SALIENT ANATOMICAL FEATURES FOR ROBUST SURFACE REGISTRATION AND ATLAS-BASED MODEL UPDATING IN IMAGE-GUIDED LIVER SURGERY

By

Logan W. Clements

Dissertation

Submitted to the Faculty of the

Graduate School of Vanderbilt University

in partial fulfillment of the requirements

for the degree of

DOCTOR OF PHILOSOPHY

in

Biomedical Engineering

May, 2009

Nashville, Tennessee

Approved by:

William C. Chapman

Benoit M. Dawant

Robert L. Galloway

Michael I. Miga

James D. Stefansic

DEDICATION

This work is dedicated to my nephews,

Zachary and Blaine.

ACKNOWLEDGEMENTS

First and foremost, I would like to thank my primary advisors Dr. Robert Galloway and Dr. Michael Miga for their overwhelming patience and support during the completion of this work. The inspiration and technical guidance has been invaluable throughout my graduate career. Further, Dr. Galloway has been a professor and mentor of mine since my undergraduate days and it was through him that I have found the support I needed to pursue a doctorate degree. For this, I am eternally grateful.

I must also acknowledge the remaining members of doctoral committee, Dr. William Chapman, Dr. Benoit Dawant, and Dr. James Stefansic, for their willingness to facilitate this dissertation. Dr. Chapman was instrumental in the acquisition of the clinical data as well as providing practical insight into the feasibility of the proposed methods. Dr. Dawant has provided invaluable knowledge concerning image registration and facilitated the deformation analysis portion via the cutting edge algorithms developed in his lab. Dr. Jim Stefansic has provided exceeding knowledge with regards to the marketability and requirements therein of image-guided surgical methods.

The knowledge imparted by my colleagues within the SNARL/BML complex cannot be overstated. Without the aid of Dr. David Cash and Dr. Tuhin Sinha, none of this work would have been possible. The contribution they provided with regards to hands-on knowledge and programming fundamentals have been invaluable. The amount of foresight these two gentlemen shared have yet to be equaled within in SNARL/BML. I would also like to extend special thanks to my roommate and colleague Prashanth Dumpuri. He has been a great friend and sounding board throughout my graduate tenure. Without his modeling assistance, much of this work would not have been possible. I must also thank Dr. David Kwartowitz for his assistance in performing the phantom studies used in this work. Finally, I would like to thank

my office mates Anne Benencasa and Rowena Ong for their support and for putting up with my neurotic tendencies.

I can not go without giving a huge thanks to all of my friends and fellow graduate students that have stuck by me through the trials and tribulations of graduate study. While too many to mention individually, the moral support and camaraderie has been as invaluable as any technical knowledge that has been imparted to me throughout my studies. I can only hope that I have played a similar role to a mere fraction of those that have helped me.

Finally, I must thank my family. They have been wholly supportive and have been a beacon of inspiration for me throughout my academic career. Without their inspiration and guidance I certainly would not have had the opportunity to experience such a level of academic achievement. There is no possible way for me to ever truly compensate them for all they have provided me.

TABLE OF CONTENTS

LIST OF TABLES

LIST OF FIGURES

CHAPTER I

INTRODUCTION

Objective

A successful surface based image-to-physical space registration in image-guided liver surgery (IGLS) is critical to provide reliable guidance information and pertinent surface displacement data for use in deformation correction algorithms. The current protocol used to perform the image-to-physical space registration involves an initial pose estimation provided by a point based registration of anatomical landmarks identifiable in both the pre-operative tomograms and the intra-operative presentation. The surface based registration is then performed via a traditional iterative closest point algorithm between the pre-operative liver surface, segmented from the tomographic image set, and an intra-operatively acquired point cloud of the liver surface provided by a laser range scanner (LRS). Using the aforementioned method, the registration accuracy in IGLS can be compromised by poor initial pose estimation as well as intra-operative soft tissue deformation. Based on the lack of robustness and propensity for traditional surface registration methods to converge to unreasonable solutions given poor initial pose, a more robust registration method is needed.

Similar to the well documented brain shift experienced during neurosurgical procedures, intra-operative soft tissue deformation in open hepatic resections is the primary source of error in current IGLS applications. Numerous avenues have been suggested to aid in the compensation for the experienced soft tissue deformation, including the use of intra-operative tomography and ultrasound. However, intraoperative computed tomography and magnetic resonance imaging equipment is extremely expensive and

cumbersome in the operating room environment. Additionally, intraoperative ultrasound provides low signal-to-noise images with a limited field of view of the patient's anatomy. Ultimately, the goal for image-guidance is to update the high contrast, high resolution pre-operative tomograms to match the intra-operative presentation.

Mathematical models, which have been used to model various mediators of the deformation in neurological surgery, have been proposed to provide the missing link between the pre-operative and intra-operative presentations. While the direct solution of mathematical models, utilizing intra-operatively determined displacements, during surgery is promising in facilitating deformation compensation, more recent work in atlas-based methods seem to provide a more realistic alternative. By simulating the range of deformation sources in a pre-operatively computed atlas and matching the intra-operative data to the atlas, compensation for soft tissue deformation can be performed with minimal user interaction and in a fraction of the time needed to directly solve the model.

Specific Aims

Specific Aim 1. *Implement a method to robustly register intra-operatively acquired liver LRS data with surfaces reconstructed from pre-operative tomograms.* The robustness characteristics of the developed method will be determine via rigorous testing with the ultimate goal of providing proper alignments even in conditions where no initial pose estimation is given. Additionally, the proposed method will be evaluated, relative to the traditional method, in terms of the feasibility of incorporation into an image-guided liver surgery system based on solution time and required user interaction.

Specific Aim 2. *Measure the extent of soft tissue deformation experienced in open*

liver resection procedures. A method for the quantification and analysis of intra-operative surface deformation and shape change in open hepatic procedures will be developed. Further, analysis of the deformation will be performed in order to determine the similarities of deformation experienced between similar surgical procedures in hopes of providing further insight into potential novel methods of deformation compensation.

Specific Aim 3. *Develop an atlas-based model updating scheme for the correction of soft tissue deformation, relative to the pre-operative presentation, imposed upon the liver by the mobilization and packing procedure performed prior to resection.* Emphasis will be placed on the determination of the feasibility of utilizing an atlas-based approach within the context of model updating in IGLS. A combination of simulation and phantom data will be used to demonstrate the feasibility of the developed algorithm in comparison with other proposed methods. Further, the impact of incorporating salient anatomical feature weighting within the developed method will be evaluated.

CHAPTER II

BACKGROUND AND SIGNIFICANCE

The information provided by diagnostic, pre-operative computed tomography (CT) or magnetic resonance (MR) images allow surgeons to determine the operative plan for patients presenting with primary or metastatic liver diseases. Additionally, a significant body of research has been geared toward the processing and analysis of the pre-operative tomograms such that extensive surgical planning and simulation can be performed [89, 132]. Based on the value of the information provided by pre-operatively obtained data, it is desirable to place this information in the context of the patient's anatomy during the surgical procedure. The field of image-guided surgery (IGS) serves to provide the link between pre-operative data and the intra-operative anatomical presentation by utilizing thee-dimensional (3D) localization devices, algorithms developed in the field of image registration, and current visualization and display techniques [65, 120, 119]. While the techniques of IGS are constantly improving, the field is in a relative infancy and many fundamental problems exist in the current implementation of many IGS systems. More specifically, a vast majority of proposed IGS systems rely, to some extent, on the assumption of rigidity between the pre-operative image data and the intra-operative patient anatomy. This assumption is known to be invalid and is one of the primary sources of error in current systems. The soft tissue deformation problem, as well as other procedure specific difficulties, provide the motivation for ongoing research in the field of image-guided liver surgery (IGLS).

Overview of Hepatic Cancer and Surgical Procedures

In order to understand the specific limitations and difficulties with the implementation of IGS for liver applications and to provide a general rationalization for ongoing research in the field, a knowledge of general liver anatomy, prevalence of liver disease, and common surgical practices is needed.

Physiological and Anatomical Characteristics of the Liver

The liver is the largest abdominal organ in the human body and is charged with the physiological duties of degradation of body wastes and hormones, synthesis of plasma proteins, storage of glycogen and fats, activation of Vitamin D, removal of bacteria and worn-out red blood cells, excretion of cholesterol and bilirubin, and secretion of bile salts [136]. The liver is located inferior to the diaphragm, to which it is attached by the left and right triangular ligaments (illustrated in Figure II.1 on segment II), on the right side of the abdominal cavity. The falciform ligament (illustrated in Figure II.1 between segment IV and segments II and III) divides the left and right lobes and serves to attach the liver to the abdominal wall.

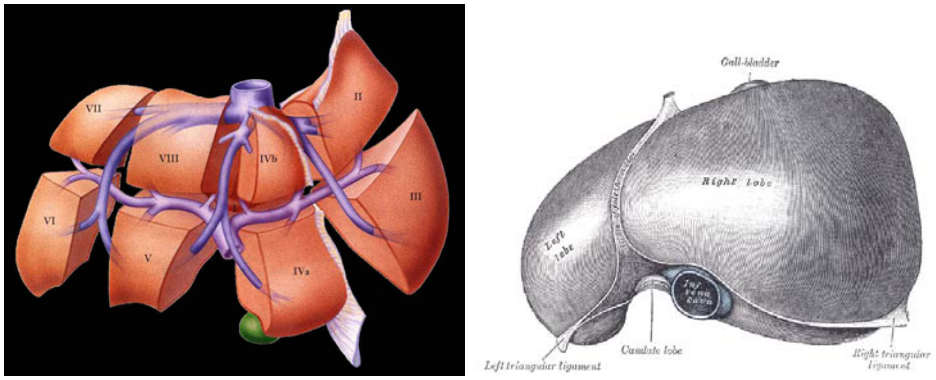

Figure II.1: Artistic depiction of the segmental nature of the liver anatomy (left) and superior view of liver showing the primary ligament structures. The portal and hepatic venous structure as well as the gallbladder are highlighted.

The liver can be divided into a set of eight functionally distinct regions with respect

to vascular supply and biliary drainage. These regions are termed the Couinaud segments [45] and the numbering convention of this characterization are is demonstrated in Figure II.1 and Figure II.2. Based on the functional independence of these regions and the information concerning the anatomical relationships between the vasculature and biliary tree, resections are often performed based on the Couinaud segments [66, 67, 131].

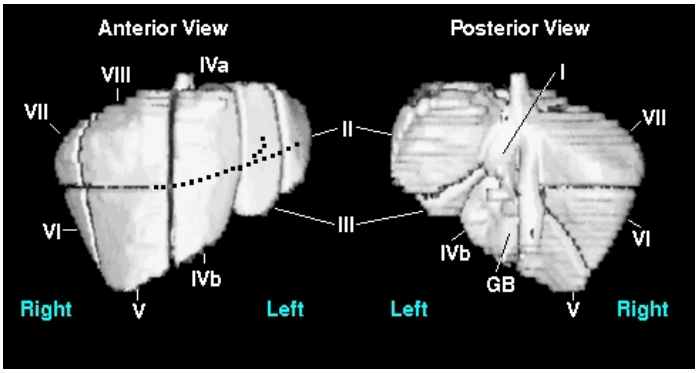

Figure II.2: 3D surface rendering of the liver surface depicting the division of the anatomy via the Couinaud segments from anterior (left) and posterior (right) views [154].

Being as one of the major physiological roles of the liver is the processing and degradation of body wastes and hormones, the organ is highly vascularized and contains significant blood volume. The portal vein and hepatic artery provide the blood flow into the liver tissue while the blood leaves the liver through the hepatic vein. The hepatic artery provides 25% of the inflowing blood and virtually all of the oxygen, while the portal vein provides the remaining 75% for detoxification [11].

Prevalence of Primary and Metastatic Liver Cancer

In 2006, an estimated 18,510 patients will be diagnosed with cancer of the liver and intra-hepatic bile duct [2]. Additionally, primary liver cancers occur in African and Asian populations at rate approximately ten times that seen in the United States

and Northern Europe [128]. The most common form of primary malignancy found in the liver is hepatocellular carcinoma (HCC). Most cases of HCC are secondary to either hepatitis infections or cirrhosis. The mitigation of the primary risk factors for HCC provides a rationalization for the low incidence of these malignancies in developed countries.

Metastatic liver disease is approximately 20 times more prevalent in developed countries than primary malignancies. Since the portal vein receives a large volume of blood directly from the gastrointestinal system, a majority of metastatic liver tumors originate from primary colorectal malignancies. Other sources of metastases include the lung, pancreas, breast, gallbladder, prostate, and melanoma [100]. Based on the American Cancer Society statistics, an estimated 148,610 new cases of colorectal cancer will be diagnosed in 2006 [2]. It is suspected that roughly half of these patients will develop a liver metastases during the course of their illness, with 20% to 30% of patients having liver metastases at the time of diagnosis [129].

Treatment of Liver Cancer

The only treatment method that provides a potential for cure of both primary malignancies and certain metastases is resection, or surgical removal of the diseased region [131]. Studies have shown that five year survival rates after metastases resection are in the 25% to 40% range and from 0% to 2.5% for un-resected patients [129]. Unfortunately, however, 70% to 90% of all patients that present with primary liver tumors are ineligible for resection procedures based on tumor location, severe cirrhosis, extent of liver disease or extrahepatic disease [128].

In situations where resection is not feasible, other procedures, such as transplantation and various ablation methods can be performed. The reader is pointed to the article by Frezza which provides an extensive review of alternative treatments for patients with un-resectable hepatic cancers [60]. Transplantation for primary tumor

cases has shown survival rates similar to conventional resection [123, 159]. A less invasive alternative to the treatment of liver tumors comes in the form of ablation methods. Currently, there are two forms of ablation therapy. Cryoablation utilizes a probe cooled to sub-zero temperatures to freeze and ultimately destroy tumor cells [31, 69]. However, the effect of cryoablation on normal tissue as well as the incidence of post-operative complications has been a concern [32, 33, 142]. In contrast to cryoablation, radiofrequency ablation (RFA), which uses electromagnetic energy to heat tissue and induce cell death, produces fewer complications [77, 160, 51]. Ultimately, the success of ablation procedures depends on the ability to accurately localize tumors during procedures, such that no residual tumor is left untreated. A number of interventional imaging techniques have been proposed to facilitate the guidance of ablation procedures.

Intraoperative Imaging for Surgical Guidance

The use of intra-operative imaging for the guidance of various hepatic procedures has been the subject of extensive research. The most ubiquitous imaging modality used in liver resection procedures is intra-operative ultrasound (iUS). The use of iUS has been shown to impact the choice of resection treatment, relative to that determined by analysis of pre-operative computed tomography (CT) images, for patients with a variety of primary diseases [114, 122, 116]. In addition to its use in determining resection plans during procedures, iUS has also been used to guide open, percutaneous, and laparoscopic radio-frequency (RF) thermal ablation of liver tumors [87, 143]. While it is apparent that iUS provides invaluable information intra-operatively and is relatively inexpensive, this modality is limited by poor signal-to-noise as well as the limited field of view of the acquired images.

In addition to iUS, intra-operative magnetic resonance (iMR) imaging has also been proposed for the guidance of RF ablation treatment of hepatic tumors [158, 24,

48]. While intra-operative tomographic imaging provides the distinct advantage of yielding full three-dimensional (3D) images of the surgical regions of interest, the utility of such modalities and corresponding widespread implementation is limited by a variety of factors, such as the exorbitant cost of the equipment and the cumbersome nature of incorporating the imaging equipment into the operating room (OR) setting. The limitations of the aforementioned intra-operative imaging modalities have provided the impetus for the development of the field of image-guided surgery (IGS) whereby the high resolution, high contrast, low noise diagnostic tomographic image volumes, acquired pre-operatively, are placed within the context of the intra-operative patient anatomy.

Introduction to Image-Guided Liver Surgery

Driven by the success of IGS research for neurosurgical applications and the desire to provide surgeons with the improved navigational information by placing the pre-operative image data in the context the intra-operative presentation, IGLS was proposed for both open and laparoscopic hepatic resections at Vanderbilt University by Herline *et al.* in 1999 [73, 71, 72, 70, 144]. More recently, Cash *et al.* have incorporated laser range scanner (LRS) technology into IGLS for the acquisition of intra-operative surface data [29, 30, 25]. Other groups have studied the incorporation of co-registered, 3D freehand ultrasound imaging data of the abdomen for intra-operative guidance of needle placement for tumor ablation [18, 118]. Bao *et al.* have recently proposed the use of co-registered laparoscopic ultrasound for use in minimally invasive liver tumor resection and ablation [9]. Additionally, the incorporation of a novel electromagnetic tracking system for use in the image-guidance of liver tumor biopsy has also been investigated [8]. For further information on the use of image-guidance for other applications, the reader is referred to the extensive reviews of image-guided procedures by Peters [120, 119] and Galloway [62]. The following

discussion will outline the major components required to perform IGLS, with specific emphasis on the protocol as described by Cash [26], since that work provides the basis for the proposed research described herein.

Pre-operative Image Data and Processing

The wealth of information that is possessed by the high resolution, 3D image sets acquired by current imaging technology provides the desire to incorporate this data into the decision making process performed during surgical procedures. While the most commonly used modalities in the acquisition of diagnostic anatomical image data for liver applications are CT and magnetic resonance (MR) imaging, the use of functional imaging methods such as positron emission tomography (PET), single photon emission tomography (SPECT) and function magnetic resonance imaging (fMRI) can be used to to provide functional information for use in IGS [102, 17, 151, 157].

The visualization of pertinent surgical structures described by the pre-operatively obtained image sets and, as will be discussed later, the ability to perform a mapping between the intra-operative patient space and the pre-operative image space are greatly facilitated by the performance of image processing on the image data. Being that manual methods of segmentation are extremely time consuming, a significant amount of research has been devoted to the development of automated and semi-automated segmentation routines used to extract pertinent anatomical regions from pre-operatively obtained images of the liver. Many of these developed segmentation and processing routines are used to provide information and renderings used for pre-operative treatment planning [132]. Dawant *et al.* have developed a robust liver segmentation algorithm [47, 74, 115] based on the level set technique proposed by Sethian [133]. The level set formulation incorporates the boundary of an object as

the zero level set in a higher order function (ϕ). The function is computed iteratively using the following relation:

$$\frac{\phi_{i,j,k}^{n+1} - \phi_{i,j,k}^{n}}{\Delta t} + F|\nabla_{i,j,k}\phi_{i,j,k}^{n}| = 0 \tag{II.1}$$

where F is the speed function that specifies the speed at which the contour evolves in a normal direction. The novelty of the level set implementation proposed by Dawant *et al.* is based upon the concept of an accumulative speed function (F) whereby not only the value of the function at a particular location but also the history of propagating contour determine the speed at which the contour evolves. Example slices of manual and semi-automatic segmentations are shown in Figure II.3.

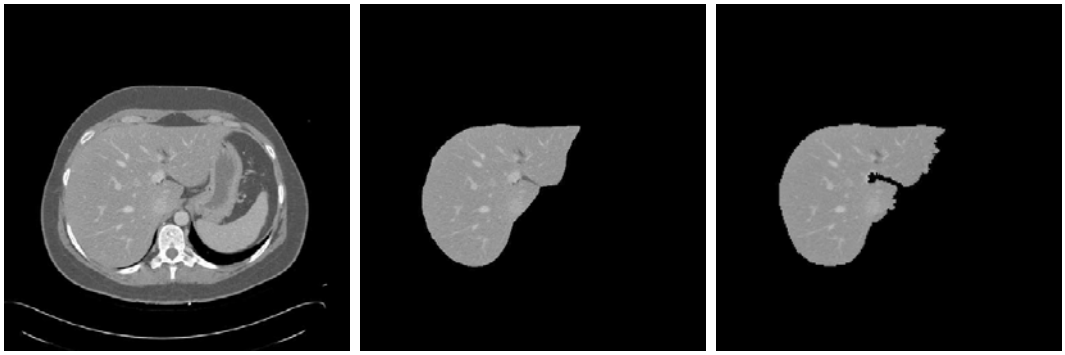

Figure II.3: Examples of slices of a CT image volume of the liver segmented with manual and semi-automatic level set techniques. These images were taken from [26].

Once segmentation of pertinent structures has been obtained, tessellated surfaces of these objects can be generated via the Marching Cubes Algorithm [84]. Being that the surface representation provided by Marching Cubes is extremely dense and lacks the true smoothness of the liver surface due to segmentation error and image sampling artifacts, the surface can be further refined using smoothing and decimation techniques [130] or surface fitting packages [23]. The decimation of the segmented liver surfaces is particularly important in situations where the surface is used in image

registration routines and extremely dense surface representations can cause the point search time to become infeasible for OR use. Figure II.4 shows sample renderings of a liver surface tessellated using the Marching Cubes algorithm as well as the smoothed surface using the FastRBF toolkit (FarField Technology, Christchurch, NZ) and a sample rendering including segmented vasculature and tumors.

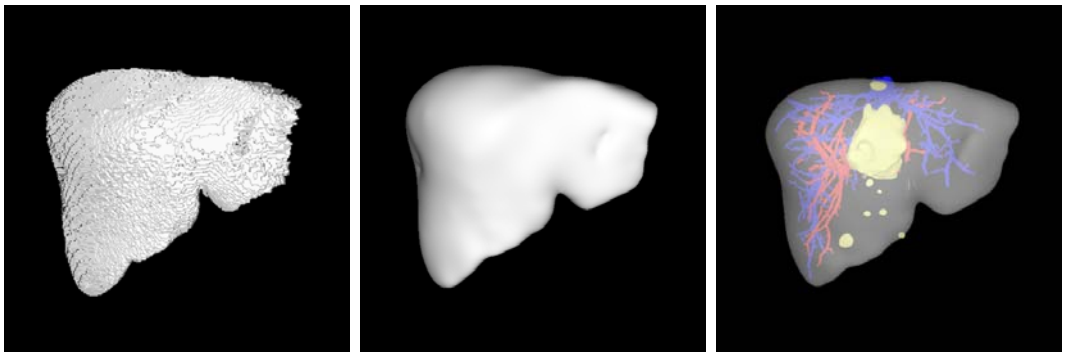

Figure II.4: Examples of the Marching Cubes (left) and FastRBF radial basis function (center) tessellations of a liver surface segmented from pre-operative images. A sample rendering of portal venous (red), hepatic venous (blue), and tumor (yellow) structures is also shown (right).

The research in the fields of vascular image segmentation and pre-operative planning and simulation have provided surgeons with valuable tools with which to determine the appropriate treatment options before the surgical procedure. However, the ability to provide a link between the wealth of information provided by the pre-operative images and the surgical presentation would be of great utility for surgeons and ultimately improve patient care. The link between the surgical field-of-view (or "physical space") and the pre-operative images (or "image space") is provided by the field of image registration.

Surface-Based Image Registration

While point-based landmarks can be reliably identified in neurosurgical IGS applications where fiducial markers can be fixed to the skull prior to the acquisition of the

pre-operative images [63, 91], the ability to utilize rigid anatomical landmarks or implanted fiducial markers is complicated in IGLS due to the mobilization and packing of the organ prior to resection. Due to the lack of reliably useful point fiducials for use in point-based registration (PBR) techniques, Herline *et al.* [72, 71] suggested the use of surface-based registration algorithms to facilitate the mapping of physical-space to image-space. An extensive review of surface based image registration is provide by Audette *et al.* [4].

One of the most popular surface registration techniques, as well as the basis of a vast number of surface registration algorithms, is the Iterative Closest Point (ICP) algorithm proposed by Besl and McKay [12]. Given a source point set (S) and target point set (T), the ICP algorithm seeks to minimize the following objective function:

$$f(\Omega) = \sqrt{\sum_{i=1}^{N_S} \|\Omega(S) - C(\Omega(s_i), T)\|^2} \tag{II.2}$$

where C denotes the closest point operator used to determine correspondence between the two point sets. Once correspondence is established, the transformation (Ω) between the point sets is determined via a closed-form PBR [76, 3]. Once Ω has been determined, the computation of point correspondence is then repeated and so the algorithm continues until some convergence criteria is met. Besl and McKay also proved that the process is guaranteed to converge, thus eliminating the need for the use of an optimization scheme. It should be noted that the ICP algorithm is extremely sensitive to initial pose and is prone to convergence to a local minimum.

Maurer *et al.* proposed an extension to the ICP algorithm called the Weighted Geometrical Features (WGF) algorithm [90]. This method described a way to incorporated multiple surfaces and point sets within an iterative matching process whereby each of the surfaces or point sets (called features) were assigned a particular weight

within the closest point cost function. Maurer *et al.* also describes the use of a multidimensional binary search tree (or kd-tree) data structure to perform the point searches in a more computationally efficient manner [10, 61]. Given N_S source points and N_T target points, the k-d tree can be constructed in $O(N_T \log(N_T))$ time. Each closest point search can be performed in $O(\log(N_T))$ time. Thus, in order to find N_S closest points, the kd-tree searching process takes $O(N_S \log(N_T))$ time, in comparison to the computational complexity of $O(N_T N_S)$ for an exhaustive search. A similar approach where point sets and surface regions are combined within an ICP based approach was also proposed by Collignon *et al.* [40].

In order to curb some of the local minima convergence issues with the traditional closest point operator used in the ICP algorithm, an interpolated closest point transform was proposed by Cao *et al.* [22]. Building on the work of Ge *et al.* [68] and Kapoutsis *et al.* [80], the interpolated closest point method first computes a closest point transform, which is a variant on the distance transform whereby each voxel in a target image volume analog contains the location of it's closest point. The proposed method computes the closest point transform using a variation on the Fast Marching Method proposed by Sethian [134]. In order to circumvent discretization error of standard closest point transform methods, a novel interpolation scheme is implemented on the closest point transform.

In addition to the use of geometrical information in surface based registration methods, a number of studies have also incorporated texture information to drive the matching process. Miga *et al.* [99] proposed the SurfaceMI algorithm which incorporated the mutual information metric [155, 88, 147] into the registration of textured cortical LRS data to textured brain surfaces extracted from MR volumes. Johnson and Kang propose the incorporation of color information to improve point correspondence determination in the registration of textured 3D data [79]. In addition to the incorporation of texture information to bias point correspondence, other groups have

proposed the use of geometric invariant features to guide correspondence determination [135, 55, 162].

While the initial focus of ICP and the aforementioned studies were primarily concerned with the use of surface registration methods to determine rigid transformations, ICP based approaches can also be used in non-rigid registration algorithms. Feldmar *et al.* [56] proposed a multi-level, multi-resolution approach and utilized the thin-plate spline transformation [20] within the ICP paradigm. The thin-plate spline provides a very convenient non-rigid transformation for use in an ICP based approach being as the splines provide a smooth warping between corresponding point sets. More recently, Chui *et al.* [34, 35, 36] introduced the Robust Point Matching (RPM) algorithm which utilizes the notion of fuzzy correspondence, rather than the implied binary correspondence used in ICP algorithms. While the results presented in these works provide an substantial contribution to the problem of non-rigid point matching, it is unclear how the RPM algorithm performs in situations where the data contained within the source point set (S) comprises only a subset of that contained within the target data (T).

Physical-Space Tracking and Intra-operative Data Acquisition

In order to perform the mapping of the intra-operative patient space to the pre-operative images and to provide a useful visualization of this mapping in IGS, the ability to establish a coordinate system within the OR and accurately track objects within this coordinate system is needed. While articulated arm systems were used in the earliest image guided procedures [63], the current *de facto* method of intra-operative localization is provided by optical tracking systems. Optical tracking systems use the principle of triangulation to localize objects within the field of view of the sensor. These systems are either passive or active, meaning that the tracked objects either act to reflect the infrared light (e.g. photo-reflective spheres) or actively

emit the light (e.g. infrared emitting diodes (IREDs)) that is detected by the sensor. Based on the known configuration of the photo-reflective spheres or IREDs on the object being tracked, optical tracking systems are also able to determine the pose of the tracked objects of interest. The primary manufacturer of the optical tracking systems used in surgical navigation is Northern Digital, Inc. (Waterloo, Ontario), whose Optotrak and Polaris units have been validated to provide sub-millimetric localization errors [64, 112, 110].

While optical localization provides the most accurate method with which to track objects and digitize points within the OR, these methods are not without disadvantages. The primary disadvantage of optical tracking is the line of sight required between source and detector. If this line of sight is broken, it becomes impossible for the camera to sense the tracked object's location. Additionally, the configuration of the source points (i.e. photo-reflective spheres or IREDs) attached the tracked object are assumed to remain in a rigid configuration relative to each other. Any deviation in the locations of these source points, relative to their "known" positions by the tracking system, can result in erroneous tracking results. In order to overcome some of the constraints imposed by optical tracking, a significant body of work has been performed to validate the used of magnetic localization systems.

Magnetic localization systems use a reference field generator that produces a spatially varying magnetic field and a sensor coil placed within the tracked probe. The orientation and position of the tracked probe can be determined by the current induced within the sensor coil by generated magnetic field. The primary advantages of magnetic localization are provided by the facts that line of sight between the reference generator and the sensor coils is not needed and the engineering of the sensor coils to be small enough that they can fit inside the tip of non-rigid objects (e.g. catheters) for tracking. A number of studies have been performed to validate the usefulness of magnetic tracking in IGS [15, 16, 121, 8]. However, due to distortions

in the generated magnetic field by ferrous objects and electronic devices, the accuracy of electromagnetic systems has not reached the standard set by optical systems [14, 111, 113].

In the initial work proposed by Herline *et al.* [72, 73, 71], an optically tracked probe was used to obtain liver surface data by continuously collecting the probe tip location as the surgeon moved the probe across the liver surface (shown in Figure II.5). More recently, the work of Cash *et al.* has incorporated the use of a tracked LRS system (shown in Figure II.5) capable of capturing spatially dense point clouds representing the liver surface in a non-contact fashion [29, 30, 25]. The use of LRS data has also been proposed by Audette *et al.* [5, 6] and Sinha *et al.* [138, 139] for use in neurosurgical IGS. More specifically, these groups discuss the use of LRS data in the determination of intra-operative brain shift. Similarly, Skrijar *et al.* [140, 141] and Sun *et al.* [149, 150] have utilized stereo-camera pairs to obtain cortical surface point cloud representations for the measurement of intra-operative brain shift and, ultimately, for use in deformation compensation routines.

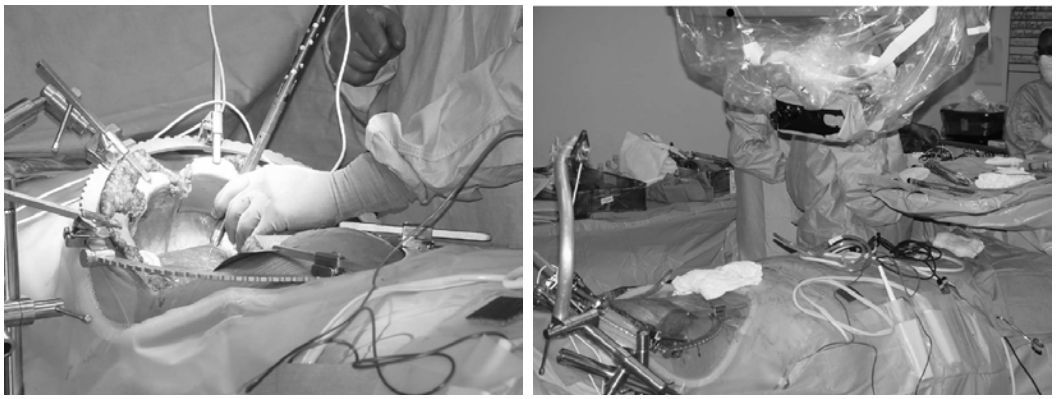

Figure II.5: Digitization methods employed during surgery to identify anatomical points and surfaces. An optically tracked pen probe (left) can be used to digitize anatomical fiducial points and surface regions while tracked LRS hardware (right) is used to acquire high resolution surface scans of the liver.

In addition to the acquisition of intra-operative surface data using stereo-camera

pairs and LRS technology, a significant body of work has been performed on the incorporation of co-registered iUS for use in IGS. Trobaugh *et al.* [153] and Comeau *et al.* [41, 42] performed the initial work in the calibration and display of tracked iUS for neurosurgical IGS. More recently, Lunn *et al.* has used co-registered iUS to perform displacement estimation for use in deformation compensation methods [85]. The use of co-registered iUS has also been proposed for use in guidance of needle placement for tumor ablation in hepatic surgery [18, 118]. Aylward *et al.* has proposed the integration of iUS data via a vessel based registration with pre-operative CT and MR angiograms for guidance of hepatic tumor radio-frequency ablation [7]. More recently, Bao *et al.* has reported the incorporation of tracked laparoscopic US for use in minimally invasive hepatic procedures used to treat decompensated cirrhotics [9].

The acquisition of intra-operative data using tracking systems and imaging modalities, such as LRS, stereo-pair cameras, and iUS, provides a key component to the determination of the image-to-physical-space registration. However, current IGS systems use rigid body assumptions to determine this registration and a number of studies have shown that these assumptions are invalid and a primary source of error. Therefore, the compensation for the soft tissue deformation that occurs during surgical procedures is of great importance and, as we shall see, is greatly facilitated by the data acquired in the OR using the aforementioned technology.

Compensation for Soft Tissue Deformation

Intra-operative soft tissue deformation studies have shown that the incidence of brain shift during neurosurgical procedures is a significant contributor to error in IGS with maximum gravity induced displacements found to be on the order of 1 cm [81, 105, 124, 75, 93, 103, 107]. While no studies of intra-operative tissue deformation in open liver procedures has been performed, it is quite apparent that soft tissue deformations play a significant role in current IGLS system inaccuracies. In

order to rectify the error that exists between the pre-operative image volumes and intra-operative presentation due to soft-tissue deformation, two different avenues for compensation have been proposed: intra-operative tomographic imaging and non-rigid image registration. While we will consider each of these methodologies as being separate entities for the sake of discussion, many studies have combined aspects of each within their proposed systems.

The use of iMR technology to rectify the brain shift problem was initially proposed by Nimsky *et al.* [107, 108, 109] Additionally, Ferrant *et al.* proposed the use of finite element methods (FEM) to solve a mathematical model for computing the deformation and providing an interpolation between intra-operative and pre-operative image volumes [57, 58]. While the use of iMR to provide a viable solution to the soft tissue deformation problem is appealing, several limitations ultimately make the reliance on intra-operative tomographic imaging to be impractical for widespread implementation. Namely, iMR hardware is exorbitantly expensive and is also susceptible to imaging artifacts due to magnetic field inhomogeneities caused by ferrous materials in the operating room. Ultimately, the use of a more practical intra-operative imaging technology (e.g. iUS or LRS) would be more amenable to widespread use.

The most popular framework for non-rigid image registration in soft tissue deformation compensation involves the use of the FEM to solve bio-mechanical models. In addition to the work of Ferrant *et al.* [57, 58], several other groups have proposed the use of and developed bio-mechanical models for the compensation of soft tissue deformation. Miga *et al.* [117] developed a model of the brain based on the theory of consolidation [13], which was demonstrated to compensate for pharmacological agents (e.g. mannitol) and resection and retraction [95, 98]. Their developed model was validated in animal studies to recover 75% to 85% of the error due to brain shift [96]. More recent work has involved the incorporation of intra-operatively acquired sparse data to drive the developed bio-mechanical brain models. Skrinjar *et al.* [140, 141]

and Sun *et al.* [149, 150] have demonstrated the utility of stereo-camera pairs in calculating cortical surface deformations. Sinha *et al.* have demonstrated the use of LRS to acquire serial scans of the cortical surface and, via deformable registration methods, track the shift of the brain surface [139]. Lunn *et al.* have proposed the use of the adjoint equations to assimilate sparse intra-operative data with bio-mechanical models [86].

The use of LRS data to drive a bio-mechanical model of the liver was initially proposed by Miga *et al.* [94]. Building on this work, Cash *et al.* proposed an incremental approach to solving the model [28]. Additionally, this work demonstrated the use of a deformation identifying rigid registration which provided a more meaningful alignment than a traditional ICP registration. Other groups, such as Brock *et al.* [21], have used time dependent models to describe the liver motion due to respiration.

Recently, the use of atlas-based methods have been proposed for incorporation into IGS systems for the compensation of deformation. Dumpuri *et al.* have proposed the computation of a deformation atlas, provided by FEM solutions of a bio-mechanical model under a variety of conditions determined by *a priori* knowledge of the surgical procedure [53, 52]. The individual surface displacements predicted by the deformation atlas are then matched with those determined via cortical surface tracking with LRS using a constrained linear inverse model. Similar methods have been proposed by Davatzikos *et al.* [46] wherein a statistical approach based on principal component analysis (PCA), inspired by the work of Cootes *et al.* [43, 44], is used to fit deformed data to the atlas.

Several groups have proposed the incorporation of non-rigid registration using spline-based transformations for the compensation of a variety of intra-operative deformation sources. Lange *et al.* have proposed the use of a combined algorithm using ICP and multi-level B-Splines to match iUS images of liver vasculature with the segmented vessels from pre-operative CT/MR angiograms [82]. Rohlfing *et al.*

presented a method to model liver motion due to respiration using an MI based multi-dimensional non-rigid registration between gated respiratory MR images [126]. While spline-based methods of deformation modeling have shown potential, the use of bio-mechanical model based methods seem more appealing due to the fact that the solutions will be based on constitutive physical laws. Further, the spline-based methods that utilize iUS data can only perform the model-updating in the region where iUS data has been acquired as opposed to bio-mechanical models which can perform deformation compensation over the entire liver volume.

Summary

The recent developments towards realizing IGLS are very exciting. However, a number of shortfalls are apparent. First, the *de facto* utilization of ICP methods for the performance of image-to-physical space registration is very much dependant on accurate initialization and can easily converge to an inaccurate local minimum. The development of methods that provide for more robust methods of intra-operative registration is paramount to the continued success and utility of image-guided methods within the context of open hepatic procedures. Further, the development of a more robust method of registration will facilitate the analysis of intra-operative soft tissue deformation and provide insight into practical methods of model-updating for IGLS.

CHAPTER III

MANUSCRIPT 1 - ROBUST SURFACE REGISTRATION USING SALIENT ANATOMICAL FEATURES FOR IMAGE-GUIDED LIVER SURGERY: ALGORITHM AND VALIDATION

Original form of the manuscript appears in ***Medical Physics****, Vol. 35, No. 6, pp. 2528-2540, 2008.*

Abstract

A successful surface-based image-to-physical space registration in image-guided liver surgery (IGLS) is critical to provide reliable guidance information to surgeons and pertinent surface displacement data for use in deformation correction algorithms. The current protocol used to perform the image-to-physical space registration involves an initial pose estimation provided by a point based registration of anatomical landmarks identifiable in both the pre-operative tomograms and the intraoperative presentation. The surface based registration is then performed via a traditional iterative closest point (ICP) algorithm between the pre-operative liver surface, segmented from the tomographic image set, and an intra-operatively acquired point cloud of the liver surface provided by a laser range scanner (LRS). Using this more conventional method, the registration accuracy can be compromised by poor initial pose estimation as well as tissue deformation due to the laparotomy and liver mobilization performed prior to tumor resection. In order to increase the robustness of the current surface-based registration method used in IGLS, we propose the incorporation of salient anatomical features, identifiable in both the pre-operative image sets and intra-operative liver surface data, to aid in the initial pose estimation and play a more significant role in the surface based registration via a novel weighting scheme. Examples of such salient anatomical features are the falciform groove region as well

as the inferior ridge of the liver surface. In order to validate the proposed weighted patch registration method, the alignment results provided by the proposed algorithm using both single and multiple patch regions were compared with the traditional ICP method using six clinical data sets. Robustness studies were also performed using both phantom and clinical data to compare the resulting registrations provided by the proposed algorithm and the traditional method under conditions of varying initial pose. The results provided by the robustness trials and clinical registration comparisons suggest that the proposed weighted patch registration algorithm provides a more robust method with which to perform the image-to-physical space registration in IGLS. Further, the implementation of the proposed algorithm during surgical procedures does not impose significant increases in computation or data acquisition times.

Introduction

The determination of an accurate image-to-physical space registration is a fundamental step in providing meaningful guidance information to surgeons via image-guided surgery (IGS). A significant body of research has been dedicated to the use of IGS techniques for neurosurgical applications and has resulted in several commercially available systems (e.g. StealthStation, Medtronic Navigation, Louisville, CO). A common feature of the developed IGS technology for neurosurgery is the use of point-based landmarks, via bone-implanted or skin-affixed fiducial markers, to provide the registration of image- and physical-space. The use of such point-based techniques is greatly facilitated in neurosurgical IGS by the rigid anatomy (i.e. skull) surrounding the organ of interest. Unfortunately, the use of such point-based techniques is not applicable for open abdominal IGS due to the lack of rigid anatomical landmarks and the inability to pre-operatively attach a set of extrinsic fiducials that will remain rigid relative to the organ of interest after laparotomy and organ mobilization.

Since the use of rigid, point-based landmarks is not feasible in image-guided liver surgery (IGLS), surface-based techniques were proposed to determine the registration between the pre-operative images and the intra-operative presentation [73, 72]. Specifically, the iterative closest point (ICP) algorithm, proposed by Besl and McKay [12], has traditionally been used to determine the transformation between the image-space surface of the liver, derived from pre-operative image segmentations, and the intra-operative liver surface. Intra-operative data were initially acquired using an optically tracked probe while more recent efforts have utilized a laser range scanner (LRS) to provide spatially dense, textured delineations [29, 30]. In addition to being used for IGLS, LRS technology has also been employed to provide surface data in neurosurgical procedures for the purpose of tracking intra-operative brain shift [5, 6, 99, 139]. Several groups have also explored the use of intra-operative ultrasound (iUS) to acquire sparse data for use in abdominal IGS [18, 118].

The current protocol for surface-based image-to-physical space registration in IGLS (described in detail by Cash *et al.* [30, 27]) begins with the selection of anatomical fiducial points in the pre-operative image sets prior to surgery. The homologous physical-space location of these anatomical fiducials are then digitized during the surgical procedure such that a point-based initial alignment registration can be performed. The point-based registration serves to provide a reasonable initial pose for the ICP algorithm, which is used to register the liver surface derived from pre-operative images and LRS data acquired intra-operatively.

Being that the surface alignment provided by the ICP algorithm is highly dependent on the initial pose of the surfaces, gross errors in the initial alignment provided by the point-based registration can result in erroneous surface alignments. A failed surface-based registration not only compromises the guidance information relayed to the surgeon but also impairs deformation correction efforts due to inaccurate surface displacement data that are used to drive mathematical models [28]. In IGLS, the

quality of the initial alignment registration can be compromised by the large fiducial localization errors (FLE) inherent in using anatomical landmarks that undergo deformation relative to the pre-operative images. Additionally, gravity and the effects of the liver mobilization and packing performed prior to open liver resections can lead to liver deformations that can compromise the results of a rigid ICP surface registration. Figure III.1 shows an example clinical data set where a poor initial alignment registration, due to high FLE of the anatomical fiducials, and large liver deformations resulted in the convergence of the rigid ICP algorithm to a gross misalignment. A similar lack of robustness of ICP in the presence of planar LRS data has been exemplified in the work of Cash *et al.* [27]

In order to circumvent erroneous surface registrations due to gross misalignments in the initial pose, we propose the incorporation of reliably identifiable, salient anatomical features into the ICP algorithm. As shown in Figure III.2, the falciform ligament region is one such feature. This ligament divides the medial and lateral segments of the left lobe and can be identified on the pre-operative image surface via the ligament's distinctive groove in the surface. The falciform ligament region can be delineated in the intra-operative LRS surface presentation via the difference in texture between the ligament and liver parenchyma. In addition to the falciform groove, the inferior ridge of the liver between the falciform and right triangular ligaments along sections IV, V, and VI would also be a potential salient feature to utilize. For the purposes of this study the salient anatomical features were delineated in the pre-operative CT image space via manual segmentation of liver surface (generated via the Marching Cubes Algorithm [84]). With regards to intra-operative LRS salient feature segmentation, the homologous regions were delineated by the surgeon via optically tracked pen probe. These point sets, as well as the texture information provided by the LRS, were then used to guide the manual segmentation of the salient features in

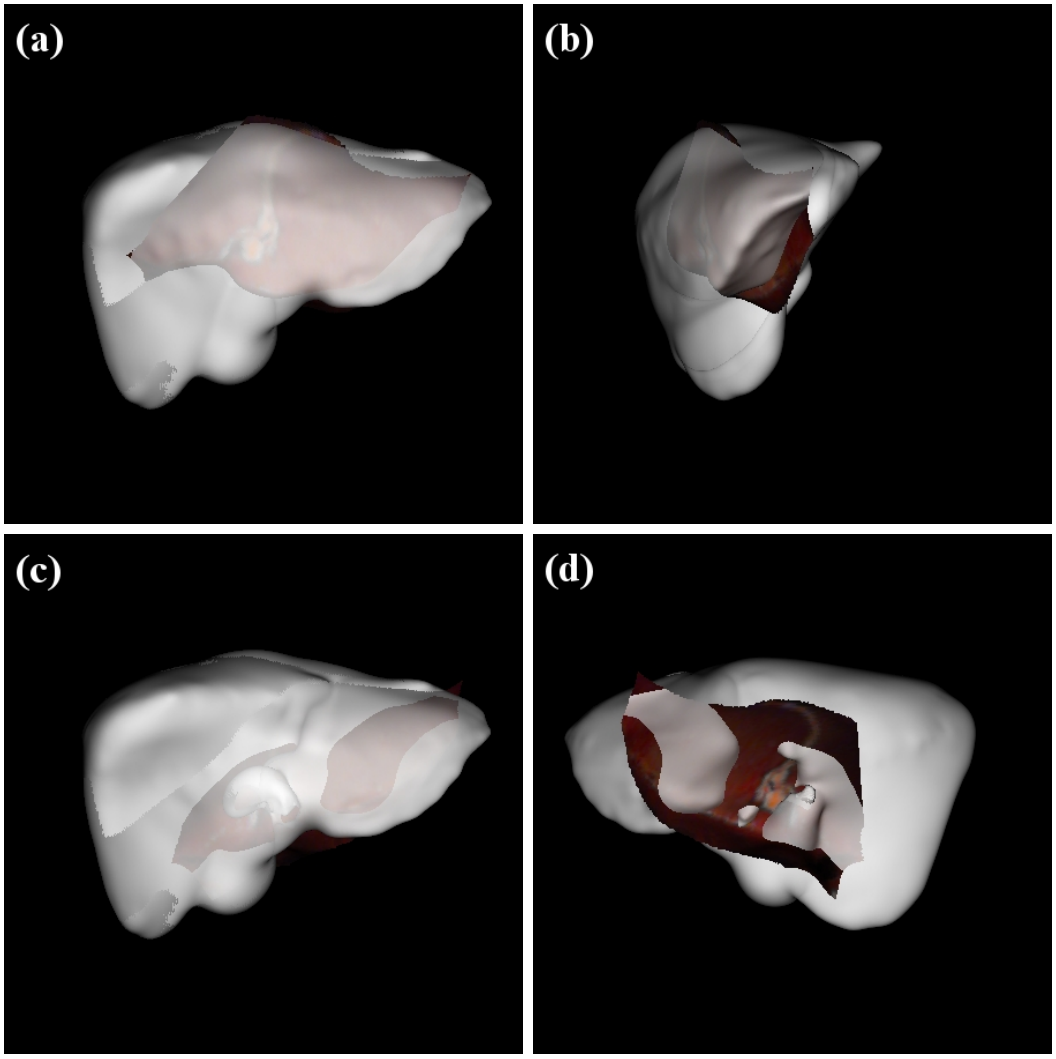

Figure III.1: Example of poor initial alignment (a),(b) and resulting misregistration (c),(d) of clinical data obtained using a traditional ICP algorithm. The combination of poor initial alignment and significant soft tissue deformation from the mobilization and packing procedure performed by the surgeon resulted in a significant misalignment of the two surfaces. Note that the LRS scan of the anterior surface of the liver is registered to the posterior liver surface via ICP.

the intra-operatively acquired sparse data. A preliminary formulation allowing the incorporation of a single salient anatomical feature has been described previously [37].

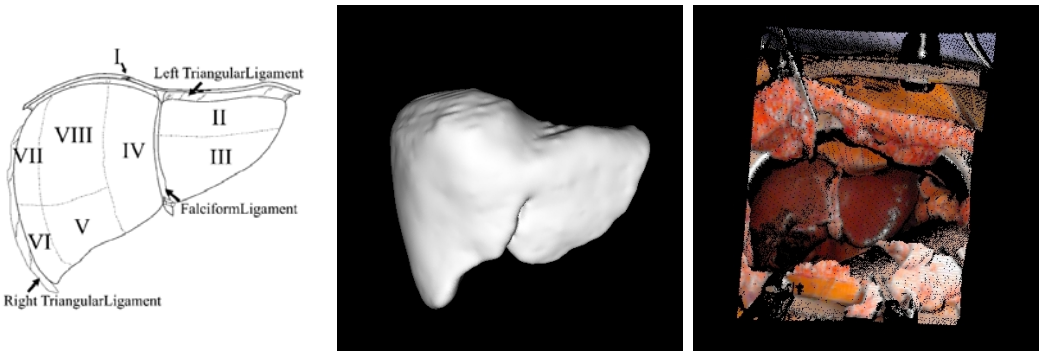

Figure III.2: Anatomical schematic (left) and examples of pre-operative image (middle) and intra-operative LRS liver data (right) with corresponding falciform ligament regions outlined. Note that the falciform ligament region can be located on the pre-operative image surface via the groove in the surface and texture can be used to delineate the falciform region in the LRS surface.

Related Work

The proposed use of salient anatomical features to weight the ICP registration is similar to the weighted geometrical features (WGF) algorithm described by Maurer *et al.* [90] This method described a way to incorporate multiple surfaces and point sets within an iterative matching process whereby each of the surfaces or point sets (called features) were assigned a particular weight within the closest point cost function. The WGF algorithm was shown to facilitate the registration of computed tomography (CT) and T2-weighted magnetic resonance image volumes of the head. The work also provides the closed form solution to perform a weighted point-based registration (PBR) that is utilized in this work. A similar approach where point sets and surface regions are combined within an ICP based approach was also proposed by Collignon *et al.* [40]

In order to curb some of the local minima convergence issues with the traditional

closest point operator used in the ICP algorithm, an interpolated closest point transform was proposed by Cao *et al.* [22] Building on the work of Ge *et al.* [68] and Kapoutsis *et al.* [80], the interpolated closest point method first computes a closest point transform, which is a variation on the distance transform whereby each voxel in a target image volume analog contains the location of it's closest point. The proposed method computes the closest point transform using a variation on the Fast Marching Method proposed by Sethian [134]. In order to circumvent discretization error of standard closest point transform methods, a novel interpolation scheme is implemented on the closest point transform.

In addition to the use of geometrical information in surface based registration methods, a number of studies have also incorporated texture information to drive the matching process. Miga *et al.* [99] proposed the SurfaceMI algorithm which incorporated the mutual information metric [155, 88, 147] into the registration of textured cortical LRS data to textured brain surfaces extracted from MR volumes. Johnson and Kang propose the incorporation of color information to improve point correspondence determination in the registration of textured 3D data [79]. In addition to the incorporation of texture information to bias point correspondence, other groups have proposed the use of geometric invariant features to guide correspondence determination [135, 55, 162].

Additionally, a deformation identifying rigid registration (DIRR) has been proposed by Cash *et al.* [28] The DIRR provides a marked improvement in surface alignments relative to ICP with respect to the facilitation of deformation compensation algorithms. However, the algorithm relies on a Powell's method optimization scheme to determine the rigid-body transformation and, thus, is more time consuming to perform and may not be feasible for intra-operative implementation at the present time. Additionally, the ability of the DIRR to provide reasonable alignments using clinical data has not yet been demonstrated.

Objective

The objective of this work is to implement a surface based registration method that utilizes the homologous, salient anatomical features to ensure convergence to reasonable solutions under conditions of poor initial alignment. Similar to our preliminary work, we propose that these extracted anatomical regions be used to bias both the point correspondence determination as well as guide the traditional ICP method via a dynamic weighting scheme such that convergence to an extremum is avoided. Further, we seek to demonstrate that the use of multiple salient features will allow the surface registration algorithm to converge to favorable solutions in the absence of initial pose information. The ability to provide robust, favorable alignments in the absence of an initial PBR presents a significant advancement to the performance of intra-operative image-to-physical space registrations in IGLS.

Methods

Weighted Patch ICP Algorithm

The algorithm proposed in this work is an extension to the WGF algorithm proposed by Maurer *et al.* [90] The homologous anatomical features, or patches, will be used to both bias point correspondence determination as well as play a more significant role in the PBR performed at each iteration of the algorithm. The weighting scheme used to bias the PBR is dynamic over the course of the algorithm where the homologous patch regions play an overwhelming role early in the registration process to ensure the patches are initially aligned and a more supportive role at later iterations in the algorithm.

For the following explanation, let $S = \{\mathbf{s}_m\}$ for $m = 1, \ldots, N_S$ be the source point set and $T = \{\mathbf{t}_n\}$ for $n = 1, \ldots, N_T$ be the target point set. Assume that the point sets S and T each contain a number of patch point sets (N_p) that describe the homologous anatomical features that are used to drive the registration. Further, let

$\{p_m^S\}$ and $\{p_n^T\}$ be integer arrays that contain values along the interval $[0, N_p]$, where an array value of 0 corresponds with the non-patch point indices and a value greater than 0 indicates the patch point indices (i.e. a value of 1 indicates that the particular point index refers to a point within the first anatomical feature). Let $\{w_m\}$ be a set of weights where $w_m = 1$ for $p_m^S = 0$ and $w_m = w_{PBR}$, a dynamic weighting factor used to bias the PBR at each iteration, for $p_m^S > 0$.

Point Correspondence Determination

In order to bias the point correspondence determination for the patch point sets, we introduce a weighting factor w_{PC}, where $0 < w_{PC} << 1$. The weighting factor is used to bias the closest point operator, C_m, by significantly decreasing the Euclidian distances (d) between patch point pairs via the following relationship:

$$d_{m,n} = \begin{cases} w_{PC}\|\mathbf{s}_m - \mathbf{t}_n\| & \text{if } p_m^S = p_n^T \\ \|\mathbf{s}_m - \mathbf{t}_n\| & \text{otherwise} \end{cases} \tag{III.1}$$

In other words, Euclidean distances identified as being between source and target patch points are multiplied by the fractional weighting factor (w_{PC}). Since the weighting factor is presumably a very small fraction, the corresponding point found for a source patch point will primarily be contained within the target patch point set. This method of point correspondence determination is different, and to a degree more general, than that that proposed by Maurer *et al.* [90] Specifically, there is no constraint placed on the points that are determined as non-patch points and these points are allowed correspondence to the identified patch regions as well. Further, the fractional weight factor (w_{PC}) does not impose a hard correspondence constraint and, hence, even patch regions are allowed to correspond with other regions under particular circumstances.

Figure III.3 shows a pictorial representation of the weighted point correspondence

method in the case where only a single patch region is used. Biasing the point correspondence determination alone, however, will not be enough to facilitate a robust surface alignment under conditions of poor initial pose and soft tissue deformation. As described in the next section, biasing the rigid PBR performed at each iteration will provide increased robustness in the proposed algorithm. For clarification, we will use the notation of C_m^* to represent the closest point operator biased by Equation III.1.

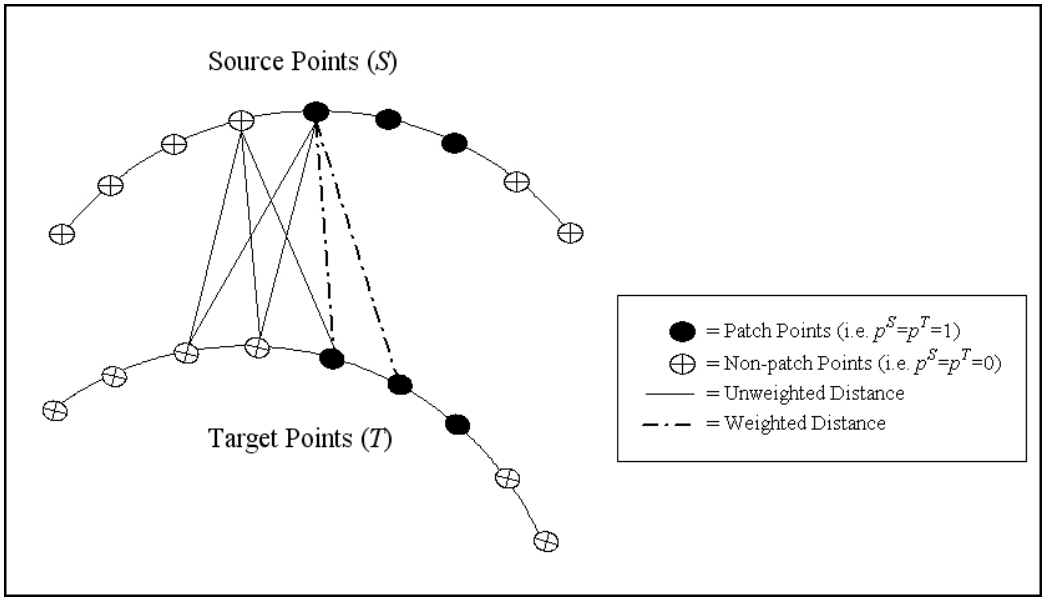

Figure III.3: Graphical depiction of the weighted point correspondence method. Only the Euclidean distances computed from source patch point to target patch point are biased by the weighting factor w_{PC} (i.e. dashed lines). The point correspondence determination for non-patch points is not effected by the weighting (i.e. solid lines) Note that the graphical depiction represents the case where only a single patch region is used.

Weighted Point-Based Registration

Once point correspondence has been determined, the weighted rigid PBR method described by Maurer *et al.* [90] is implemented. This method seeks to find the rigid-body transformation (Ω) that minimizes the following objective function (f):

$$f(\Omega) = \sqrt{\sum_{m=1}^{N_M} w_m \|C_m^*(\mathbf{s}_m, T) - \Omega(\mathbf{s}_m)\|^2} \tag{III.2}$$

where $\{w_m\}$ is a set of weights letting $w_m = 1$ for $p_m^S = 0$ and $w_m = w_{PBR}$, where $w_{PBR} \geq 1$, for $p_m^S > 0$. The weighting factor (w_{PBR}) serves to increase the role of the patch points within the determination of the transformation, Ω. A closed form solution for the special case of $w_m = 1/N_m$ for $m = 1, \ldots, N_m$ has been presented by Arun *et al.*[3] The solution is based on the singular value decomposition of the covariance matrix of the position vectors in the two spaces. The closed form solution presented by Maurer *et al.* [90], which is valid for all $w_m > 0$ is an extension of the aforementioned solution.

In the WGF algorithm, the weights used within the PBR for the geometrical features used in the registration (i.e. w_{PBR}) remain constant throughout the registration process. We seek to modify this implementation by creating a dynamic scheme by which the patch point weight, w_{PBR}, is dynamic as the algorithm progresses.

Dynamic Weighting Scheme

Being that FLE and soft tissue deformation impose error in the accurate selection of homologous anatomical points, the initial alignment provided by the anatomical fiducial based PBR can be quite poor. In order to circumvent incorrect, local minima convergence issues, the alignment of the homologous patch regions is made to play a very strong role early in the weighted patch ICP algorithm. However, due to segmentation inaccuracies and the fact that a one-to-one correspondence between source and target patch regions most likely will not exist, it is important that the bias in the PBR towards the patch regions be less significant as the registration continues. In other words, since patch regions identified in the source data will not likely contain the entire target patch point set and by biasing the registration too heavily throughout

the registration process could lead to convergence to an incorrect local minima. In order to address these problems, we allow for the remainder of the surface data to play a more significant role as the registration proceeds. By employing this dynamic weighting, the patch regions serve as an anchor at later iterations within the algorithm such that deformation will not cause a divergence in the final registration result. The following equation describes the behavior of the dynamic weighting scheme, where w_{PBR} is described as a function of iteration (i, $i \geq 1$):

$$w_{PBR}(i) = w_{PBR,max}e^{-\alpha(i-1)} + w_{PBR,base}(1 - e^{-\alpha(i-1)}) \tag{III.3}$$

In the above equation, $w_{PBR,max}$ is the maximum patch PBR weight factor and corresponds to the patch weight at the very first iteration of the algorithm. The weight factor w_{PBR} approaches $w_{PBR,base}$, the baseline patch weight where $w_{PBR,max} \geq w_{PBR,base} \geq 1$, as i becomes significantly large. The rate at which w_{PBR} approaches $w_{PBR,base}$ is determined by the relaxation constant α, where $\alpha \in [0, 1]$. A graphical representation of Equation III.3 and the effects of the relaxation constant α are graphically described in Figure III.4.

Phantom Validation

Silicon Liver Phantom and Phantom Data Acquisition

In order to quantitatively compare the developed weighted patch ICP algorithm with the traditional ICP method, the imaging phantom shown in Figure III.5 was used. Poly (dimethyl) siloxane (rubber silicone) was used to fabricate the liver model. The liver model was surrounded by seven Teflon spheres (Small Parts Inc., Miami Lakes, FL) which served as a set of point-based fiducials for the performed experiments. A more detailed description of the imaging phantom can be found in the publications of Cash *et al.* [29, 25, 30] Imaging data of the described phantom were

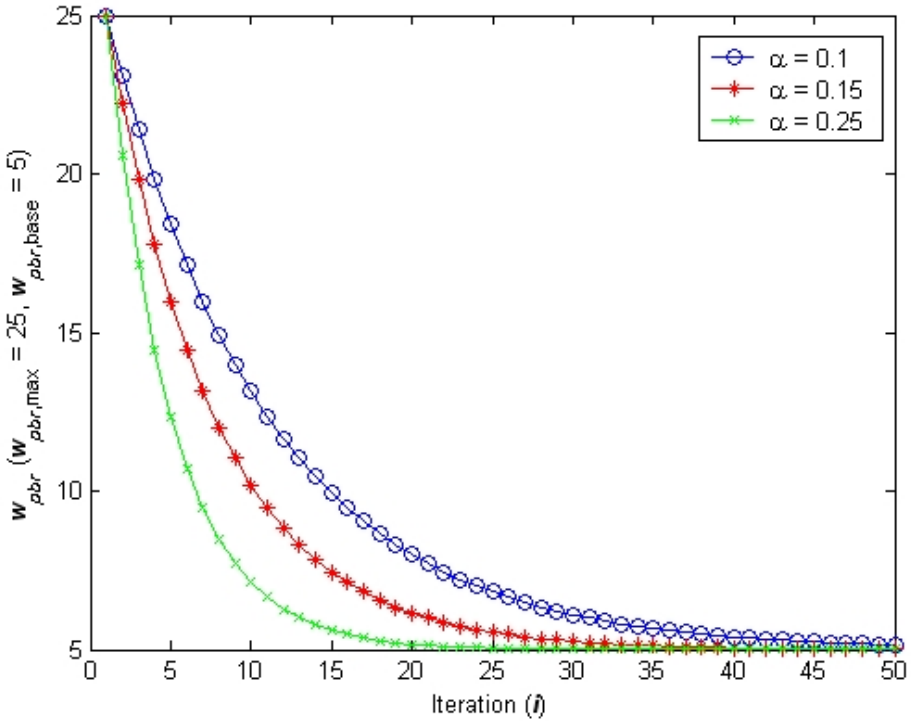

Figure III.4: Plots of dynamic PBR weighting factor function with various relaxation parameter (α) values. Decreasing the value of α increases the length of time that the patch region dominates the PBR at each iteration. As the value of α approaches zero the PBR weighting scheme becomes more akin to that proposed by Maurer *et al.* [90].

acquired using both CT (Mx8000, Phillips Medical Systems, Bothell, WA) and LRS (Real Scan 200C, 3-D Digital Corporation, Bethel, CT) modalities. The RealScan 200C is capable of acquiring spatially dense 3-D point cloud surface representations of 500 lines per scene with as many as 512 samples per line and a spatial resolution on the order of 0.5 mm. The scanner specifications state that the average deviation from planarity is 300 μm at 300 mm depth and 1000 μm at 800 mm depth. In addition to the geometrical data, a digital image of the LRS field of view is simultaneously acquired and texture mapped to the point cloud via a pre-determined calibration. A detailed validation of the imaging capabilities of the LRS system used has been provided by both Sinha *et al.* [139] and Cash *et al.* [29, 30]

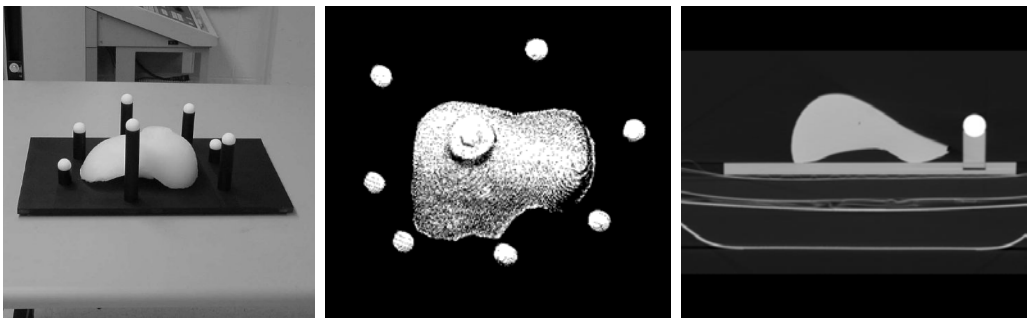

Figure III.5: Digital photograph (left), raw LRS scan (center) and sample CT slice (right) of imaging phantom. The silicon liver model, located in the center of the phantom, is surrounded by a set of seven white Teflon spheres. These spheres, which can be localized in both LRS and CT image spaces, are used in the determination of the "gold standard" ICP registration and serve as targets in the robustness studies.

Once imaging data were acquired, the sphere points were localized in the LRS scan using a least squares sphere fitting method described by Ahn *et al.* [1] and the sphere centroids were computed in the CT image volume using a region growing algorithm implemented within the Analyze software package (Analyze AVW Version 6.0, Mayo Clinic, Rochester, MN). Once the fiducial points and surfaces were extracted from both CT and LRS images, a PBR was computed using the seven sphere fiducial

points via Horn's quaternion method [76]. This PBR served as an initial alignment registration from which the "gold standard" ICP registration was computed using the entire LRS surface. Additionally, the sphere fiducials were also used as targets for computation of target registration error (TRE), defined by Fitzpatrick *et al.* [59], in the validation experiments.

Simulated falciform and inferior ridge patch regions were manually selected from the full LRS data as shown in Figure III.6. The "gold standard" ICP registration was then used to extract the analogous region on the CT image surface of the liver phantom. The CT image falciform region contained all the points within a 3 mm radius of each of the LRS surface falciform points. This was done to simulate segmentation errors in accurately delineating the homologous patch region on the image surface (shown in Figure III.6). Additionally, only a sub-region of the LRS data was used in the robustness studies since the LRS scans acquired intraoperatively very rarely contain the amount of surface information shown in the complete LRS scan. The region was selected based on the authors' experience of the most scanned regions during the observed surgical procedures (shown in Figure III.6).

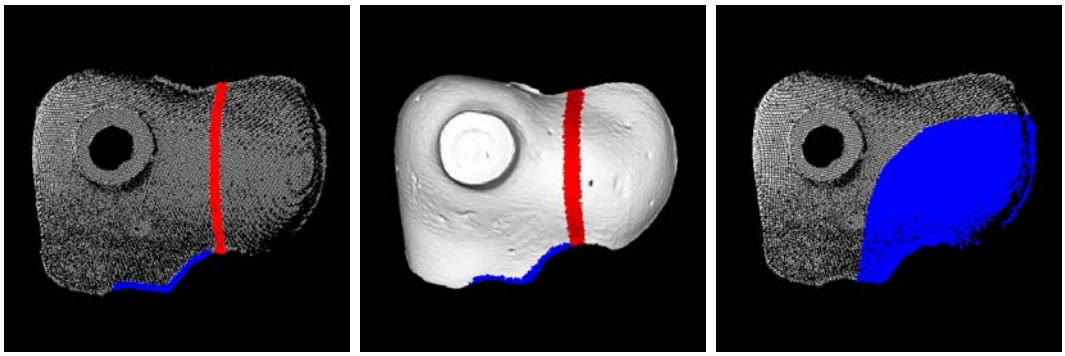

Figure III.6: Phantom LRS simulated falciform patch selected from full scan (left) was used to delineate the homologous region in the CT image surface (center). To more accurately simulate the typical LRS surface field of view obtained during surgery, a subregion of the LRS was manually selected for use in the robustness trials.

For reference, the number of points contained within the CT image liver surface, simulated falciform region, and simulated inferior ridge region were 106,661, 2,066, and 1,393, respectively. The number of points contained within the full and partial liver LRS scans were 34,546 and 12,376 with 1,125 and 802 falciform points in the respective full and partial scans. The number of inferior ridge points in the full and partial scans were 404 and 303, respectively.

Phantom Data Robustness Trials

In order to describe the robustness of the proposed algorithm, a series of registration experiments were performed which involved perturbing the LRS data from the "gold standard" ICP alignment with a random six degree-of-freedom, rigid-body transformation. The random transformations were computed by generating a set of six random parameters (three translation and three rotation). In order to simulate the variety of initial alignments corresponding with those provided by an anatomical fiducial PBR and without performing any initializing registration, two magnitudes of perturbation (termed "small scale" and "large scale") were utilized. The significance of performing robustness trials over two different magnitudes of perturbation is to test the hypothesis that utilizing salient feature information within the proposed algorithm provides the ability to reliably obtain reasonable surface registrations without the use of anatomical fiducial points to provide an initial pose. By alleviating the need to use an anatomical fiducial based PBR as an initial alignment, a primary error source in the current IGLS registration procedure will have been eliminated.

Three different surface registration methods were used for comparison within the robustness trials: traditional ICP, patch ICP using a single feature (falciform), and patch ICP using multiple features (falciform and inferior ridge). The "large scale" and "small scale" robustness trials were run over 250 perturbations per registration method and the data were compared in terms of sphere TRE and surface root mean

square (RMS) residuals (i.e. the RMS of the closest point distances between the source and target surfaces) provided by the registration algorithms. The parameters used for the ICP implementation for these trials were a maximum iteration number of 1000 and convergence criterion of $1e^{-4}$ mm RMS residual difference between iterations. The parameters used for the weighted patch ICP registration were as follows: 1000 maximum iterations, $w_{PBR,max} = 1000$, $w_{PBR,base} = 25$, $w_{PC} = 1e^{-4}$, $\alpha = 0.01$, and a convergence criterion of $1e^{-4}$ mm RMS residual difference between iterations.

A uniformly distributed random number generator was used to supply the rotation parameters $(\theta^x, \theta^y, \theta^z)$ and translation parameters (t^x, t^y, t^z) for the perturbation transformation matrices. For the "large scale" perturbation trials, the rotation parameters were generated on the interval [-180°,180°] (μ = -0.7$\pm$106.1) and the translation parameters were generated on the interval [-200 mm,200 mm] (μ = -3.4$\pm$119.3). For the "small scale" perturbation trials the intervals for the rotation and translation parameters were set to [-45°,45°] (μ = 0.6$\pm$26.6) and [-50 mm,50 mm] (μ = -1.0$\pm$28.9), respectively.

Clinical Validation

Clinical Image and Intra-operative Data Acquisition

Using an Institutional Review Board (IRB) approved patient protocol, CT or MR image sets and intra-operative data were acquired for six patients undergoing hepatic tumor resections at Barnes-Jewish Hospital in St. Louis, MO. The intra-operative protocol involved a series of pre-planned apneic periods during the acquisition to minimize errors in the data due to respiratory liver motion. The apneic periods were part of the IRB approved protocol and were performed at the same point of the respiratory cycle (end-expiration) such that the liver would reside approximately in the same location during each period of data acquisition. Specifically, the intra-operative protocol involved the acquisition of both anatomical point fiducial data

using an optically tracked probe (OPTOTRAK 3020, Northern Digital, Waterloo, Ontario) and LRS surface data. Further, the LRS unit used was optically tracked (description of the tracked LRS design provided by Sinha *et al.* [139] and Cash *et al.* [25, 30]) such that the anatomical fiducial data and the LRS surface data were both acquired relative to the same reference coordinate system.

Clinical Data Registration Experiments

The six clinically acquired data sets were then used in a set of registration trials to determine the effectiveness of the proposed patch ICP registration algorithm. For each data set, falciform and inferior ridge regions were segmented from both the pre-operative image surface and intra-operative LRS data. Comparisons were performed between the results obtained using a traditional ICP method, patch ICP using a single feature (falciform), and patch ICP using multiple features (falciform and inferior ridge). Additionally, registrations were performed under conditions of no initial pose transformation and an initial alignment provided by the anatomical fiducial based PBR. The parameters used for the ICP implementation for these trials were a maximum iteration number of 1000 and convergence criterion of $1e^{-4}$ mm RMS residual difference between iterations. The parameters used for the weighted patch ICP registration were as follows: 1000 maximum iterations, $w_{PBR,max} = 3000$, $w_{PBR,base} = 25$, $w_{PC} = 1e^{-4}$, $\alpha = 0.005$, and a convergence criterion of $1e^{-4}$ mm RMS residual difference between iterations.

Clinical Data Robustness Trials

Finally, one of the clinical data sets (patient 4) was used to perform robustness tests similar to those described for the phantom data. The particular clinical data set was chosen for the robustness trials due to the minimal soft tissue deformation in this particular case and the fact that the ICP registration provided a particularly

good alignment (shown in Figure III.7), based on visual inspection. For reference, the number of points containing the pre-operative liver, falciform, and inferior ridge regions derived from CT images were 57,873, 2,220, and 1,291, respectively. The number of points in the LRS scan representation of the liver, falciform, and inferior ridge regions for this clinical data set were 17,848, 594, and 101, respectively.

As in the phantom trials, three different surface registration methods were used for comparison within the robustness trials: traditional ICP, patch ICP using a single feature (falciform), and patch ICP using multiple features (falciform and inferior ridge). The "large scale" and "small scale" robustness trials were run over 250 perturbations per registration method and the robustness data is reported in terms of the RMS residual relative to the "gold standard" ICP registration. The parameters used for the ICP implementation for these trials were a maximum iteration number of 1000 and convergence criterion of $1e^{-4}$ mm RMS residual difference between iterations. The parameters used for the weighted patch ICP registration were as follows: 1000 maximum iterations, $w_{PBR,max} = 3000$, $w_{PBR,base} = 25$, $w_{PC} = 1e^{-4}$, $\alpha = 0.005$, and a convergence criterion of $1e^{-4}$ mm RMS residual difference between iterations.

As with the phantom robustness trials, a uniformly distributed random number generator was used to supply the rotation parameters $(\theta^x, \theta^y, \theta^z)$ and translation parameters (t^x, t^y, t^z) for the perturbation transformation matrices. For the "large scale" perturbation trials, the rotation parameters were generated on the interval [-180°,180°] (μ = -0.5±105.4) and the translation parameters were generated on the interval [-200 mm,200 mm] ($\mu = 5.5 \pm 113.3$). For the "small scale" perturbation trials the intervals for the rotation and translation parameters were set to [-45°,45°] (μ = 0.4±26.1) and [-50 mm,50 mm] ($\mu = 0.3 \pm 28.5$), respectively.

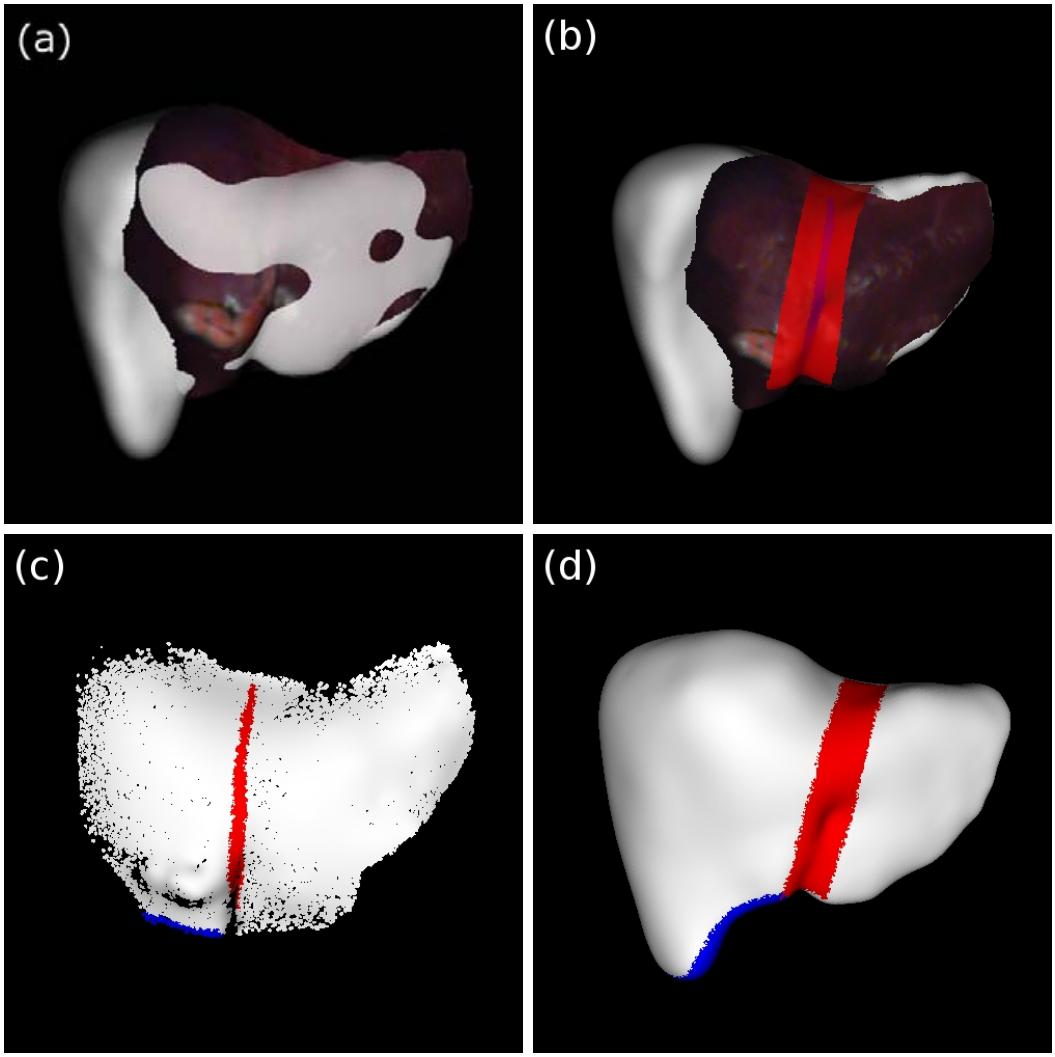

Figure III.7: Traditional ICP registration results (left) and overlaid image and falciform patch regions (right) for the clinical data used in the robustness trials (Patient 3). Note the large contrast in the accuracy of the alignment in this case than that shown in Figure III.1. The RMS residual for this registration was 3.4 mm. Note that for this data set the CT image and LRS surfaces contained 57,873 points and 19,863 points, respectively. The CT image and LRS falciform regions consisted of 3,148 and 594 points, respectively.

Results

Phantom Data Robustness Trials

The results of the "small scale" perturbation experiments over all 250 trials for each registration algorithm with respect to both RMS residual and sphere TRE values are shown in histogram format in Figure III.8. A summary of the results for the "small scale" perturbation robustness trials is shown in Table III.1. For reference, the PBR calculated between the CT and LRS sphere point sets yielded an FRE of 1.4 mm. The "gold standard" ICP registration based off this PBR gave a TRE of 2.3 mm and an RMS residual of 0.6 mm. Based on the distributions of the TRE values shown, a "failed" registration was defined as that which yielded a sphere TRE value of greater than 5.0 mm. The mean TRE for "failed" registrations for the ICP and patch ICP using a single feature were found to be 149.8±60.7 mm ($N = 118$) and 256.2±95.8 mm ($N = 7$), respectively.

Using aforementioned criterion to determine registration success, it can be seen in Figure III.8 and Table III.1 that the traditional ICP algorithm had a significantly higher failure rate than the patch ICP algorithm using both single and multiple features. Further, the weighted patch ICP algorithm using multiple patches provided successful registrations over all trials whereas using a single feature yielded failures for seven trials, suggesting that multiple features is more robust. It is also notable that the average RMS residual and sphere TRE values over the "successful" registrations is higher for the patch ICP method than those provided by the traditional ICP registration.

Table III.2 shows a summary of the results from the "large scale" perturbation robustness trials and Figure III.9 displays the results over all 250 trials in histogram format with respect to both RMS residual and sphere TRE values. As with the "small scale" perturbation trials, a "failed" registration was determined as that which

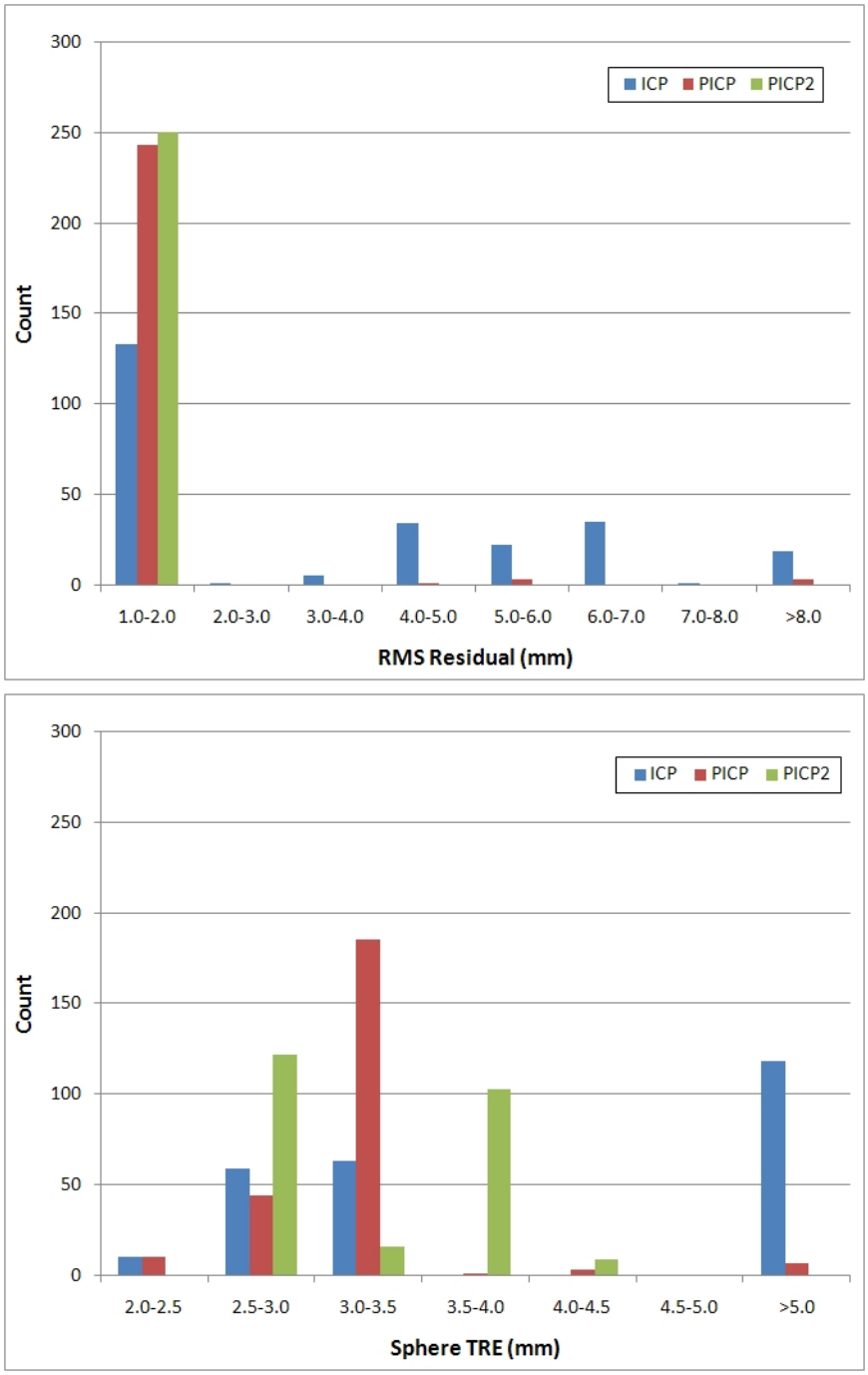

Figure III.8: Histogram representations of the RMS residual (top) and TRE (bottom) results from the "small scale" phantom robustness trials. Note that for these trials the "gold standard" RMS residual and TRE values were found to be 0.6 mm and 2.3 mm, respectively. Note the far greater number of ICP RMS residual results that fell >2 mm and TRE results that were >5 mm as compared to the weighted patch ICP results.

Registration method	Success (No.)	Residual (mm)	TRE (mm)	Successful Reg. Residual (mm)	Successful Reg. TRE (mm)
ICP	132 (52.8%)	3.0±2.9	72.1±81.4	0.6±0.002	2.7±0.2
PICP	243 (97.2%)	0.9±1.5	9.9±44.5	0.6±0.01	2.8±0.2
PICP2	250 (100%)	0.7±0.01	3.0±0.5	0.7±0.01	3.0±0.5

Table III.1: Summary of results for the "small scale" perturbation robustness trials using the phantom data set shown in Figure III.6 and histogram representation in Figure III.8. The number of successful trials (out of 250), RMS residual and TRE over all trails, and RMS residual and TRE over "successful" trials is reported for each registration method. A "successful" trial is determined as that which yields a TRE of less than 5.0 mm. For reference, the "gold standard" ICP registration for the phantom yielded RMS residual and TRE values of 0.6 mm and 2.3 mm, respectively.

yielded a sphere TRE value larger than 5.0 mm. The mean TRE values for "failed" registrations for the ICP and patch ICP using a single feature were found to be 240.1±43.5mm ($N = 239$) and 293.9±24.0 mm ($N = 127$), respectively. Similar to the results for the "small scale" perturbation trials, the rate of failure of the patch ICP registration method is significantly lower than that of the traditional ICP method and the use of multiple features provides successful registration methods over all "large scale" perturbation trials.

Registration method	Success (No.)	Residual (mm)	TRE (mm)	Successful Reg. Residual (mm)	Successful Reg. TRE (mm)
ICP	11 (4.4%)	5.4±2.4	229.7±64.7	0.6±0.002	2.5±0.3
PICP	123 (49.2%)	4.6±4.9	150.7±146.8	0.6±0.01	2.9±0.3
PICP2	250 (100%)	0.7±0.003	2.9±0.5	0.7±0.003	2.9±0.5

Table III.2: Summary of results for the "large scale" perturbation robustness trials using the phantom data set shown in Figure III.6 and histogram representation in Figure III.9. The number of successful trials (out of 250), RMS residual and TRE over all trails, and RMS residual and TRE over "successful" trials is reported for each registration method. A "successful" trial is determined as that which yields a TRE of less than 5.0 mm. For reference, the "gold standard" ICP registration for the phantom yielded RMS residual and TRE values of 0.6 mm and 2.3 mm, respectively.

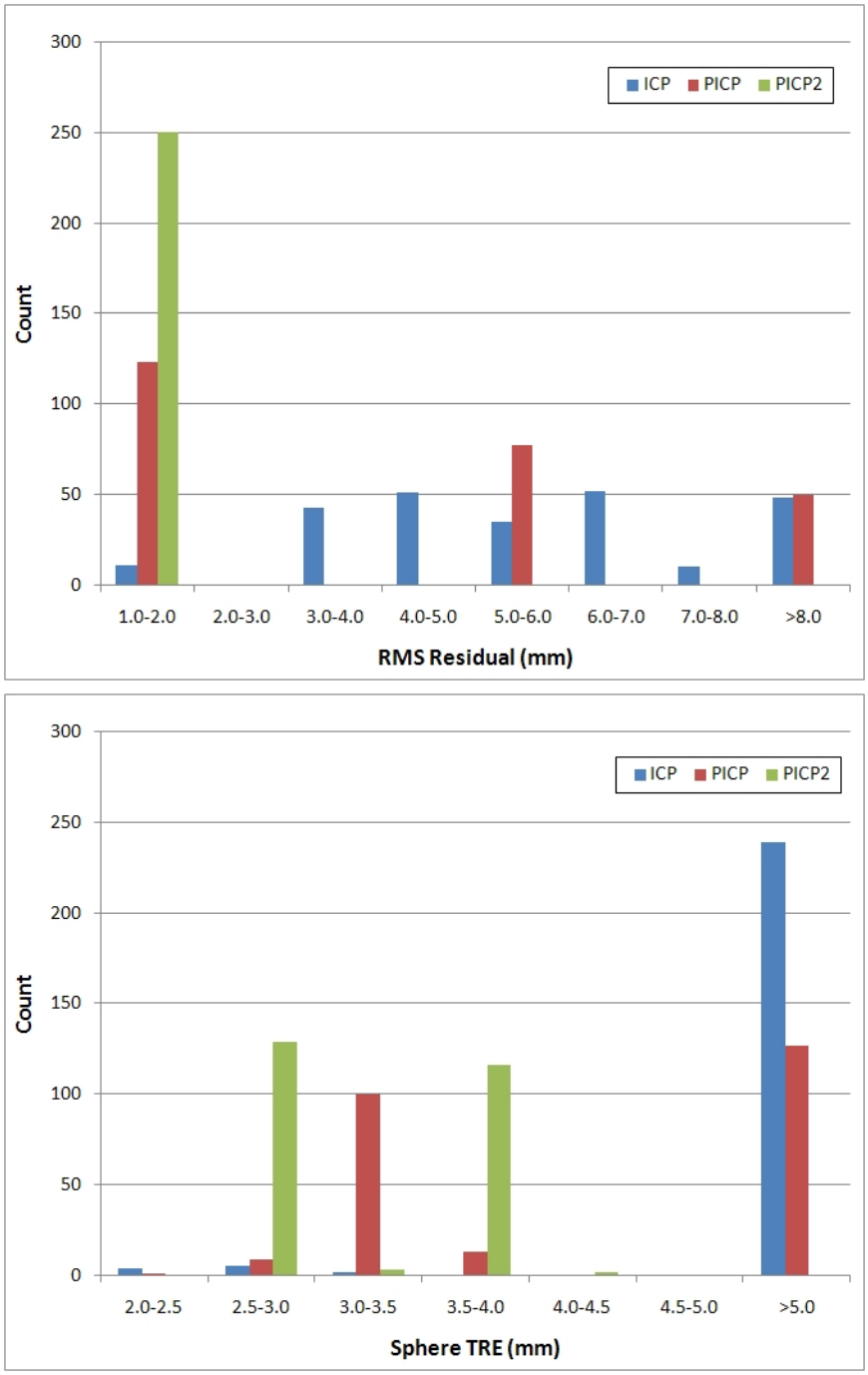

Figure III.9: Histogram representations of the RMS residual (top) and TRE (bottom) results from the "large scale" phantom robustness trials. Note that for these trials the "gold standard" RMS residual and TRE values were found to be 0.6 mm and 2.3 mm, respectively. Note the far greater number of ICP RMS residual results that fell >2 mm and TRE results that were >5 mm as compared to the weighted patch ICP results.

Clinical Data Registration Experiments

Summaries of the clinical data registration experiments in terms of the RMS residual obtained by the performed registration method and over the six patients are shown in Table III.3 and Table III.4. The results are shown for the ICP, patch ICP with single feature, and patch ICP with multiple features using both the anatomical fiducial based PBR initial alignment (Table III.4) and with no initial pose transformation (Table III.3). In addition to reporting the RMS residuals over the entire surfaces, "feature errors" were computed for each registration result as RMS residuals of the homologous patch regions. For the feature errors, feature 1 indicates the falciform ligament region and feature 2 represents the inferior ridge. The registrations that yielded gross misalignments are indicted with a superscript, which was evaluated via visual inspection. The most notable result shown in Tables III.3 and III.4 is the fact that given no initial alignment, the traditional ICP method was unable to provide a reasonable alignment for any of the clinical data sets. However, the multiple feature patch ICP algorithm yielded reasonable alignment for all cases even without any initial alignment. Further, it is apparent that the patch ICP algorithm with a single patch is not quite as robust as that using multiple patches since the single patch ICP trials yield gross misalignments for two of the patients when no initial pose is provided.

In addition to reporting numerical summaries, visualizations of the clinical data registrations for all six patients are shown in Figure III.10 through Figure III.15. The visualizations shown are the results of the ICP (panels (a) and (b)) and patch ICP using a single feature (panels (c) and (d)) given the anatomical fiducial PBR initial alignment. The results of the patch ICP registration with multiple features given no initial alignment is also shown (panels (e) and (f)) for the six patients. For each of the

	RMS Residual (mm)			Feature 1 Error (mm)			Feature 2 Error (mm)		
Patient	ICP	PICP	PICP2	ICP	PICP	PICP2	ICP	PICP	PICP2
1	5.2†	4.5	4.7	40.2†	1.7	1.8	107.1†	3.0	1.7
2	5.7†	6.2	7.0	43.9†	3.8	4.9	61.8†	10.9	3.4
3	7.3†	5.5	6.2	86.3†	2.6	4.2	106.3†	12.5	7.2
4	7.5†	10.8†	3.7	64.4†	7.1†	3.5	140.6†	46.3†	5.9
5	11.6†	6.6	6.4	138.6†	3.2	3.5	11.6†	5.4	5.0
6	11.3†	10.8†	5.9	74.5†	4.1†	3.7	37.5†	104.4†	3.3

Table III.3: Summary of the registration results for the six clinical data sets using no initial alignment transformation. The results are shown for the ICP, patch ICP registration with a single feature (PICP), and patch ICP registration with multiple features (PICP2) in terms of the RMS residual between the entire surfaces as well as the homologous patch regions. Feature 1 represents the falciform ligament region and feature 2 denotes the inferior ridge region. Grossly misaligned registrations are noted with a superscript (†) and were determined by visual inspection.

	RMS Residual (mm)			Feature 1 Error (mm)			Feature 2 Error (mm)		
Patient	ICP	PICP	PICP2	ICP	PICP	PICP2	ICP	PICP	PICP2
1	2.8	4.6	4.7	35.9	1.8	1.8	5.0	2.7	1.7
2	5.2†	5.7	7.0	63.5†	3.1	4.9	39.9†	38.6	3.4
3	5.2	5.5	6.2	7.1	2.8	4.2	10.4	11.5	7.2
4	3.4	3.5	3.7	3.9	3.7	3.5	7.1	7.2	5.8
5	3.4	6.5	6.4	30.2	3.1	3.5	5.3	8.6	5.0
6	5.4	5.6	5.9	4.3	2.9	3.7	5.9	6.5	3.3

Table III.4: Summary of the registration results for the six clinical data sets using the anatomical fiducial based PBR initial alignment. The results are shown for the ICP, patch ICP registration with a single feature (PICP), and patch ICP registration with multiple features (PICP2) in terms of the RMS residual between the entire surfaces as well as the homologous patch regions. Feature 1 represents the falciform ligament region and feature 2 denotes the inferior ridge region. Grossly misaligned registrations are noted with a superscript (†) and were determined by visual inspection.

registrations performed, the patch regions are highlighted in both the pre-operative image surface (red) and intra-operative LRS data (blue).

Similar to that shown in Tables III.3 and III.4, the most notable result is the fact that the patch ICP algorithm using multiple features with no initial alignment was able to provide similar results to those obtained by both the ICP and single feature patch ICP given the anatomical fiducial PBR initial pose. Further, for several of the patients, the patch ICP registration provides a much more reasonable alignment as compared with that provided by the traditional ICP method. Most noticeably, for patient 2 (shown in Figure III.11) the ICP registration resulted in a gross misalignment of the surfaces, even given the anatomical fiducial PBR initial alignment, where the LRS scan of the anterior liver surface was aligned with the posterior surface. The improvement in the surface alignment provided by the weighted patch ICP algorithm is also visible in the registration for patient 1 shown in Figure III.10. Specifically, the alignment near the umbilical fissure is significantly improved relative to the ICP registration result. Similar to the results for patient 1, the alignment provided by the weighted patch ICP algorithm for patient 5 seems to be an improvement in comparison of that provided by the traditional ICP method (see Figure III.14). This is shown, specifically, by the alignment near the region of the umbilical fissure between segments III and IV of the liver surface. The improved alignments for patients 1, 2, and 5 using the weighted patch ICP algorithm is also supported by the lower feature error results shown in Tables III.3 and III.4.

Clinical Data Robustness Trials

The clinical robustness results for the "small scale" perturbation trials are summarized in Table III.5. Additionally, a histogram representation of the "small scale" perturbation experiments over all 250 trials for each registration algorithm with respect to RMS residual is shown in Figure III.16. For reference, the RMS residual of

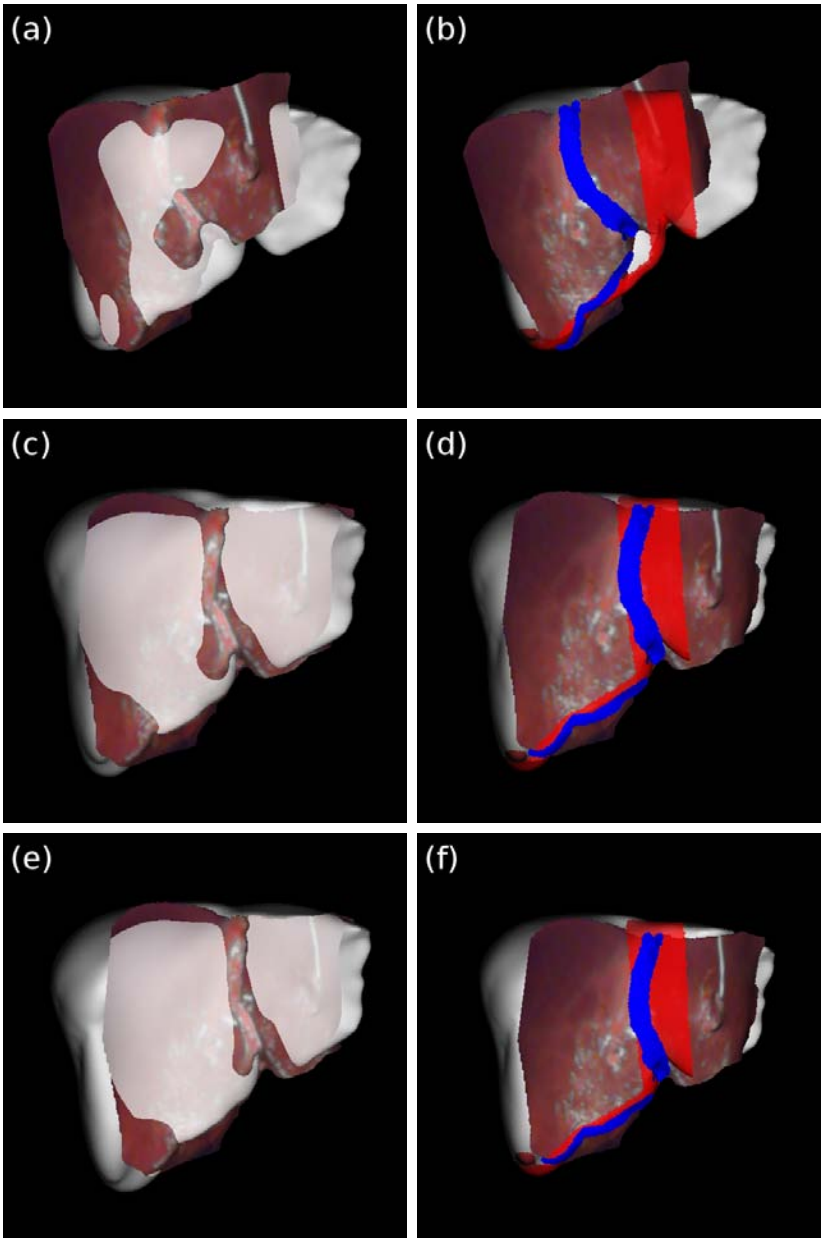

Figure III.10: Clinical results for Patient 1 showing visualizations of the ICP registration (a-b) and patch ICP registration using a single (falciform) patch (c-d) initialized using the anatomical fiducial PBR, as well as patch ICP registration using multiple patches (falciform and inferior ridge) given no initial alignment registration (e-f). The LRS and ICP inferior ridge and falciform patches are highlighted for the ICP and patch ICP registrations in (b,d,f). The ICP registration shows an apparent misalignment which is corrected via the proposed method.

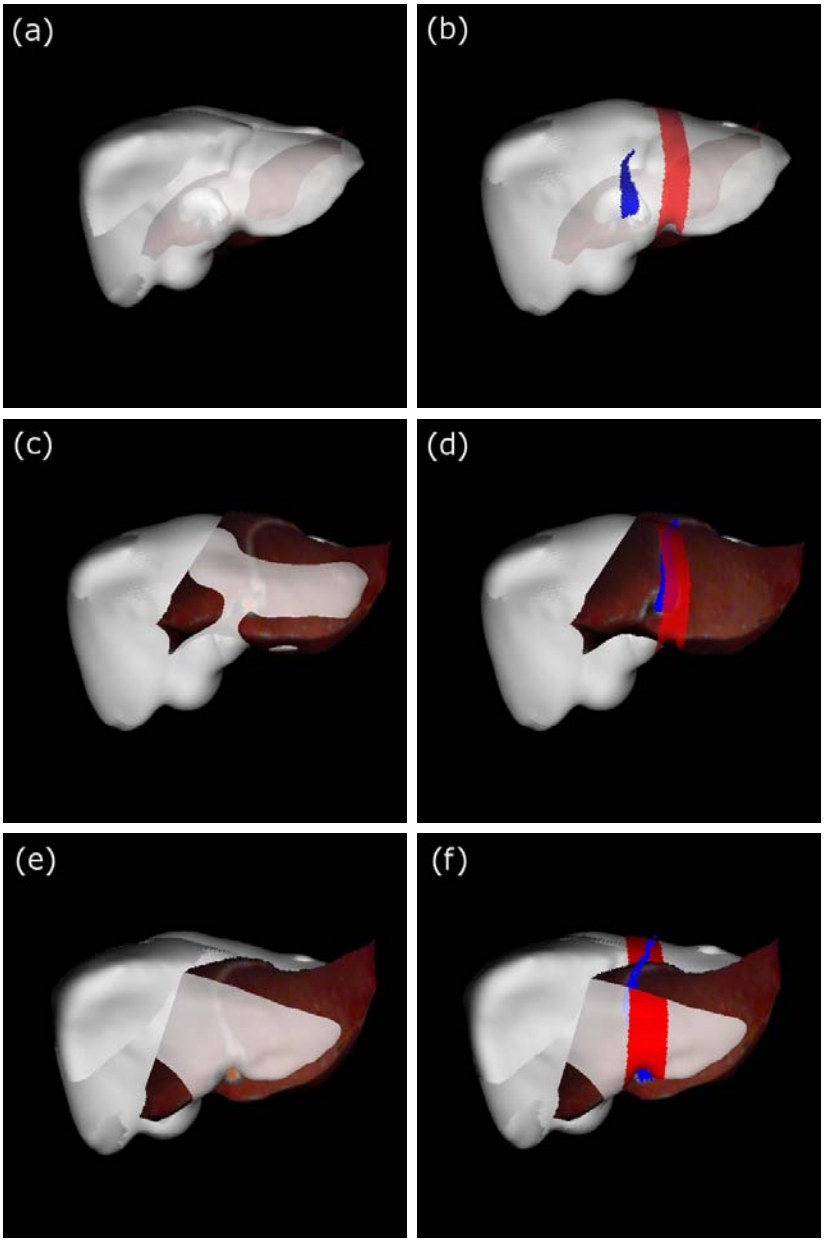

Figure III.11: Clinical results for Patient 2 showing visualizations of the ICP registration (a-b) and patch ICP registration using a single (falciform) patch (c-d) initialized using the anatomical fiducial PBR, as well as patch ICP registration using multiple patches (falciform and inferior ridge) given no initial alignment registration (e-f). The LRS and ICP falciform patches are highlighted for the ICP and patch ICP registrations in (b,d,f). The ICP registration shows a gross misalignment which is corrected via the proposed method.

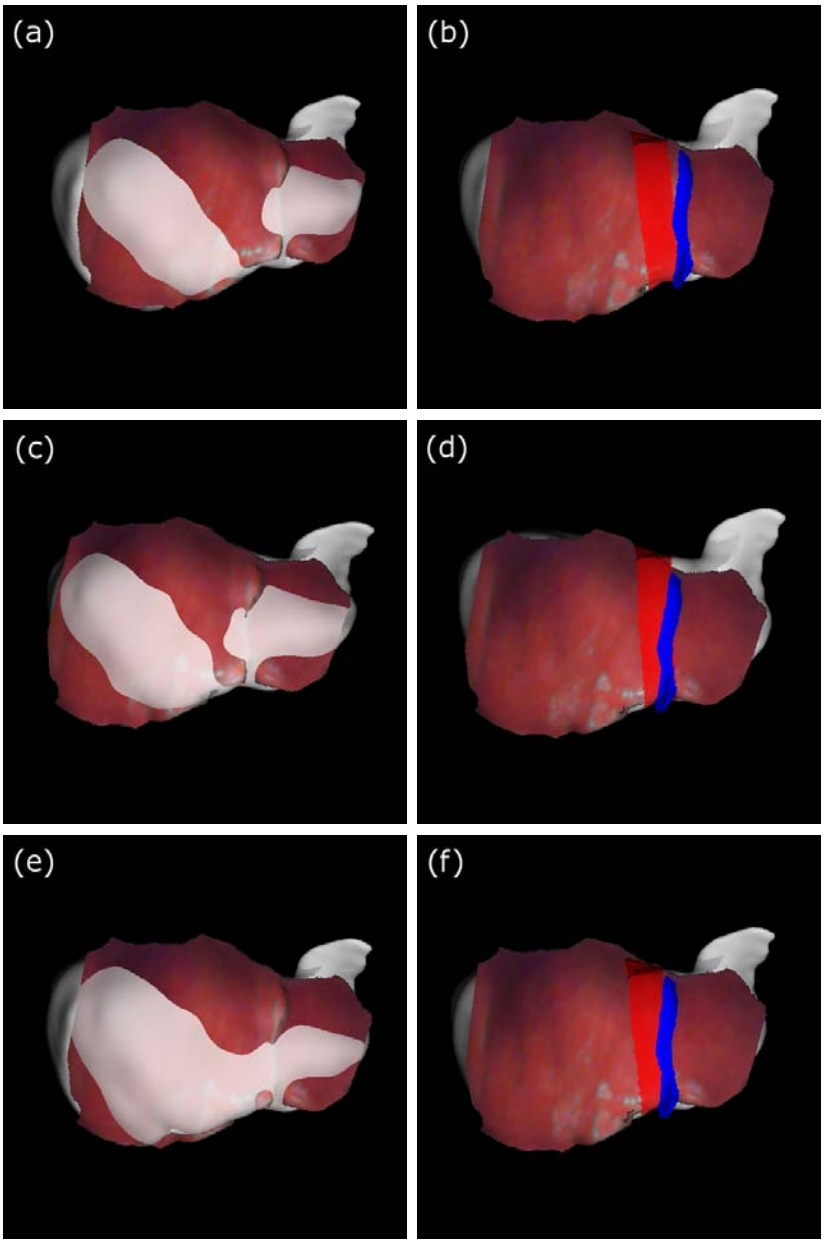

Figure III.12: Clinical results for Patient 3 showing visualizations of the ICP registration (a-b) and patch ICP registration using a single (falciform) patch (c-d) initialized using the anatomical fiducial PBR, as well as patch ICP registration using multiple patches (falciform and inferior ridge) given no initial alignment registration (e-f). The LRS and ICP falciform patches are highlighted for the ICP and patch ICP registrations in (b,d,f).

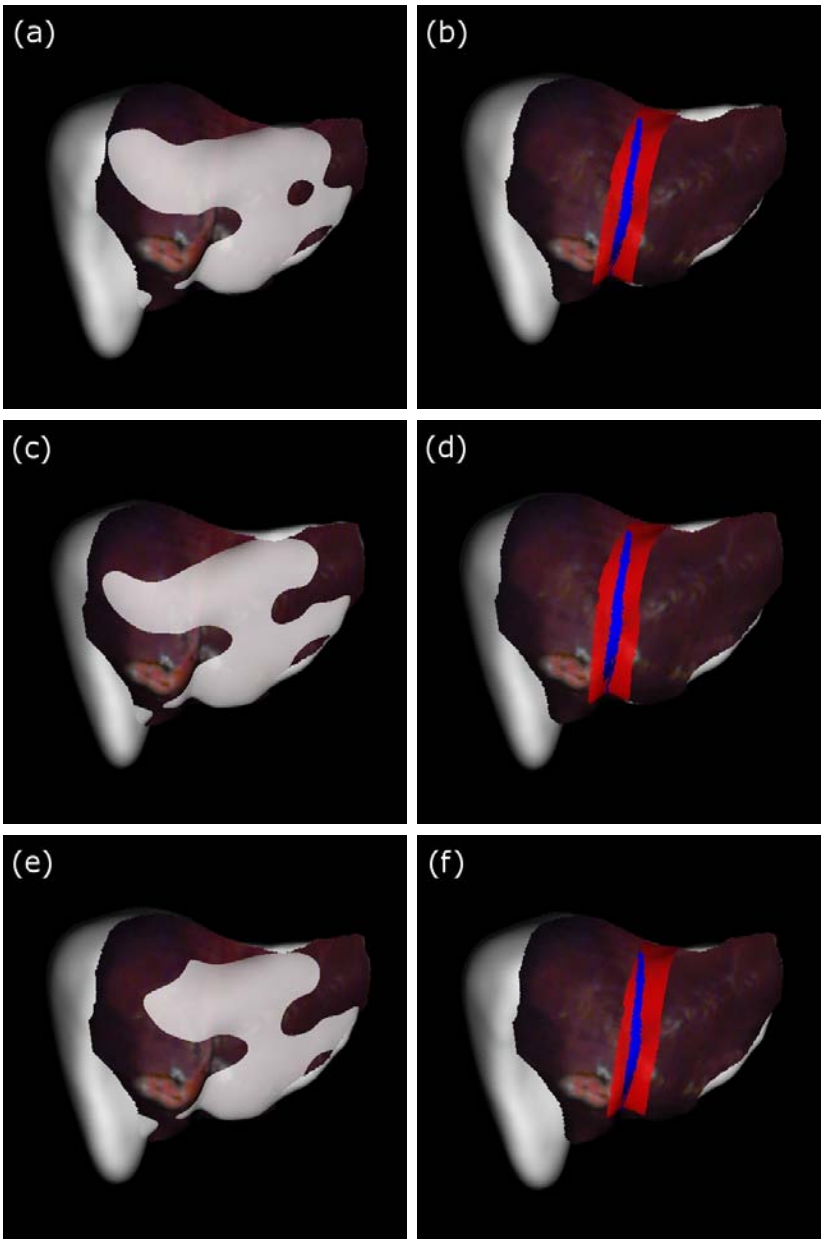

Figure III.13: Clinical results for Patient 4 showing visualizations of the ICP registration (a-b) and patch ICP registration using a single (falciform) patch (c-d) initialized using the anatomical fiducial PBR, as well as patch ICP registration using multiple patches (falciform and inferior ridge) given no initial alignment registration (e-f). The LRS and ICP falciform patches are highlighted for the ICP and patch ICP registrations in (b,d,f).

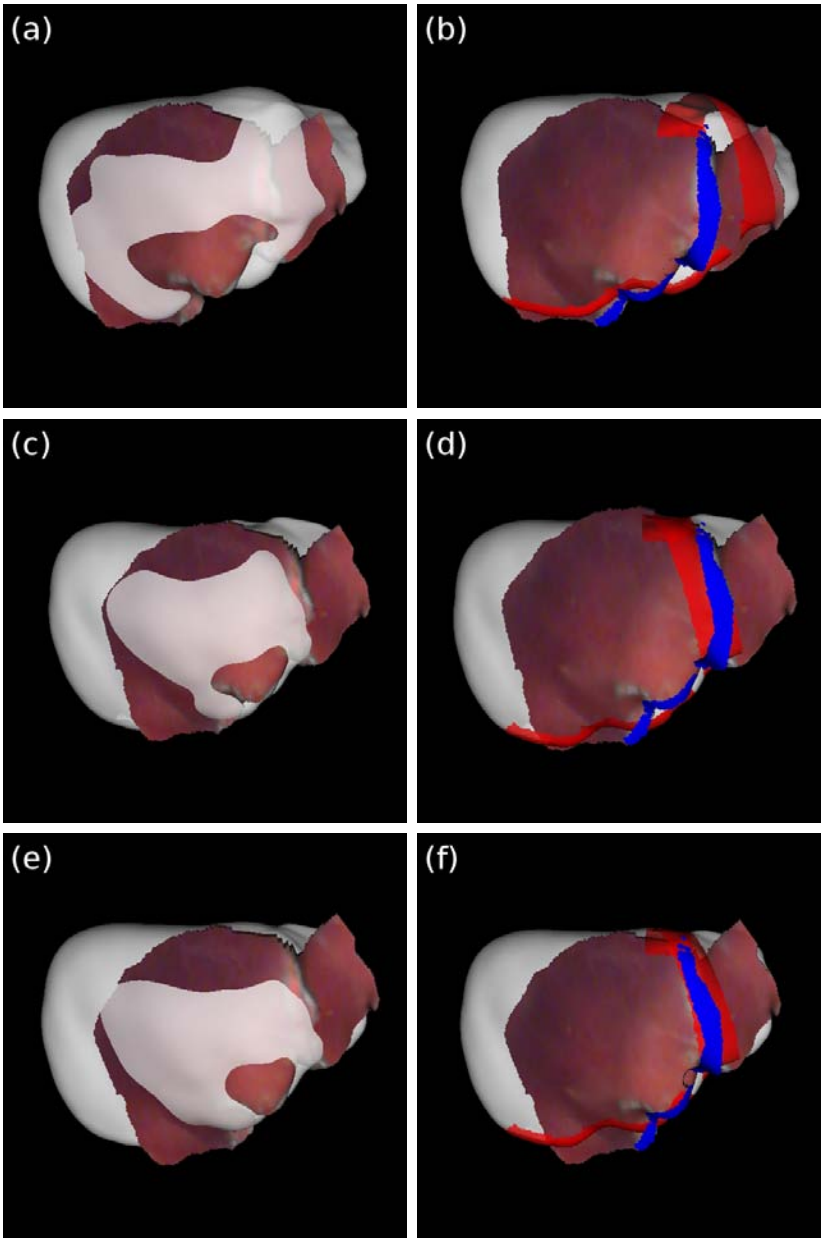

Figure III.14: Clinical results for Patient 5 showing visualizations of the ICP registration (a-b) and the patch ICP registration using a single (falciform) patch (c-d) initialized using the anatomical fiducial PBR, as well as patch ICP registration using multiple patches (falciform and inferior ridge) given no initial alignment registration (e-f). The LRS and ICP inferior ridge and falciform patches are highlighted for the ICP and patch ICP registrations in (b,d,f). The ICP registration shows an apparent misalignment which is corrected via the proposed method.

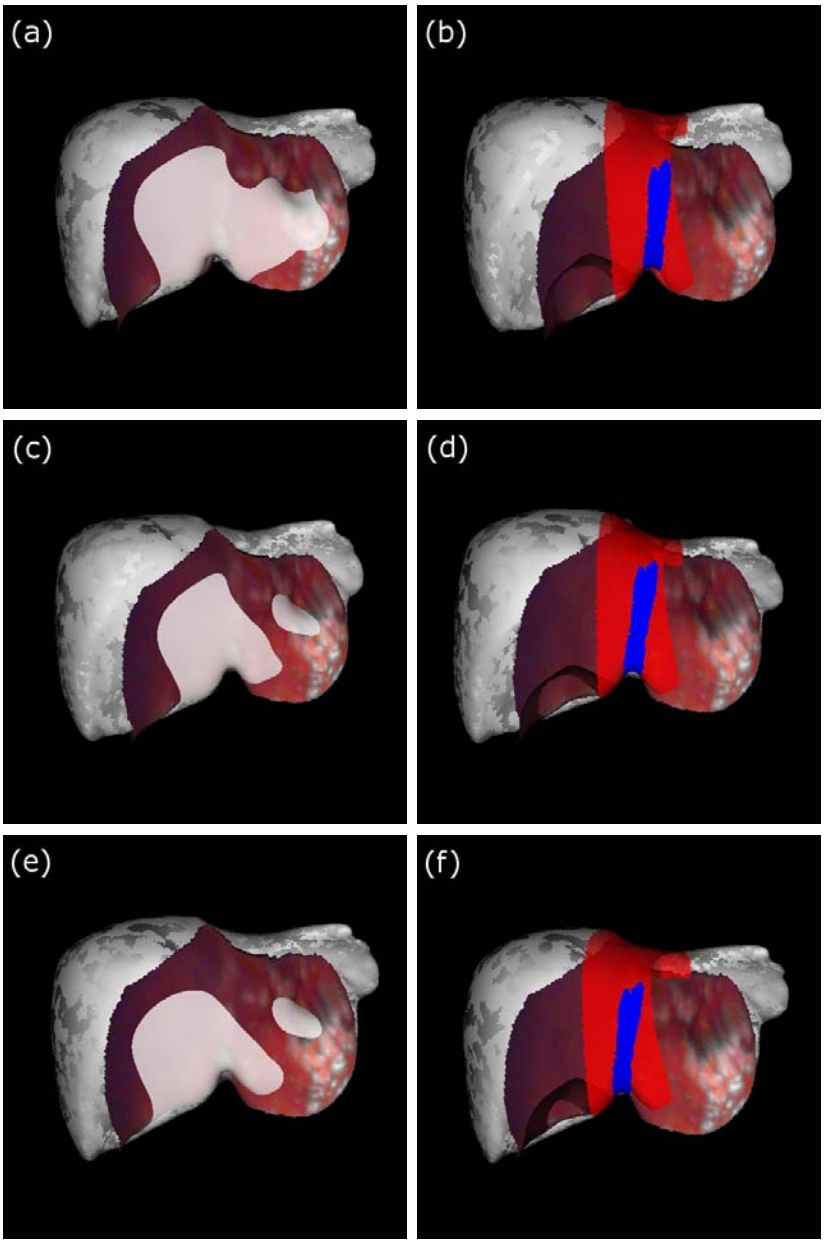

Figure III.15: Clinical results for Patient 6 showing visualizations of the ICP registration (a-b) and patch ICP registration using a single (falciform) patch (c-d) initialized using the anatomical fiducial PBR, as well as patch ICP registration using multiple patches (falciform and inferior ridge) given no initial alignment registration (e-f). The LRS and ICP falciform patches are highlighted for the ICP and patch ICP registrations in (b,d,f).

the "gold standard" ICP registration in this case was found to be 3.4 mm, which is shown in Figure III.7. Based on the distribution of RMS residuals shown, a "failed" registration was determined to be one which yielded an RMS residual of greater than 5.0 mm. The mean RMS values >5.0 mm for the ICP and patch ICP using a single feature were found to be 6.6±0.9 mm ($N = 63$) and 15.9±4.8 mm ($N = 22$), respectively. Similar to that shown by the results of the phantom "small scale" robustness trials, the traditional ICP algorithm was shown to have a higher "failure" rate than both the single feature and multiple feature patch ICP algorithm. Further, over the "successful" registrations the mean RMS residual provided by the ICP algorithm is lower than either the patch ICP using a single feature and using multiple features. The higher RMS residuals over the successful trials is expected for the patch ICP algorithm based on the fact that utilizing the salient features imposes constraints on the final alignment.

Registration method	Success (No.)	Residual (mm)	Residual (Success) (mm)
ICP	187 (74.8%)	4.2±1.4	3.4±5e-4
PICP	228 (91.2%)	4.7±3.8	3.6±0.014
PICP2	250 (100%)	3.7±0.05	3.7±0.1

Table III.5: Summary of results for the "small scale" perturbation robustness trials using the clinical data set shown in Figure III.7 and histogram representation in Figure III.16. The number of successful trials (out of 250), mean residual over all trails, and mean residual over "successful" trials is reported for each registration method. A "successful" trial is determined as that which yields a RMS residual of less than 5.0 mm over the entire surface. For reference, the "gold standard" ICP registration (shown in Figure III.7) yielded an RMS residual of 3.4 mm.

Table III.6 shows a summary of the results of the "large scale" perturbation trials for the clinical data and Figure III.16 depicts a histogram representation of the RMS residual data obtained by the 250 trials of the "large scale" perturbation experiment over the three registration methods. As with the "small scale" trials, a "failed" registration was defined as that which yielded an RMS residual of greater than 5.0

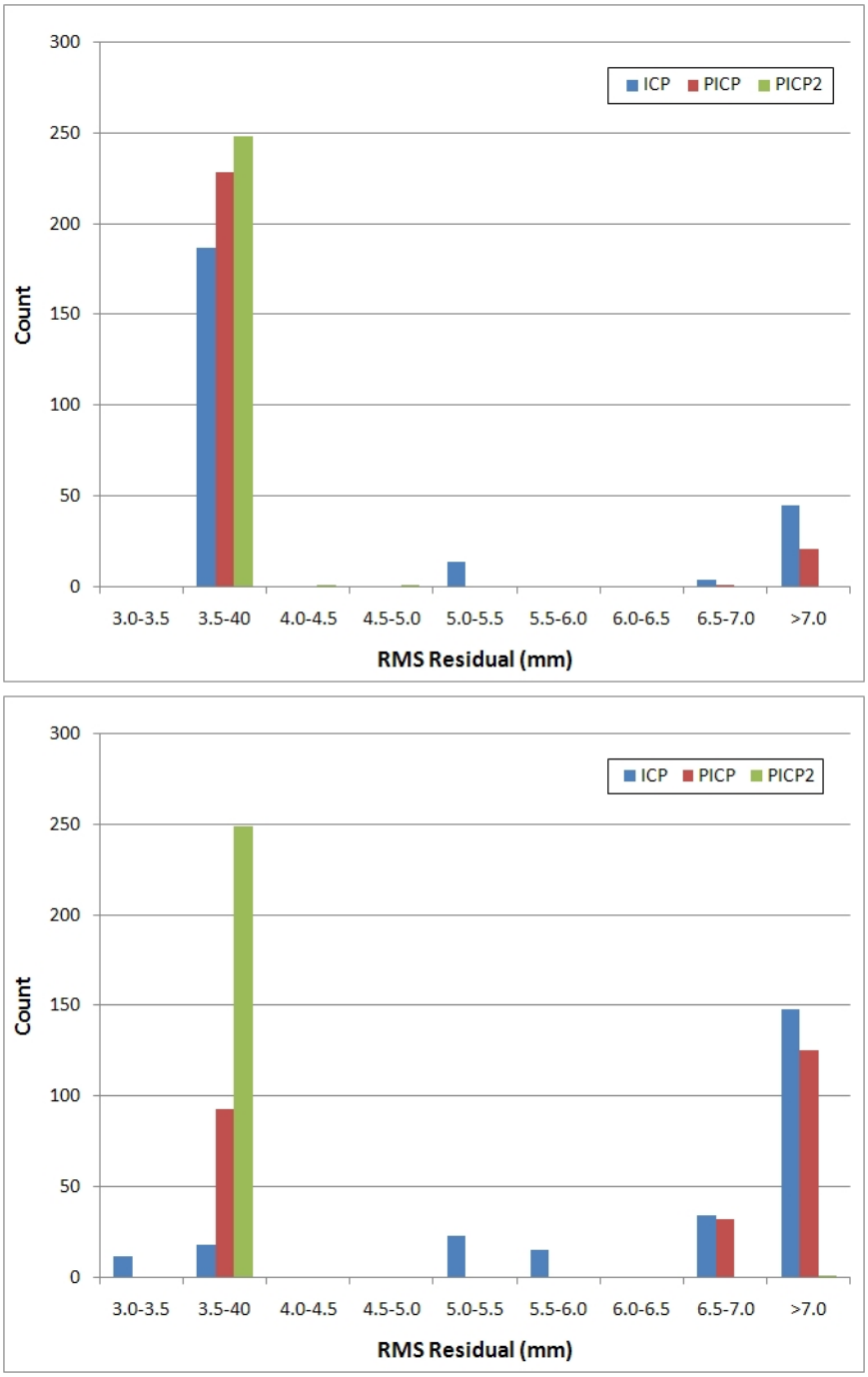

Figure III.16: Histogram representation of the RMS residual data obtained from "small scale" (top) and "large scale" (bottom) robustness trials performed on clinical data (Patient 3). The "gold standard" ICP registration is shown in Figure III.7 and this registration yielded an RMS residual of 3.4 mm. Note the drastic improvement in robustness provided by the patch ICP method with multiple features (PICP2).

Registration method	Success (No.)	Residual (mm)	Residual (Success) (mm)
ICP	30 (12.0%)	7.3±2.6	3.3±0.2
PICP	93 (37.2%)	8.9±5.6397	3.6±0.01
PICP2	249 (99.6%)	3.7±0.5	3.7±0.01

Table III.6: Summary of results for the "large scale" perturbation robustness trials using the clinical data set shown in Figure III.7 and histogram representation in Figure III.16. The number of successful trials (out of 250), mean residual over all trials, and mean residual over "successful" trials is reported for each registration method. A "successful" trial is determined as that which yields a RMS residual of less than 5.0 mm over the entire surface. For reference, the "gold standard" ICP registration (shown in Figure III.7) yielded an RMS residual of 3.4 mm.

mm. The mean RMS values for "failed" registrations for the ICP and patch ICP using a single feature were found to be 7.9±2.2 mm ($N = 220$) and 12.0±4.9 mm ($N = 157$), respectively. The results shown in TableIII.6 and Figure III.16 provide similar results as those shown in both the phantom and clinical robustness trials. Based on the incidence of the "failed" registrations, the patch ICP implementation, specifically the one that utilized multiple features, provides a much more robust method with which to achieve reasonable alignments. However, in the "large scale" trials, the multiple feature weighted patch ICP implementation failed on one of the trials. By modifying the algorithm parameters ($w_{PBR,max} = 4000$ and $\alpha = 0.001$) for the particular random perturbation transform that resulted in a failure, it was found that the multiple feature patch ICP algorithm was able to achieve a reasonable alignment for this case.

Discussion

Weighted Patch ICP Robustness and Validation

The data presented from both the phantom and clinical studies provide strong evidence that the proposed weighted patch ICP algorithm is more robust to poor initial alignment than the traditional ICP method. Further, it is reasonable to conclude from this work that by including the multiple features (falciform and inferior

ridge) and the correct algorithm parameters, the weighted patch ICP algorithm can provide alignments under virtually any possible initial pose routinely experienced during surgery. The ability to circumvent the need to provide an initial alignment registration is quite powerful in the case of IGLS, since the determination of this transformation is the most error prone step within the current process. As mentioned previously, the accurate determination of homologous, rigid anatomical landmarks is complicated in the case of IGLS due to amount of deformation and non-rigid movement of the liver upon laparotomy and mobilization. A success or failed registration for the phantom robustness trials is much easier to determine than for the clinical experiments since the liver phantom data set includes a set of target points from which the TRE of the transformations can be determined. Being that we do not currently have the ability to acquire accurate sub-surface targeting data in a clinical setting, the RMS residual between the two surfaces is the only metric that can be used to evaluate the alignments in the clinical data experiments.

While the RMS residual between two surfaces is not the most objective measure of registration accuracy, it is highly unlikely that registrations resulting in large RMS residuals correspond with reasonable alignments. While it is quite possible that incorrect alignments may still provide small RMS residuals (as shown by the RMS residuals of the ICP alignments for patient 2 in Tables III.3 and III.4), the comparatively large number of high RMS residual alignments resulting from the traditional ICP implementation under condition of both "small scale" and "large scale" perturbation in initial pose (shown in Table III.5, Table III.6, and Figure III.16) suggests that the proposed weighted ICP algorithm is much more robust. Further, the patch ICP registration algorithm provided much improved registrations for three of the sets (patients 1, 2, and 5) of clinical data where the traditional ICP method resulted in obvious misalignments as determined by visualization and further indicated by the significantly lower feature error measurements indicated in Tables III.3 and III.4.

Algorithm Parameter Selection and Optimization

One of the primary advantages of the proposed algorithm is the use of the dynamic PBR weighting scheme described by Equation III.3. This dynamic weight factor allows for the registration to be significantly biased towards patch alignment at early iterations, while utilizing this patch alignment as an anchor at later iterations. The fact that the registration is so heavily biased towards the alignment of the patch regions at the early iterations of the algorithm provides the means by which variations in initial alignment are rendered less significant to the final outcome. Further, by lowering the PBR weight factor of the patch points at later iterations the remaining surface information is utilized to provide a more unbiased alignment of the surfaces. Additionally, the dynamic weighting scheme also compensates for segmentation errors in the delineation of exactly homologous patch regions. Since the non-patch regions of the surfaces play a more significant role later in the registration process, the registration is given the opportunity to converge to a more globally correct alignment.

For the phantom and clinical robustness trials and registrations performed in this work, all of the algorithm parameters were determined empirically via real-time visualization of the behavior of the proposed registration method and retrospective analysis of the registration results for the sample initial alignments of the phantom and clinical data sets. Ultimately, the factors that dictate the parameters required for the proposed weighted patch ICP algorithm to achieve reasonable alignments are the quality of the initial pose and the relative fraction of source (i.e. LRS scan) feature points to total source points. It stands to reason that the algorithm will require a higher maximum PBR weighting factor ($w_{PBR,max}$) and smaller relaxation parameter (α) when the fraction of source patch points is relatively small and/or the initial alignment is extremely poor.

In terms of parameter determination, the primary difference between the clinical

and phantom data sets is the relative fraction of the source (i.e. LRS scan) data that the anatomical features comprise. For example, the salient patch regions (falciform and inferior ridge) for the phantom data comprise approximately 9% of the total source points while these features represent only 4% of the total source points in the clinical data set used in the perturbation studies. Based on the differences in the relative fraction of patch points to total size of the LRS data between the phantom and clinical data sets, it can be seen that if a smaller fraction of the source data is comprised of patch regions then a larger value of the maximum patch PBR weight factor ($w_{PBR,max}$) and smaller value of the relaxation constant (α) are required to achieve similar algorithm robustness.

In order to optimize the parameter selection for a given data set it is important to take several points into consideration. As discussed in previous paragraph, the values of the maximum patch PBR weight factor ($w_{PBR,max}$) and the relaxation constant (α) are directly dependent on the relative fraction of points that are contained in the patch point data sets. It is important that α not be too small and that $w_{PBR,base}$ not be too large, less the algorithm be too heavily biased to patch regions at later iterations. Biasing towards the patch regions too heavily throughout the registration process could lead to less optimal alignments since, in most cases, the source data (i.e. LRS scan) will not contain data to represent the entire region delineated from the pre-operative image set. Optimizing the value for the point correspondence weight factor (w_{PC}) is a bit more obvious, as the only negative effect of an extremely small value for this factor would be to potentially increase negative effects of over segmentation of the anatomical features in the LRS data or outliers contained in the source patch data. These effects are more appropriately minimized by conservative segmentation of the salient anatomical features in the LRS data.

Segmentation Effects on Algorithm Performance

While the preliminary data is promising, a number of caveats exist with the proposed algorithm in its current form. In contrast to the ease of accurately delineating the falciform region within the LRS data, the ability to accurately segment the falciform region, based on the surface groove, is highly dependant on patient anatomy, image quality, and the quality of segmentation. As one would expect, if the segmentations of the salient anatomical features are grossly inaccurate, then the algorithm will most likely provide grossly inaccurate alignments. Based on the current implementation, however, favorable results can be facilitated by being a little more conservative in the segmentation of the LRS anatomical patches while being a bit more liberal in the pre-operative anatomical feature delineation. As long as homologous target patch points exist for all source patch points (the opposite does not have to be true), the current implementation will not cause a bias towards an incorrect registration.

Concerns Regarding Intra-operative Implementation

Being that the proposed algorithm requires additional point searches to be performed at each iteration of the algorithm, one of the potential concerns for intra-operative implementation is the increase in computation time. In order for the guidance information provided by IGLS to be relevant and useful, the ability to compute the registration must be as fast as possible. In order to address this concern, k-d dimensional trees were used to decrease point search times [162, 61] for both the ICP and weighted patch ICP implementations used in the aforementioned studies.

To more accurately characterize the effects of the computational overhead imposed by additional point searches, the time to solution for each trial within the robustness studies performed for both the clinical and phantom data sets were recorded. A summary of the timing data is shown in Table III.7, which displays the average times to solution both in terms of total time (in seconds) and in time per iteration (in

Registration method	"Small scale" trials		"Large scale" trials	
	Phantom (sec / sec/itr)	Clinical (sec / sec/itr)	Phantom (sec / sec/itr)	Clinical (sec / sec/itr)
ICP	60.77 / 0.24	70.73 / 0.37	59.06 / 0.24	92.04 / 0.37
PICP	76.77 / 0.34	88.99 / 0.54	108.09 / 0.38	141.87 / 0.62
PICP2	43.60 / 0.36	52.70 / 0.51	52.08 / 0.38	54.77 / 0.54

Table III.7: Comparative summary of the time to solution of each algorithm under the condition of "large scale" and "small scale" perturbations for both phantom and clinical data sets. The reported solution times were averaged over the successful registration runs for each trial and reported both as mean total time as well as mean time per iteration for each algorithm.

seconds per iteration). In order to remove bias from failed registrations, only the times to solution for the registrations that were determined as successful (based on the aforementioned criteria) were reported. For reference, the robustness trials were performed on a Dell XPS with Pentium D 3.20 GHZ CPU and 2 GB RAM, which is not unlike what would be used during an IGLS procedure.

The results shown in Table III.7 show the increased computation for the weighted patch ICP algorithm using both single and multiple patch regions normalized per iteration, with respect to the ICP results, is modest. The increase in total computation time imposed by the weighted ICP algorithm using a single patch is only significantly greater than the ICP results for the "large scale" perturbation experiments. Additionally, the total time to solution for the weighted patch ICP algorithm using multiple patch regions over all trials was lower than the results provided by ICP. While the computation time per iteration is greater for the weighted patch ICP algorithm, when multiple patch regions are used the number of iterations required to reach a given convergence criterion is lowered, thus facilitating faster solution times when compared with ICP.

A second concern of utilizing the proposed method in the clinical setting is the additional time required to delineate the pertinent anatomical features from either LRS

data or via digitization with a tracked probe. Since the utilization of the proposed method with two salient features (falciform ligament and inferior ridge) alleviates the need for an anatomical fiducial-based initial alignment, we feel that the manual selection of the salient anatomical features in the LRS data will have a negligible influence on the time and work flow for intra-operative data acquisition. In essence, there will be no increase in the OR time requirements for data acquisition while a considerable increase in algorithm robustness will be achieved. Furthermore, utilization of differential geometry similar to the crest line extraction work published by Monga *et al*. may provide an avenue for the automatic delineation of the salient anatomical features, particularly the inferior ridge regions [101].

Conclusion

The results of the proposed weighted patch ICP algorithm suggest that this method is more robust to poor initial alignments than the traditional ICP based approach. As shown in several of the clinical data sets, the proposed weighted ICP method was able to achieve reasonable alignments under conditions where the traditional ICP method failed. Additionally, the use of multiple anatomical features (i.e. falciform ligament and inferior ridge) showed increased robustness in both the clinical and phantom perturbation trials, provided reasonable alignments for all clinical data sets under conditions where no initial pose transformation was provided. As such, the proposed method, using multiple anatomical features, allows the ability to neglect the use of an anatomical fiducial PBR initial registration used in current IGLS methods. Further, the incorporation of the proposed algorithm does not impose any additional computational time and requires a trivial additional effort, in terms of intra-operative data collection and pre-operatively data processing, relative to the current technique.

Acknowledgements

This work was supported under the NIH R21 Grant No. CA 91352-01 and by the NIH R21 Grant No. EB 007694-01 from the National Institute of Biomedical Imaging and Bioengineering of the National Institutes of Health. The authors would like to thank Dr. Sean Glasgow, Mary Ann Laflin, and Krista Cstonos of Washing University School of Medicine in St. Louis, MO for their help in collecting the clinical range scan data used in this work. In addition, many of the algorithms and visualization tools used in this work were developed using the Visualization Toolkit (http://www.vtk.org). The FastRBF Toolkit (FarField Technology, Christchurch, NZ) was used to generate a number of the surfaces shown. The ANN Nearest Neighbor Search Library (http://www.cs.umd.edu/ mount/ANN/) was used to speed up closest point searches. Some segmentations of clinical data were performed using the Analyze AVW Version 6.0, which was provided in collaboration with the Mayo Foundation, Rochester, Minnesota. For disclosure, Drs. Chapman, Dawant, Galloway and Miga are founders and hold equity in Pathfinder Therapeutics, Inc., Nashville, TN.

CHAPTER IV

MANUSCRIPT 2 - ORGAN SURFACE DEFORMATION MEASUREMENT AND ANALYSIS IN OPEN HEPATIC SURGERY: METHOD AND PRELIMINARY RESULTS FROM 12 CLINICAL CASES

Abstract

The incidence of soft tissue deformation has been well documented in neurosurgical procedures and is known to compromise the guidance information provided by current image-guided surgery systems. Within the context of image-guided liver surgery (IGLS), no detailed method to study and analyze the observed organ shape change between pre-operative imaging and the intra-operative presentation has yet been developed. Contrary to the studies of deformation in neurosurgical procedures, the majority of deformation in IGLS is imposed prior to the resection and is due to laparotomy and mobilization. As such, methods of analyzing the organ shape change must be developed to utilize the sparse intra-operative data (e.g. laser range scan (LRS) surfaces) acquired with the organ in its fully deformed shape. To achieve this end we utilize a pair of deformation metrics, mean curvature difference and signed closest point distance, computed based on the rigid alignment of the intra-operative LRS data with organ surfaces generated from the pre-operative tomograms. The rigid alignment between the intra-operative LRS surfaces and pre-operative image data was computed with a feature weighted surface registration algorithm. In order to compare the deformation metrics across patients, an inter-patient non-rigid registration of the pre-operative CT images was performed. Given the ability to determine inter-patient liver registrations, a statistical analysis was performed to determine the potential similarities in the distribution of measured deformation between patients who had undergone similar procedures. In addition to the statistical analysis, a qualitative

comparison of the deformation metric distributions was also performed. The results of the statistical and qualitative analysis suggests a similarity in imposed deformation within similar procedure types.

Introduction

The goal of image-guided surgery is to utilize pre-operatively acquired tomographic images interactively within the surgical setting. In order for this to be possible a mathematical mapping, or registration, of the intra-operative presentation to the pre-operative image volume is required. A significant body of work has been dedicated to exploring methods to provide this registration within the context of open hepatic procedures [30, 38, 72, 73] allowing for the realization of image-guided liver surgery (IGLS) [27]. However, the *de facto* methods of obtaining the image-to-physical space registration for IGLS have required the use of rigid body assumptions. These assumptions are known to be invalid due to the incidence of soft tissue deformation. For example, brain deformations (commonly referred to as "brain shift") have been well documented within the literature and have been shown to compromise the guidance information provided by commercially available neurosurgical image-guidance systems [124, 92, 75, 93]. Unfortunately, the measurement techniques applicable within the neurosurgical context such as the tracking of cortical features do not translate to IGLS readily since a large component of the observed liver deformation does not have a time varying component.

Within this study we will rely on the use of intra-operatively obtained laser range scan (LRS) data of the liver surface acquired after the performance of laparotomy and liver mobilization. Due to the nature of open-hepatic procedures, in contrast to neurosurgical procedures, the majority of deformation occurs before the acquisition of surface data via LRS is possible. Since distinct features are not present within IGLS, new techniques of visualization and analysis to properly understand the nature of the

shape change experienced in open hepatic procedures will be developed and tested in this work.

Related Work

While a number of techniques have been proposed for the compensation of intra-operative deformation, a proper study of this behavior has not been performed within the context of IGLS. As mentioned previously, a number of studies have been performed to measure and analyze the brain shift encountered during neurosurgical procedures. Roberts *et al.* performed a quantitative analysis of cortical displacement in 28 cases by tracking specific features on the brain surface throughout the procedures [124]. Maurer *et al.* performed similar studies where point features on the brain surface were digitized wi anth optical tracking system immediately upon durotomy and after performing functional mapping prior to resection [92, 75]. Additional studies were performed by Maurer *et al.* utilizing an interventional MR scanner to collect images throughout the surgical procedure [93].

The analysis of deformation for hepatic procedures has mainly been focused on the motion due to respiration. Cash *et al.* tracked the motion of a point on the liver surface due to respiration using an optically tracked pen probe during an open liver resection case [27]. A study by Shimizu *et al.* has been performed to analyze the motion of a liver tumor due to respiration via high speed MR imaging to estimate potential errors inherent associated with radiotherapy procedures [137]. Rohlfing *et al.* utilized gated, serial MR images to analyze respiratory motion via deformable registration methods [126].

Objective

The objective of this study is to develop a protocol to determine the extent and nature of intra-operative soft tissue deformation encountered in open liver surgical

procedures. Due to the nature of deformation in open hepatic procedures, intra-operative imaging can only be acquired after a majority of the deformation has occurred. As such, previous methods of tracking features throughout the surgery are not feasible in this case and new methods of determining the organ shape change must be developed. Further, the measured deformation will be analyzed to determine the similarities between the measured deformations between similar resection procedures. The performance of this measurement and analysis will provide valuable insight for the development of methods which will facilitate the intra-operative compensation of soft tissue deformation for IGLS procedures. To the best of our knowledge, this is the first study to report the extent of intra-operative liver deformations due to surgical manipulation.

Methods

Patient Overview

Institutional Review Board (IRB) approval was obtained for the intra-operative acquisition of liver surface data as well as the use of the ORION surgical navigation system [145] at Barnes-Jewish Hospital in St. Louis, MO. A summary of the patient information for 12 of the cases performed between November 2004 and August 2006 for which intra-operative data was acquired is shown in Table IV.1.

Pre-Operative Image Acquisition and Processing

For each of the patients included in this study, CT image volumes were acquired approximately one week prior to performance of the surgical procedure (SOMATOM Sensation 64, Siemens Medical Solutions, Munich, Germany). A triphasic imaging protocol was employed for acquisition of arterial phase, venous phase, and non-contrast liver parenchymal tomographic volumes. The venous phase image sets, which

Case	Age	Sex	Pathology	Surgical Procedure
1	42	F	T2 staged tumor in gallbladder fossa	Exploratory laparotomy including multiple wedge liver and peritoneal biopsies; no resection performed
2	75	M	T2 staged cholangiocarcinoma with positive cystic duct margin	Resection of extrahepatic bile duct and gallbladder bed including segments IV and V
3	67	M	Extensive hilar cholangiocarcinoma	Resection of extrahepatic biliary tree with bile duct tumor
4	81	M	Suspected gallbladder and bile duct cancer	Partial liver resection of IV-B and V with *en bloc* gallbladder resection; resection of extrahepatic bile ducts
5	51	F	Suspected left hilar cholangiocarcinoma	Multiple tumor biopsies with bi-lobar multifocal involvement in segments III, V, and VI; no resection performed
6	65	M	Cholagiocarcinoma involving left bile duct	Left hepatectomy with caudate lobe resection; resection of entire extrahepatic biliary tree
7	54	M	Metastatic chondrosarcoma in left lobe	Hepatic resection including segments II and III
8	49	F	Hilar cholangiocarcinoma in left lobe	Exploratory laparotomy including right lobe wedge biopsy; no resection performed
9	66	M	Metastatic colorectal carcinoma in right lobe	Right hepatectomy for removal of three foci
10	36	M	Hepatocellular carcinoma in left lobe	Left hepatectomy performed midway along segment IV for removal of tumor involving segments II and III with partial extension into segment IV
11	62	M	Metastatic colorectal cancer in right lobe	Exploratory laparotomy with multiple right lobe and intraperitoneal tumor biopsies
12	82	M	Metastatic colorectal cancer in segment VI	Resection of segment VI and wedge excision of segment V tumor

Table IV.1: Summary of patient information including the pathological and surgical details for the cases performed under the IRB protocol approved at Barnes-Jewish Hospital, St. Lous, MO.

capture the hepatic venous and portal venous structures in high contrast, were used for the analysis methods proposed in this study.

In order to facilitate the analysis of the intra-operative shape change, the organ surfaces for each of the cases must be generated from the pre-operative image volumes. A semi-automatic method developed by Dawant *et al.* [47, 115], based on the level set method proposed by Sethian [134], was used to segment the liver from the surrounding anatomical structures in the pre-operative tomograms. Isosurfaces were generated from the liver segmentations via the Marching Cubes Algorithm [84] and smoothed via radial basis functions (FastRBF toolkit, FarField Technology, Christchurch, New Zealand) to facilitate accurate computation of geometric invariants.

Intra-Operative Surface Acquisition and Processing

The intra-operative surface data utilized for this study were acquired using an off the shelf laser range scanner (LRS). The RealScan 200C (3-D Digital Corporation, Bethel, CT) is capable of acquiring spatially dense 3-D point cloud surface representations of 500 lines per scene with as many as 512 samples per line and a spatial resolution on the order of 0.5 mm at the typical range acquired in this study (45-60 cm). In addition to the geometrical data, a digital image is also acquired of the scanners field of view. Via a pre-determined calibration, the color data from the digital image can be texture mapped on the 3-D point cloud. A detailed validation of the imaging capabilities of the LRS system used has been provided by Sinha *et al.* [139] and Cash *et al.* [30] The liver parenchyma was segmented from the raw LRS data and the FastRBF toolkit was utilized to provided a smooth, regularly sampled representation of the intra-operative surface, which facilitated the computation of the geometric invariants for use in the deformation analysis methods. An example LRS data set is shown in Figure IV.1.

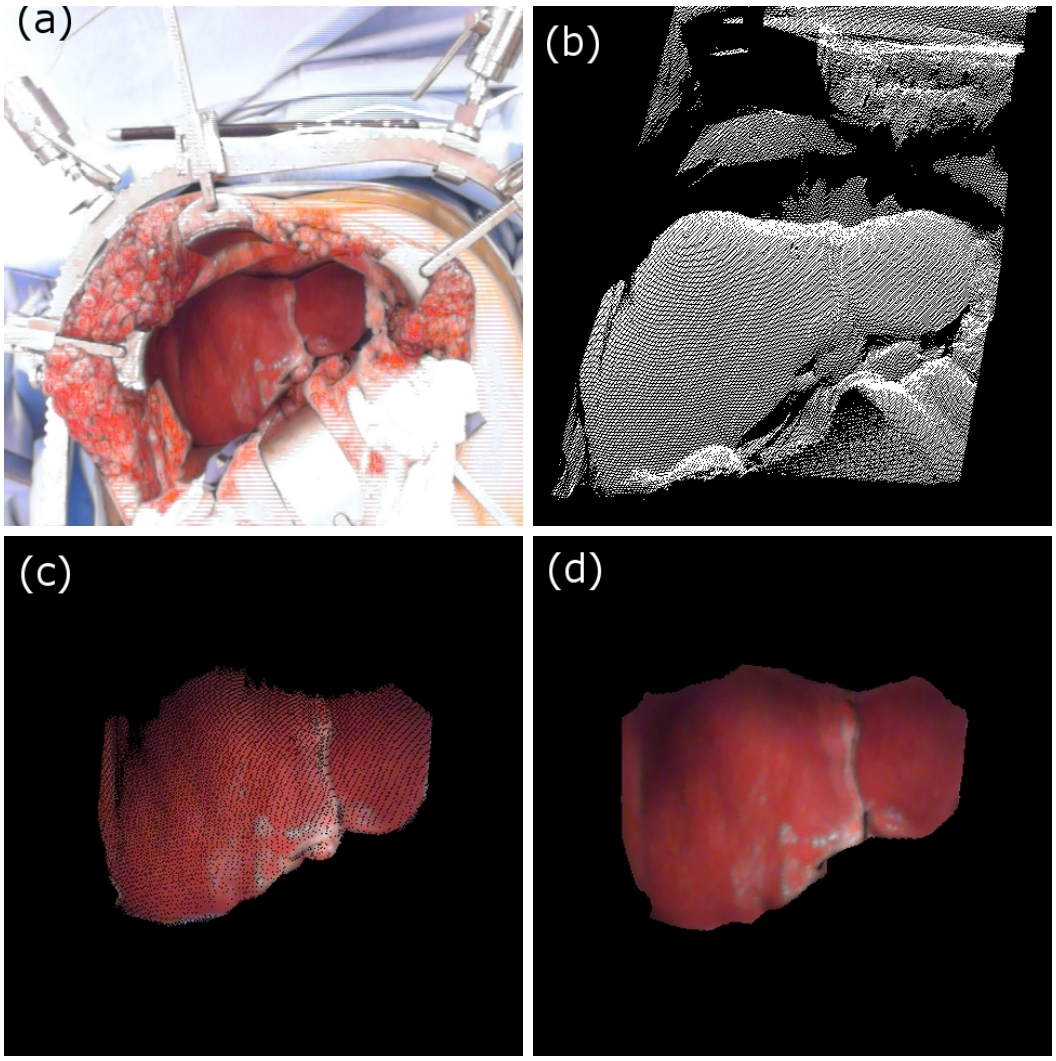

Figure IV.1: The intra-operatively collected LRS data set acquired for Case 9. The texture map of the OR scene is shown in panel (a), the raw LRS point cloud is shown in panel (b), the segmented and texture mapped liver LRS surface data is shown panel (c), and panel (d) shows the RBF interpolation of the texture mapped liver surface shown in (c). The RBF interpolation is used to facilitate accurate computation of surface curvature utilized in the deformation measurement.

In accordance with the IRB protocol, the LRS data was acquired during pre-planned apneic periods to minimize errors due to respiratory liver motion. The data was acquired at end expiration during the respiratory cycle and the time within the surgical procedure where the surface data was acquired is summarized in Table IV.2. In addition to the timing of data acquisition, the coverage of the scan data is also summarized.

Case	Group	Scan Time	Scan Coverage
1	O	post-laparotomy†	III-V,VIII
2	O	post-laparotomy†	II-V,VIII
3	N/A	pre-cholecystectomy	II-V,VIII
4	N/A	pre-cholecystectomy	III,IV
5	B	pre-cholecystectomy	II-V,VIII
6	A	post-cholecystectomy	II-V,VIII
7	A	post-laparotomy†	II-V,VIII
8	B	post-cholecystectomy	II-V,VIII
9	C	pre-cholecystectomy	III-V,VIII
10	A	pre-cholecystectomy	III-V,VIII
11	C	post-cholecystectomy	III-V,VIII
12	C	post-cholecystectomy	III-V,VIII

Table IV.2: Summary of patient intra-operative LRS acquisition including the time of the scan and the scan coverage. All of the scans were acquired prior to the performance of liver resection. Note that the data for patient 3 and patient 4 were not included in the deformation analysis studies due to the limited field of view obtained in the intra-operative LRS data. †Patients with previously performed cholecystectomy.

To facilitate the inter-patient deformation measurements within similar procedures, the patients were separated into three groups as noted in Table IV.2. The three patients for which left hepatectomy procedures were performed were placed in Group A. The two patients that presented with left hilar cholangiocarcinoma including bi-lobular, multi-focal involvement were comprised Group B. The three patients for which right lobe biopsies and resections were performed comprised Group C. Finally, the patients placed in Group O did not fit in the aforementioned groups and were themselves different procedures. It should be noted that the data for patient 3

and patient 4 were excluded from the deformation analysis due to the lack of sufficient coverage of the acquired intra-operative LRS surface digitization.

Inter-Patient Deformable Registration

In order to effectively compare the measured intra-operative surface deformation across the 12 patients, it is necessary to compute an inter-patient transformation between the pre-operative CT image volumes. As the shape and volume of hepatic anatomy is highly variable between patients, a non-rigid image registration method is required. The adaptive basis algorithm (ABA) developed by Rodhe *et al*. was selected to provide the required non-rigid transform for the intra-patient liver registration required for this work [125]. This algorithm has been utilized to perform inter-patient brain registrations to create atlases for the placement of electrodes in deep brain stimulation procedures as well as to provide registrations between whole body images of mice for utilization in a variety of temporal and longitudinal studies [83, 49, 50].

Similar to the registration method proposed by Rueckert *et al*. [127], ABA employs a multi-scale, multi-resolution approach whereby the deformation field is modeled as the linear combination of a set of basis functions irregularly spaced over the image domain:

$$\mathbf{v}(\mathbf{x}) = \sum_{i=1}^{N} \mathbf{c}_i \mathbf{\Phi}(\mathbf{x} - \mathbf{x}_i) \tag{IV.1}$$

where $\mathbf{x}$ is the coordinate vector in $\Re^d$ with d being the dimensionality of the image sets, $\mathbf{\Phi}$ is a Wu radial basis function with compact support [161], and $\mathbf{c}_i$ represents the coefficient weighting for each of these basis functions. The values of the coefficients are optimized such that the mutual information (MI) calculated between the deformed source and target images is maximized . For ABA, a steepest

gradient descent optimization algorithm is used to solve for the optimal basis function coefficients.

To provide the initial alignment required for ABA, a surface based registration was performed between the patient volumes via a rigid implementation of the iterative closest point (ICP) algorithm [12]. The surfaces were extracted from the segmented image volumes via the aforementioned segmentation and surface tessellation methods. Once transformed by the rigid transformation, the segmented source image volumes were then non-rigidly registered to the target volume via ABA. The ABA registration was implemented in a multi-level fashion with multi-resolution and multi-scale components similar to that described by Li *et al.* [83] Three image resolution levels were used for the inter-patient liver registrations (77×77×64, 154×154×128, and 308×308×255) and the scale of basis functions used varied from a 3×3×3 matrix for the lowest resolution to a 50×45×46 matrix at the highest image resolution for a total of 15 levels. The parameters with regards to the multilevel approach were determined empirically.

For the purposes of this study, the segmented images were used to compute the inter-patient liver registration due to anatomical differences with respect to gallbladder anatomy. The fact that some of the patients had prior cholecystectomies while others presented with extremely distended gallbladders could confound the non-rigid registration algorithm and result in incorrect deformation fields in the neighborhood of the gallbladder fossa. The ABA registrations were performed such that all of the pre-operative image volumes could be mapped to a single target space (i.e. patient 8 for this study) which facilitated the inter-patient statistical comparison of the distribution of measured deformation.

Rigid Surface Registration of Intra-Operative Data

Quantification of the surface deformation measured via the intra-operative LRS data relies on the ability to register this data with the liver surface generated from segmentation of the pre-operative tomograms. To provide this registration we utilize the rigid surface salient feature registration algorithm developed in Chapter III. The developed algorithm utilizes salient anatomical features that are easily identifiable in the pre-operative tomogram and intra-operative LRS presentation [38] and was inspired by the weighted geometrical features algorithm proposed by Maurer *et al.* [90]. The salient features utilized for the performance of the rigid surface regions in this study were the falciform ligament and inferior ridge along segments IV, V, and VI. An example data set highlighting the feature segmentations and the resulting salient feature preregistration is shown in Figure IV.2.

As mentioned previously, the lack of surface coverage provided by the LRS data for patients 3 and 4 allowed the use of only a single patch region for the rigid surface registrations performed for these cases. In these registrations, only the falciform ligament or inferior ridge along segments IV, V, and VI was used.

Tissue Deformation Metrics and Analysis

The rigid surface alignment of the intra-operative LRS and pre-operative CT liver surfaces was processed further by computing a signed distance metric. The performance of point searches was used to facilitate the determination of both the region of liver covered by the LRS data and the Euclidean distance calculations. The directional sign for the distance value was determined by comparing the closest point distance vector with the surface normal. The closest point values were computed from target (i.e. CT liver surface) to source (i.e. LRS scan).

In addition to the use of a closest point distance metric, the mean curvature (H) was also chosen as a geometric invariant for use in the quantification of observed soft

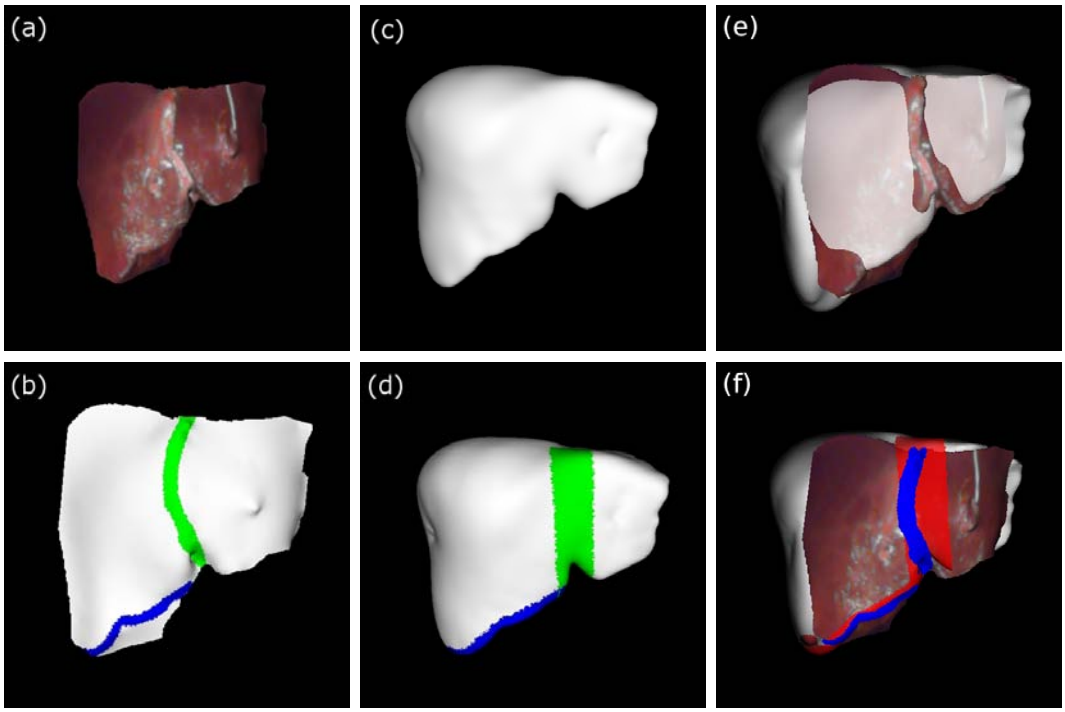

Figure IV.2: The LRS surface data (a-b), CT surface data (c-d) and resulting weighted patch ICP registration (e-f) for Case 8. The segmentations of the patch regions are shown for the LRS and CT surfaces in panels (b) and (d), respectively. The falciform region is highlighted in green while the inferior ridge of segments IV, V and VI is shown in blue.

tissue deformation. In order to approximate H at each point in the interpolated LRS and CT surfaces, a quadric was fit to the local area around the point [146]. The local quadric surface is parametrically represented as follows:

$$S(x, y, z) \Rightarrow S(u, v) = (u, v, au^2 + 2buv + cv^2) \tag{IV.2}$$

In a neighborhood of n surface points, the quadric patch can be expressed in matrix form $Ax = b$:

$$\begin{bmatrix} u_1^2 & 2u_1v_1 & v_1^2 \\ u_2^2 & 2u_2v_2 & v_2^2 \\ \vdots & \vdots & \vdots \\ u_n^2 & 2u_nv_n & v_n^2 \end{bmatrix} \begin{bmatrix} a \\ b \\ c \end{bmatrix} = \begin{bmatrix} h_1 \\ h_2 \\ \vdots \\ h_n \end{bmatrix} \tag{IV.3}$$

The local quadric surface fit begins by using the surface normal **n** (provided by the surface tessellation) at the inspection point and then drawing two orthogonal vectors **u** and **v** on the tangent plane to serve as the u and v axes. The surrounding points to be used in the quadric fit are projected into the (u,v) plane along the surface normal **n** and the distance between the point in the (u,v) plane and the neighbor point is also determined ($h(u, v)$). In this way, the surrounding points can be transformed into the local (u,v,$h(u, v)$) coordinate system whereby a least squares quadric fit can be performed via Equation (IV.3). The resulting parameters from the quadric fit can then be used to compute H as follows:

$$H = a + c \tag{IV.4}$$

Once the curvatures were calculated at each point on both the pre-operative CT and intra-operative LRS surfaces, differences between the values were computed. Point correspondence for the difference calculation was determined via the closest

point operator as with the signed distance measurements. For reference, a neighborhood of four points was used for the quadric fit.

Given the inter-patient registration computed with the ABA algorithm, it is possible to compare the distribution of curvature difference and signed closest point distance measurements across patients to determine the correlation between the intra-operative surface deformation and surgical procedure. In order to compare the data across all patients, the regions of the liver surface for which LRS data existed over all cases had to first be computed. Note that we excluded two of the data sets (Case 3 and Case 4) from the computation of the overlap region due to insufficient LRS surface coverage. The computed overlap region for the 10 included data sets mapped on the target liver surface is shown in Figure IV.3.

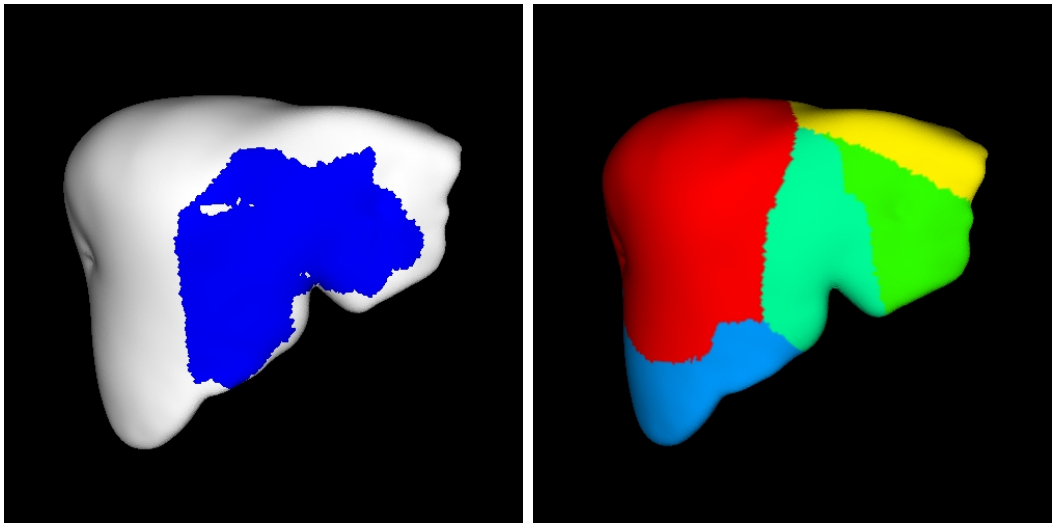

Figure IV.3: Display of the overlap region (left panel) calculated via the inter-patient registration on the target image surface. The overlap region contained 5065 points and contained measurements within segments II, III, IV, V, and VI. The right panel shows the Couinaud segment delineation for the patient provided by MeVis Medical Solutions (Bremen, Germany).

The correlation coefficient (CC) image similarity metric was chosen to compare the distribution of curvature difference and signed closest point distance measurements

across patients. The CC metric is not biased by absolute differences in the underlying data and simply assumes a linear relationship. The CC value is determined via the following equation:

$$CC = \frac{\sum_i (T(i) - \overline{T})(S'(i) - \overline{S}')}{\left[\sum_i (T(i) - \overline{T})^2 \sum_i (S'(i) - \overline{S}')^2\right]^{1/2}} \qquad \forall \quad i \in T \cap S' \tag{IV.5}$$

where S' is the transformed source data set, T is the target data set, and i represents the collection of overlapping surface points between the data sets. The mean deformation metric values in the transformed source and target data sets calculated for the overlap region are represented by $\overline{S}'$ and $\overline{T}$, respectively.

The CC values were computed between each of the patient data sets over both deformation metrics (shown in Tables IV.5 and IV.6). The CC values were then averaged within the groups of patients for which similar procedures were performed ("in group"). For statistical comparison, CC average values were computed for the groups patients for which the procedures were different ("out group"). For the procedure groups with more than two patient data sets (Group A and Group C), an independent two-sample t-test for unequal sample sizes and assumed unequal variances was performed between the "in group" and "out group" CC mean values (SigmaPlot, Systat Software, Inc., Chicago, IL).

Results

Inter-Patient Deformable Registration

The results of the inter-patient deformable registrations provided by ABA are summarized in Table IV.3. A qualitative visualization of registration result for a single case in terms of surface renderings is shown in Figure IV.4. Overall, the closest point distance measurement of error suggests that the registration results are of sufficient accuracy to be viable for use in the statistical comparison of deformation across

patients. The largest errors reported in Table IV.3 were for the registration performed for Case 9 which was due to the presence of an atypical anatomical extension of liver parenchyma visible at the left lateral segment which was not present in the target liver (i.e. Case 8) or any other data set. Further, it should be noted that the closest point distance measure of errors was much smaller when averaged over the region of LRS data overlap as compared with the average computed over the entire surface. This seems to indicate that the registration errors are minimal in the region where the statistical analysis of the deformation was to be performed.

	TARGET Case 8					
SOURCE	SRC→TAR		TAR→SRC		Overlap	
Case	Mean±St.d.	Max	Mean±St.d.	Max	Mean±St.d.	Max
1	0.94±0.48	6.05	1.11±0.80	15.55	0.94±0.37	2.78
2	1.20±0.59	5.01	1.26±0.88	14.21	1.08±0.46	2.59
3	0.85±0.58	15.99	0.81±0.60	13.76	N/A	N/A
4	1.12±1.11	22.73	0.98±0.46	5.12	N/A	N/A
5	1.80±1.10	15.41	1.73±1.03	11.96	1.04±0.55	3.29
6	1.11±0.83	17.27	1.13±0.65	13.23	0.98±0.42	3.15
7	0.95±0.49	6.90	0.93±0.65	12.88	0.83±0.34	1.99
9	2.22±5.54	57.06	1.30±0.63	5.32	0.88±0.36	2.53
10	0.94±0.93	24.39	0.94±0.41	6.78	0.76±0.29	2.12
11	0.83±0.35	4.99	0.83±0.77	16.48	0.70±0.28	2.35
12	0.86±0.37	4.81	0.83±0.52	11.65	0.71±0.29	1.91

Table IV.3: Summary of inter-patient deformable registration validation in terms of closest point distance values. These values were calculated both from the transformed source (SRC) surface to the target (TAR) surface and from the TAR to SRC surface. Additionally, the closest point distance values were reported as averages over the entire surface and over the region of overlap for which LRS data existed across all patients (shown in last two columns). Note that the maximum closest point distance values were significantly lower in the overlap region as compared with the entire surface.

The qualitative registration results shown in Figure IV.4 echo the numerical summary in Table IV.3. While the ABA result does not provide definite point to point

correspondence, the accuracy of the registration, particularly in the region of the anterior surface of segments III, IV, V, and VIII, indicate that it is sufficient for the inter-patient statistical comparison. It should be noted that the maximum closest point distance error, computed from deformed source surface to the target surface, for this particular registration was approximately 5 mm. The region of largest misalignment was located on the posterior surface and not in the overlapping region used for the inter-patient deformation comparison.

Rigid Surface Registration and Deformation Quantification

The results of the weighted patch ICP rigid surface registrations between the pre-operative CT data and intra-operative LRS liver surfaces for the cases included in Groups A, B, and C are shown in Figures IV.5, IV.6, and IV.7, respectively. Additionally, the computed signed distance and mean curvature differences using the rigid surface registration are texture mapped on the pre-operative image surfaces for qualitative evaluation of the observed deformations over the particular groups of cases. A summary of the signed closest point distances for all clinical cases is shown in Table IV.4 to indicate the range of intra-operative surface shift experienced in open hepatic procedures.

Overall, the visualizations of the distribution of signed closest point distance indicate a general similarity within the patient groups. While the absolute magnitudes of the distances are different with each group there seems to be a general similarity in the nature of the deformation. The qualitative results for the mean curvature difference calculation do not seem to show any discernable pattern within the patient groups.

As with the other qualitative visualizations, the signed distance distributions for the left hepatectomy cases (Group A) shown in the middle column of Figure IV.5 seem to display a similar pattern in the distribution of deformation. The pattern

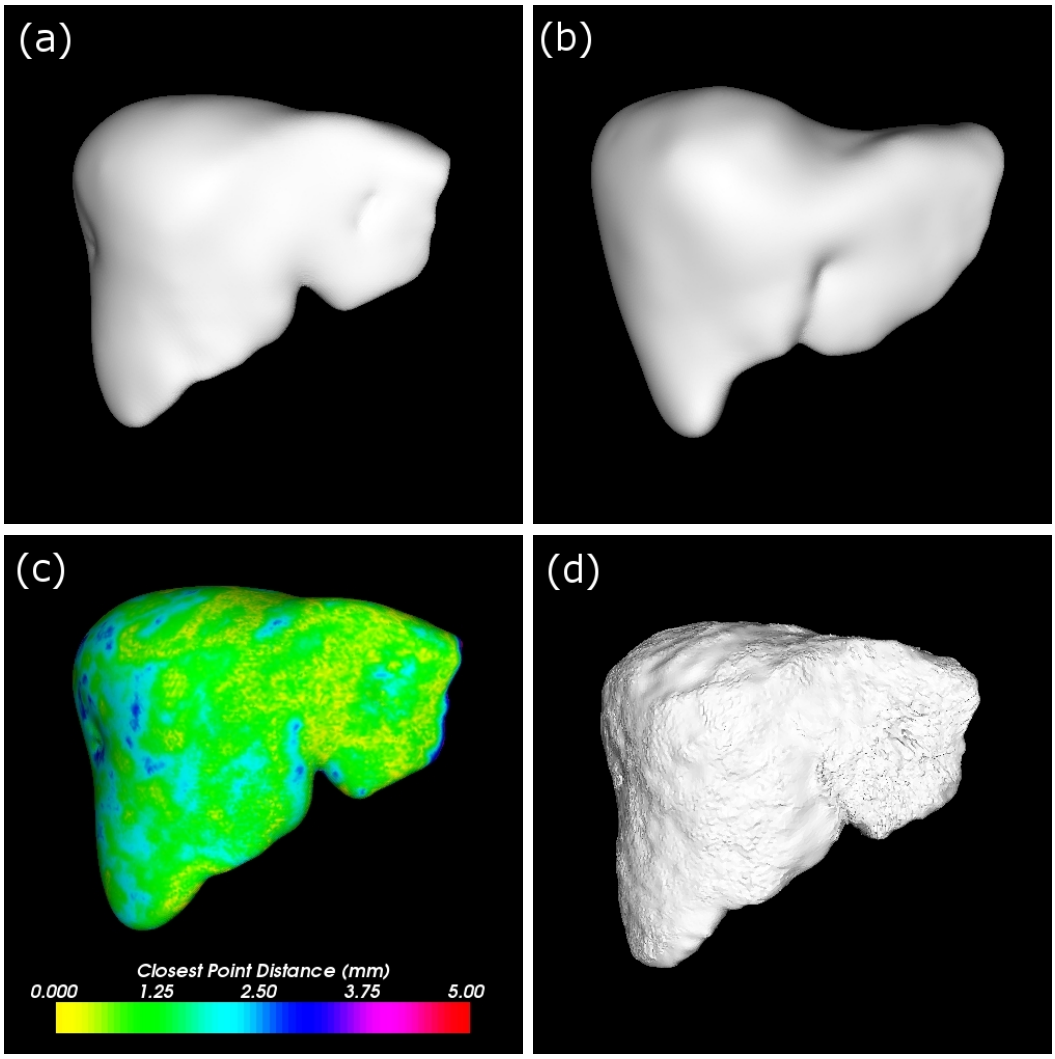

Figure IV.4: Example result of the inter-patient deformable registration between Case 2 (source) and Case 8 (target). The the target and source surfaces for Case 8 and Case 2 are shown in panels (a) and (b), respectively. The transformed source surface is shown in panel (d) and the closest point distances between the target and transformed source surfaces textured mapped on the target surface is shown in panel (c). A numerical summary of the visualized deformable registration result in terms of closest point surface distances can be found in Table IV.3.

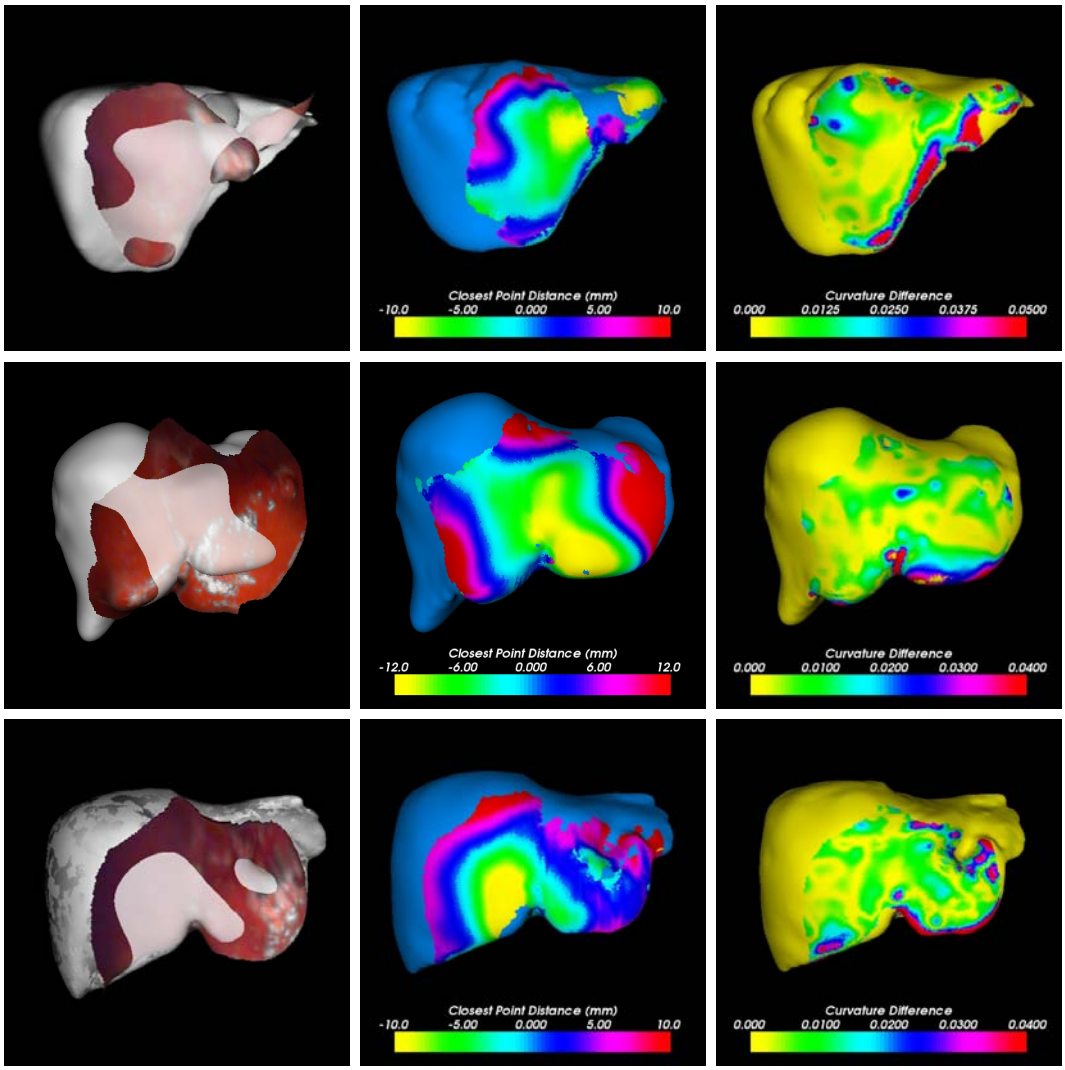

Figure IV.5: Visualizations of the results of the rigid surface registration (left column) for the three group A cases (i.e. left hepatectomies). The signed distance (middle column) and curvature difference (right column) values texture mapped on the pre-operative surfaces are also shown. For reference, the visualizations for case 6, case 7, and case 10 are shown in the top, middle and bottom rows, respectively.

Patient	Mean±St.d.	Median	Range
1	-1.30±4.20	-2.01	18.15,-9.36
2	0.74±3.39	0.79	12.10,-7.60
3	-0.82±4.91	-1.85	19.73,-19.75
4	-0.60±4.32	-0.74	8.39,-10.90
5	-2.61±4.71	-2.74	12.79,-18.80
6	-1.17±4.54	-1.44	14.12,-13.92
7	1.61±8.41	0.77	22.89,-16.40
8	-3.87±4.27	-3.32	9.33,-15.21
9	-1.28±6.20	-1.31	18.86,-13.61
10	1.35±5.34	2.01	19.45,-15.61
11	0.06±5.5	-0.71	18.62,-12.52
12	0.67±4.73	-0.42	19.55,-7.62

Table IV.4: Summary of the signed closest point distance information over all 12 clinical cases. The values of mean, standard deviation, median, and range of distance measurements are reported in mm units. Note that the range of surface error indicates surface displacements on the order of 1 to 2 cm.

of the deformation across the Group A patients where the central scan region is the location of a majority of the negative closest point distances and the peripheral scan regions lie above the pre-operative surface indicate an overall flattening of the surface in the intra-operative presentation. It should be noted that the overall shape change indicted by the signed closest point distance distribution for Group A is very similar to that for the Group C cases shown in Figure IV.7. However, the region where a majority of the flatting of the organ is evident seems to be shifted closer to the left lobe for the Group A cases and towards the right lobe of the liver for the Group C cases.

While the general pattern of shape change with regards to the signed closest point distance distribution for the left hilar cholangiocarcinoma patients (Group B) is markedly different than the qualitative results shown for Group A and Group B, the in group similarity in the distribution of this metric is evident. The peripheral scan regions for the Group B cases yield negative closest point distances since the

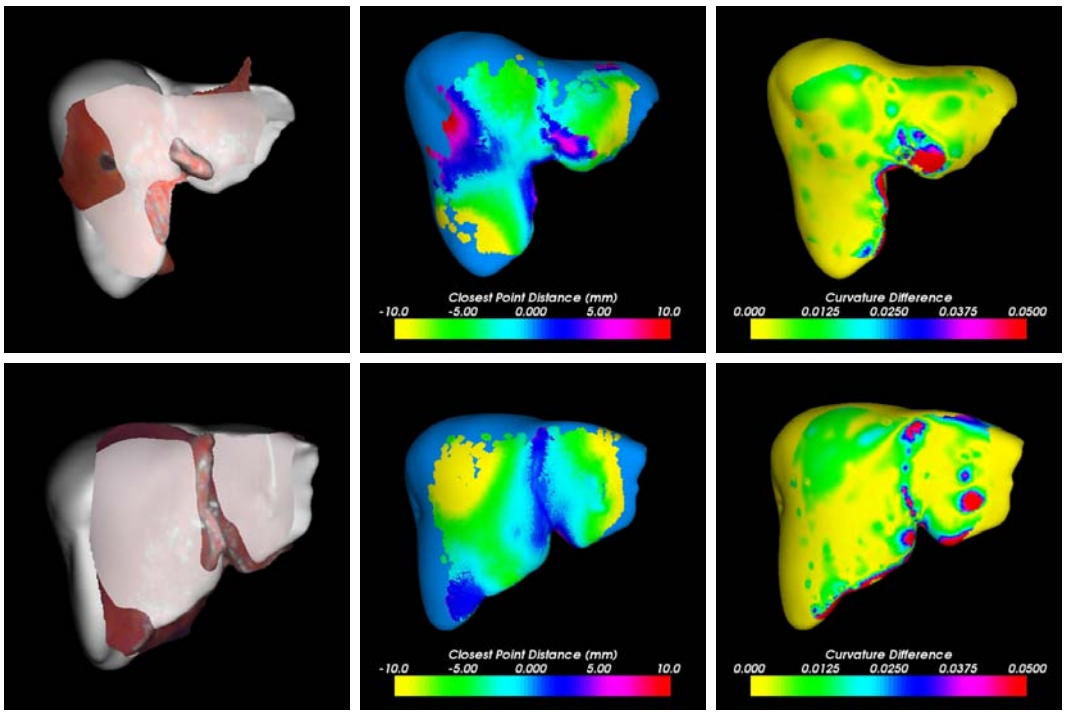

Figure IV.6: Visualizations of the results of the rigid surface registration (left column) for the two group B cases (i.e. left hilar cholangiocarcinoma with bi-lobular, multi-focal involvement). The signed distance (middle column) and curvature difference (right column) values texture mapped on the pre-operative surfaces are also shown. For reference, the visualizations for case 5 and case 8 are shown in the top and bottom rows, respectively.

intra-operative LRS data lies below the pre-operative surface. This seems to indicate a substantially different change in the overall organ shape for the Group B patients as compared with the other groups. Generally speaking, the intra-operative surface seems to be generally more curved and less flat than the pre-operative organ shape. However, the distribution of mean curvature differences for this patient group, as with the others, does not show any significant qualitative similarity.

As mentioned, the general distribution of the signed closest point measure of deformation for the Group C cases indicates a qualitative similarity in the organ shape change for the right lobe biopsy and resection procedures. While the magnitude of the measured distances varies within the patient group, signed distance distribution indicates a generally flattening of the organ as in the Group A cases. The difference in between the observed organ shape change in Group C, as compared with the Group A cases, is the the shift to the right of the region of negative closest point distances. The difference in the location of the flattening shape change is due, presumably, to the differences in the mobilization methods used for these procedures. As with the other groups, the distribution of mean curvature differences does not seem to indicate a recognizable pattern within the patient group.

Summary of the Deformation Analysis

The CC values computed between all the cases over the computed overlap region (shown in Figure IV.3) for the signed distance and curvature difference deformation measurements are shown in Table IV.6 and Table IV.5, respectively. In order to determine the similarity in measured deformation between similar surgical procedures, the mean CC values were then computed within the three groups of clinical cases (i.e. "in group" mean). Where possible, a statistical comparison was then performed with the mean value of the out of group CC values. The mean CC values computed for

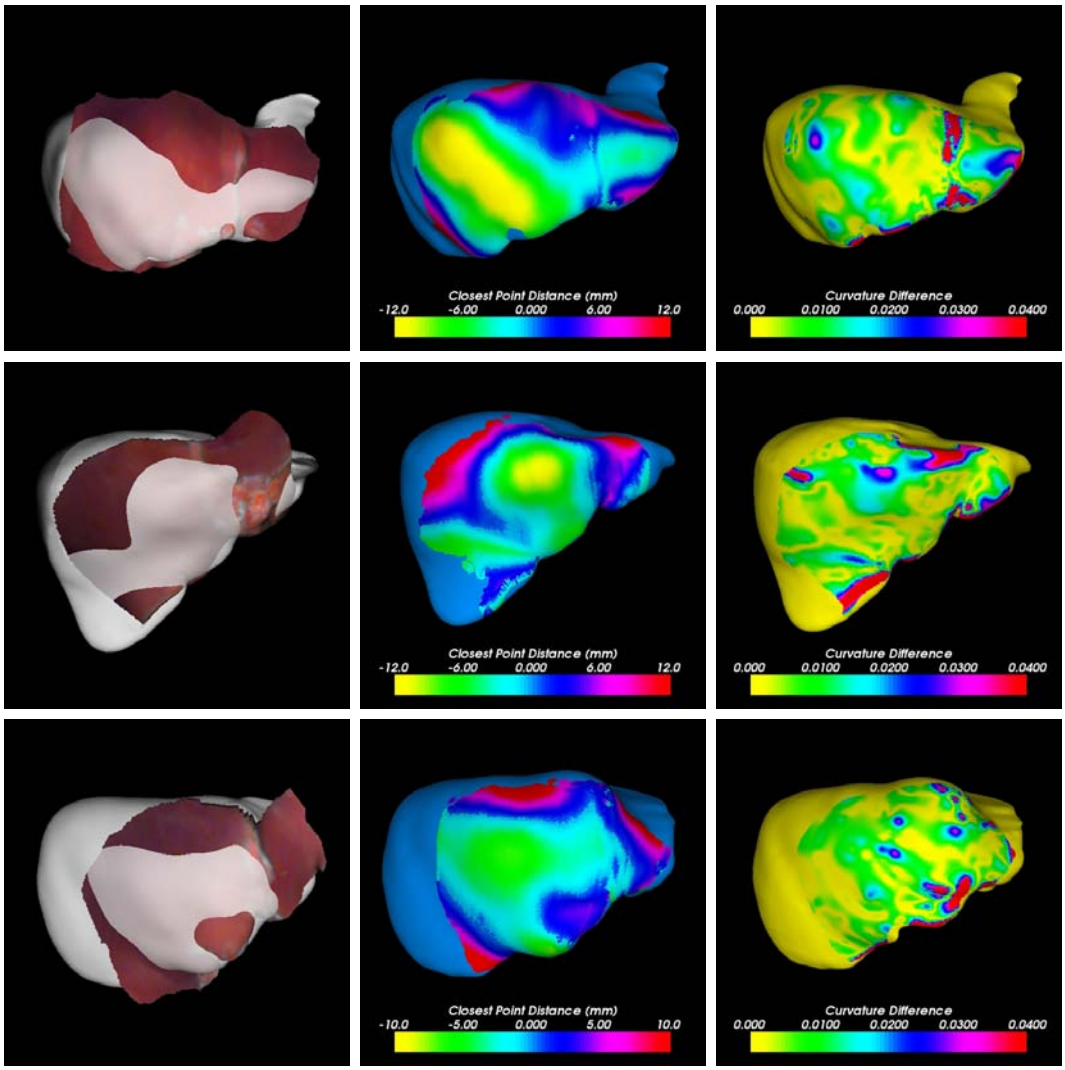

Figure IV.7: Visualizations of the results of the rigid surface registration (left column) for the three group C cases (i.e. right lobe biopsies and resections). The signed distance (middle column) and curvature difference (right column) values texture mapped on the pre-operative surfaces are also shown. For reference, the visualizations for case 9, case 11, and case 12 are shown in the top, middle and bottom rows, respectively.

both signed distance and curvature difference, as well as the results of the statistical comparisons, are shown in Table IV.7.

Case	1	2	5	6	7	8	9	10	11	12
1	1.0	-0.63	-0.09	-0.42	-0.27	-0.02	0.77	0.42	0.22	0.22
2	xx	1.0	0.22	0.27	0.49	-0.16	-0.78	-0.39	-0.44	-0.17
5	xx	xx	1.0	-0.35	-0.36	0.35	-0.24	-0.31	-0.06	-0.28
6	xx	xx	xx	1.0	0.50	-0.15	-0.43	0.02	0.17	0.28
7	xx	xx	xx	xx	1.0	-0.38	-0.45	0.18	-0.21	0.19
8	xx	xx	xx	xx	xx	1.0	0.21	-0.39	0.60	0.08
9	xx	xx	xx	xx	xx	xx	1.0	0.27	0.49	0.33
10	xx	xx	xx	xx	xx	xx	xx	1.0	0.17	-0.12
11	xx	xx	xx	xx	xx	xx	xx	xx	1.0	0.39
12	xx	xx	xx	xx	xx	xx	xx	xx	xx	1.0

Table IV.5: Summary of the CC calculations for the signed closest point distance measurements of surface deformation made on the points contained within the overlap region shown in Figure IV.3. The data for cases 3 and 4 have been omitted since the LRS data acquired intra-operatively did not contain sufficient surface coverage.

Case	1	2	5	6	7	8	9	10	11	12
1	1.0	-0.03	-0.08	-0.18	-0.06	-0.11	0.18	0.17	-0.14	0.00
2	xx	1.0	0.00	0.03	0.26	0.12	-0.01	-0.01	-0.08	0.27
5	xx	xx	1.0	0.36	0.43	0.07	0.14	0.04	0.13	-0.01
6	xx	xx	xx	1.0	0.40	0.33	0.24	0.26	0.14	0.07
7	xx	xx	xx	xx	1.0	0.17	0.09	0.15	0.22	0.13
8	xx	xx	xx	xx	xx	1.0	0.18	0.06	0.26	0.06
9	xx	xx	xx	xx	xx	xx	1.0	0.13	0.10	0.00
10	xx	xx	xx	xx	xx	xx	xx	1.0	0.07	0.02
11	xx	xx	xx	xx	xx	xx	xx	xx	1.0	0.02
12	xx	xx	xx	xx	xx	xx	xx	xx	xx	1.0

Table IV.6: Summary of the CC calculations for the curvature difference measurements of surface deformation made on the points contained within the overlap region shown in Figure IV.3. The data for cases 3 and 4 have been omitted since the LRS data acquired intra-operatively did not contain sufficient surface coverage.

Similar to the qualitative visualizations, analysis of mean CC values computed for the signed distance deformation measurement shows markedly larger evidence of a correlation in the imposed organ shape change within similar procedures than those reported for the curvature difference measure. While the results of the statistical

	Signed Distance			Curvature Difference		
Group	In-Group	Out-Group	P Value	In-Group	Out-Group	P Value
A	0.23±0.24	-0.09±0.32	0.11	0.27±0.13	0.13±0.14	0.12
B	0.35	-0.11±0.27	N/A	0.07	0.13±0.16	N/A
C	0.40±0.08	0.00±0.37	0.08	0.04±0.05	0.10±0.11	0.37

Table IV.7: Statistical analysis of the CC calculations for the signed distance and curvature difference measurements made for the overlapped surface region. For each group, "in-group" and "out-group" mean CC values are shown. Where applicable, the p values for t-tests performed are also shown.

analysis of the CC data is not significant to a 95% confidence interval, the small number of patient cases impedes the ability to make strong statistical conclusions with regards to the analysis. However, the absolute magnitude of the difference between the "in group" and "out group" CC means for the signed distance measure implies a similarity in the imposed deformation among similar procedure types.

Discussion

The qualitative visualizations and quantitative measurements of intra-operative surface deformation experienced in open hepatic procedures suggest a correlation between surgical procedure and the imposed organ shape change. In particular, the proposed analysis shows a larger correlation in the distribution of the signed closest point distance measure of intra-operative deformation within groups of similar procedures than does that performed for the curvature measure of deformation. This suggests that the mean curvature difference measure may not be an appropriate deformation metric for IGLS due to the small magnitude of the computed curvature values or that the proposed technique to compare the measured intra-operative deformation may not be amenable to the curvature difference metric.

The fact that similar deformation patterns are reflected among similar resection procedures provides a very powerful insight into potential solutions for the compensation for soft tissue deformation in IGLS. The proposed methods to compensate for soft

tissue deformation in IGLS have primarily been to use the forward solution of FEM liver models using a driving force computed via sparse intra-operative data [94, 28]. A number of other groups have focused on deformable registration techniques using B-spline interpolation to warp to the pre-operative images to the intra-operative ultrasound acquisitions [104, 19, 82]. A common theme with these proposed methods is the incurred time expense due to the computational complexity and user interaction required to execute the algorithms during the surgical procedure. Given the similarity in deformation measured between similar surgical procedures in open hepatic surgery, it may be reasonable to utilize an atlas shape based approach wherein an array of FEM solutions are computed pre-operatively given the *a priori* information regarding the surgical procedure to minimize the intra-operative time associated with deformation compensation. A promising atlas-based technique has been proposed for model updating in image-guided neurosurgery [53] and a preliminary study has been conducted to make these methods amenable to IGLS deformation compensation [39].

While the qualitative and statistical results outlined herein seem to suggest a correlation between the imposed deformation and the surgical procedure, it is important to note that all of the data acquired was for surgeries performed by a single surgeon (W. Chapman). It seems reasonable that the deformations imposed on the organ per procedure may vary based on the tendencies of the particular surgeon performing the procedure. A clinical trial by Pathfinder Therapeutics, Inc. (Nashville, TN) where LRS and other intra-operative digitizations are being acquired across three individual clinical sites (University of Pittsburg Medical Center, Memorial Sloan-Kettering Cancer Center, and Shands at University of Florida Cancer Hospital) is ongoing and will provide valuable data to supplement the findings reported here.

Conclusions

We have developed a protocol suitable to determining the extent of intra-operative surface deformation as well as establishing statistical similarity between patterns of surface deformation and the surgical procedure performed. While the statistical relevance of the computed results is limited due to the small number of patient data, a correlation between surgical procedure and the distribution of signed closest point distance measure of deformation seems quite likely. The results with respect to curvature differences seem to be less significant with regards to statistical results but qualitative observation suggests new methods of analysis may be required. Finally, the impact of the individual surgeon with respect to surgical presentation of the organ and the subsequent variations in deformation imparted needs to be studied further; but nevertheless, it is encouraging that the deformations imparted by the individual surgeon in this study seemed to express a trend across procedures of similar types.

Acknowledgements

This work was supported by the NIH R21 Grant No. EB 007694-01 from the National Institute of Biomedical Imaging and Bioengineering of the National Institutes of Health. The authors would like to thank Dr. Sean Glasgow, Mary Ann Laflin, and Krista Cstonos of Washing University School of Medicine in St. Louis, MO for their help in collecting the clinical range scan data used in this work. In addition, many of the algorithms and visualization tools used in this work were developed using the Visualization Toolkit (http://www.vtk.org). The FastRBF Toolkit (FarField Technology, Christchurch, NZ) was used to generate a number of the surfaces shown. The ANN Nearest Neighbor Search Library (http://www.cs.umd.edu/ mount/ANN/) was used to speed up closest point searches. Some segmentations of clinical data were performed using the Analyze AVE Version 6.0, which was provided in collaboration with the Mayo Foundation, Rochester, Minnesota. For disclosure, Drs. Chapman,

Dawant, Galloway and Miga are founders and hold equity in Pathfinder Therapeutics, Inc., Nashville, TN.

CHAPTER V

MANUSCRIPT 3 - ATLAS-BASED DEFORMATION COMPENSATION USING SALIENT ANATOMICAL FEATURE WEIGHTING FOR IMAGE-GUIDED LIVER SURGERY: PRELIMINARY INVESTIGATION

Abstract

Similar to the well documented brain shift experienced during neurosurgical procedures, intra-operative soft tissue deformation in open hepatic resections is the primary source of error in current image-guided liver surgery (IGLS) systems. The use of biomechanical models has shown promise in providing the link between the deformed, intra-operative patient anatomy and the pre-operative image data. More specifically, the current protocol for deformation compensation in IGLS involves the determination of displacements via registration of intra-operatively acquired sparse data and subsequent use of the displacements to drive solution of a linear elastic model via the finite element method (FEM). However, direct solution of the model during the surgical procedure has several logistical limitations including computational time and the ability to accurately prescribe boundary conditions and material properties. Recently, approaches utilizing an atlas of pre-operatively computed model solutions based on *a priori* information concerning the surgical loading conditions have been proposed as a more realistic avenue for intra-operative deformation compensation. Similar to previous work, we propose the use of a simple linear inverse model to match the intra-operatively acquired data to the pre-operatively computed atlas. Additionally, an iterative approach is implemented whereby point correspondence is updated during the matching process, being that the correspondence between intra-operative data and the pre-operatively computed atlas is not explicitly known in liver applications. Further, salient anatomical feature weighting and point correspondence biasing are

utilized within the algorithm. Preliminary validation experiments of the proposed algorithm were performed using both simulation and phantom data. The proposed method provided comparable results in the phantom experiments with those obtained using the traditional incremental FEM approach and yielded more accurate and robust results when salient feature information was utilized.

Introduction

Intra-operative soft tissue deformation in open hepatic resections is known to be the primary source of error in current image-guided liver surgery (IGLS) systems due to the rigid body assumptions required for image-to-physical space registration. Numerous avenues have been proposed to aid in compensation for the experienced soft tissue deformation, including the use of intra-operative tomography and ultrasound. However, intra-operative computed tomography (iCT) and magnetic resonance (iMR) imaging equipment is extremely expensive and cumbersome in the operating room environment. Additionally, intra-operative ultrasound (iUS) provides low signal-to-noise, sparse images of the patient's anatomy. Ultimately, the goal for image-guidance is to update the high contrast, high resolution pre-operative tomograms to match the intra-operative presentation.

Mathematical models, which have been used to model the various mediators of deformation in neurosurgery, have been proposed to provide the link between the pre-operative and intra-operative presentations. While direct solution of mathematical models, utilizing intra-operatively acquired displacements, during surgery seems to be of promise in facilitating deformation compensation, more recent work in atlas-based methods seems to provide a more realistic alternative. By simulating the range of deformation sources in a pre-operatively computed set of model solutions, or atlas,

and matching the intra-operative data to the atlas, compensation for soft tissue deformation can be performed with minimal user interaction and in a fraction of the time needed to directly solve the model.

While useful guidance information is provided by the rigid, surface-based registrations used in current IGLS procedures, it is quite clear that this information can be compromised by intra-operative soft tissue deformation. The significance of soft tissue deformation in the form of "brain shift" has been widely documented in neurosurgical procedures [81, 105, 124, 75, 93, 103, 107] and has been observed in our initial clinical experience in the performance of IGLS [27]. Figure V.1 illustrates the range of soft tissue deformation imposed during clinical cases by the liver mobilization and packing procedures performed prior to resection (see Chapter IV for a more detailed summary of intra-operative deformation in IGLS).

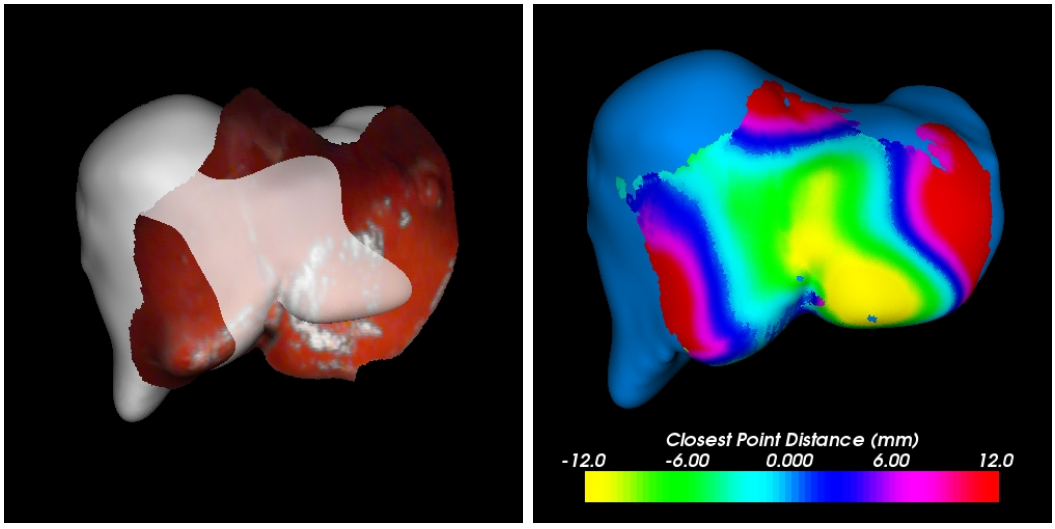

Figure V.1: Results of the salient feature registration [38] and the corresponding signed closest point distances for a single clinical case. The data set indicates the potential for closest point distances between the pre-operative CT and intra-operative LRS surfaces to be on the order of 2 cm which could likely compromise the guidance information provided by IGLS systems.

Based on the observed incidence of soft tissue deformation in IGLS, we seek to

provide compensation via an atlas-based approach similar to that originally proposed by Davatzikos *et al.* [46] Atlas-based approaches to deformation compensation have shown great promise in neurosurgery applications [52, 53] and we seek to expand on this work such that it will be amenable to IGLS. It should be noted that the implementation of atlas-based deformation compensation techniques to IGLS presents a unique challenge based on the fact that exact correspondence between the intra-operatively acquired sparse data (i.e. laser range scan (LRS) surface) and the pre-operative liver surface is not known. In neurosurgical applications, this point correspondence can be determined and allows for the computation of intra-operative brain shift [139]. The atlas-based techniques developed for neurosurgical applications are formulated based on these computed displacements which is not possible within the context of IGLS.

Related Work

The use of LRS data to drive a bio-mechanical model of the liver was initially proposed by Miga *et al.* [94] Building on this work, Cash *et al.* proposed an incremental approach to solving the model [28]. Additionally, this work demonstrated the use of a deformation identifying rigid registration (DIRR) which provided a more meaningful alignment than a traditional ICP registration. Other groups, such as Brock *et al.*, have used time dependent models to describe the liver motion due to respiration [21].

Recently, the use of atlas-based methods have been proposed for incorporation into IGS systems for the compensation of deformation. Dumpuri *et al.* have proposed the computation of a deformation atlas, provided by FEM solutions of a bio-mechanical model under a variety of conditions determined by *a priori* knowledge of the surgical procedure [53, 52]. The individual surface displacements predicted by the deformation atlas are then matched with those determined via cortical surface tracking with LRS using a constrained linear inverse model. Similar methods have been proposed by Davatzikos *et al.* [46] wherein a statistical approach based on principal component

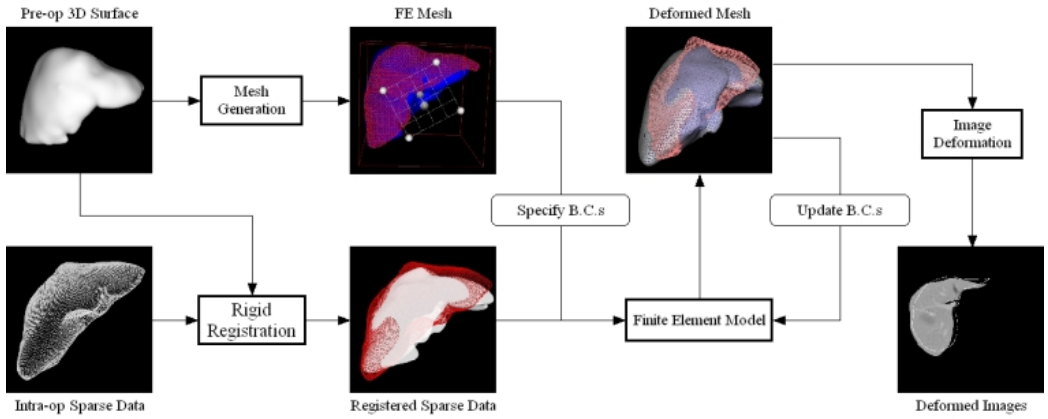

Figure V.2: Flow chart illustrating the incremental model-updating procedure for IGLS proposed by Cash *et al.*[28] The incremental model-update relies on multiple forward solutions of the FEM equations within the OR and, more importantly, a proper alignment of the intra-operatively acquired LRS data provided by the DIRR algorithm.

analysis (PCA), inspired by the work of Cootes *et al.* [43, 44], is used to fit deformed data to the atlas.

Objective

The objective of this work is to develop an atlas-based model updating method that is amenable to the application of IGLS. Given the results of the intra-operative liver deformation analysis in Chapter IV, the use of such a method seems appropriate within the context of IGLS given the implied similarity in deformation observed among similar surgical procedures. As mentioned previously, the development of such a method represents novel work due to the lack of point correspondence information as opposed to brain applications. While an initial version of the algorithm yielded comparable results to those provided by Cash *et al.* [28], a propensity to converge to local minima was observed [39]. Inspired by the increased robustness in rigid surface

based registrations provided by the algorithm developed in Chapter III, the incorporation of salient anatomical feature weighting in the proposed method will be explored to increase the robustness of the previously reported weighted patch ICP (PICP) algorithm [39]. Preliminary validation of the proposed atlas matching algorithm will be provided in the form of simulation and phantom experiments.

Methods

Overview

Figure V.3 outlines the four primary components of the proposed atlas-based model updating method for IGLS. The first two components of mesh and atlas generation, highlighted in grey, are performed pre-operatively using the diagnostic tomographic image volume as well as *a priori* information about the surgical procedure. This information is used to generate a relevant set of model solutions (i.e. model atlas) that will fully encompass the range of deformations that will be observed during a particular surgical procedure. The second two components (III and IV) of the deformation compensation paradigm are performed intra-operatively. Within the context of this work, the acquisition of intra-operative sparse data (d) will be assumed to be LRS surface data of the liver. Further, we are utilizing the salient feature surface registration developed within Chapter III as the method to initially register the intra-operative sparse data to the pre-operative CT data. It should be noted that the atlas-based method proposed herein would be amenable to other methods of intra-operative data acquisition and registration (e.g. iUS within the context of a vessel based registration framework).

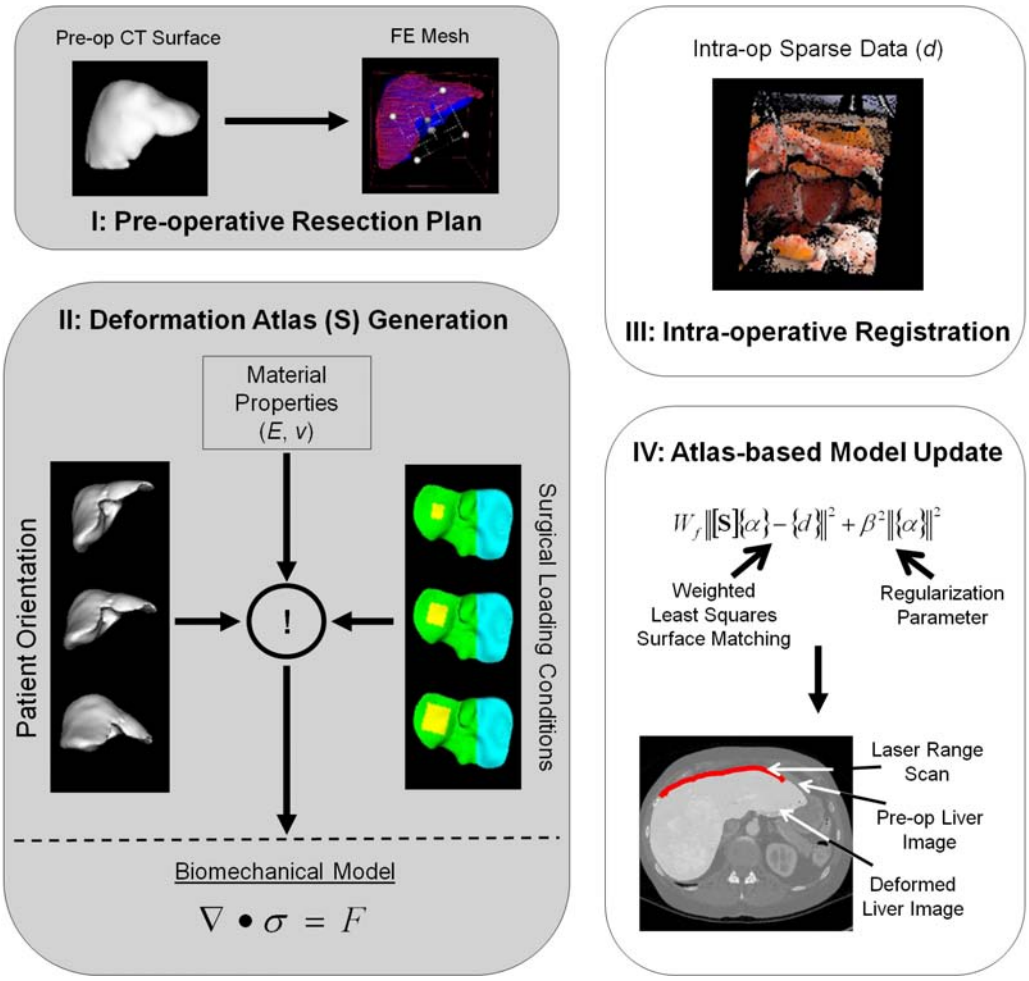

Figure V.3: Block diagram showing a general overview of the four primary components of the atlas-based model updating technique proposed for IGLS. The regions highlighted in grey indicated that they are performed pre-operatively while components III and IV are performed during the surgical procedure.

Model Equations and Boundary Condition Implementation

We begin with the assumption that the liver is an isotropic solid with a linear stress-strain relationship as in the work of Cash *et al* [28]. The equation for a linear-elastic 3D solid at static equilibrium is:

$$\nabla \cdot \tilde{\sigma} = \mathbf{B} \tag{V.1}$$

where $\tilde{\sigma}$ represents the stress tensor and $\mathbf{B}$ represents the body forces acting on the object. Hooke's law relates mechanical stress tensor ($\tilde{\sigma}$) to the mechanical strain tensor ($\tilde{\varepsilon}$) via the following relationship:

$$\tilde{\sigma} = C\tilde{\varepsilon} \tag{V.2}$$

where C represents the material stiffness matrix, which is dependent on the Young's Modulus (E) and Poisson's ratio (ν) material properties. Expanding Equation V.2 for the individual components of the stress tensor ($\tilde{\sigma}$) yields the following relationships:

$$\begin{aligned} \sigma_x &= \lambda(\varepsilon_x + \varepsilon_y + \varepsilon_z) + 2G\varepsilon_x & \tau_{xy} &= G\gamma_{xy} \\ \sigma_y &= \lambda(\varepsilon_x + \varepsilon_y + \varepsilon_z) + 2G\varepsilon_y & \tau_{xz} &= G\gamma_{xz} \\ \sigma_z &= \lambda(\varepsilon_x + \varepsilon_y + \varepsilon_z) + 2G\varepsilon_z & \tau_{yz} &= G\gamma_{yz} \end{aligned} \tag{V.3}$$

where σ_i is the normal stress in the i direction, τ_{ij} is the shear stress on the i face in the j direction, ε_i us the normal strain in the i direction, and γ_{ij} is the shear strain in the ij plane. The variables G and λ represent Lamé constants that can be expressed in terms of the Young's Modulus (E) and Poisson's ratio (ν) by the following equations:

$$G = \frac{E}{2(1+\nu)} \qquad \lambda = \frac{E\nu}{(1+\nu)(1-2\nu)} \tag{V.4}$$

Normal strain (ε_i) and shear strain (γ_{ij}) can also be expressed in terms of the displacement vector ($\mathbf{u} = \{u_x, u_y, u_z\}$) as follows:

$$\begin{aligned} \varepsilon_x &= \tfrac{\delta u_x}{\delta x} & \gamma_{xy} &= \tfrac{\delta u_x}{\delta y} + \tfrac{\delta u_y}{\delta x} \\ \varepsilon_y &= \tfrac{\delta u_y}{\delta y} & \gamma_{xz} &= \tfrac{\delta u_x}{\delta z} + \tfrac{\delta u_z}{\delta x} \\ \varepsilon_z &= \tfrac{\delta u_z}{\delta z} & \gamma_{yz} &= \tfrac{\delta u_x}{\delta y} + \tfrac{\delta u_y}{\delta x} \end{aligned} \tag{V.5}$$

By combining Equation V.1 through Equation V.5, a system of partial differential equations can be expressed in terms of the displacement vector ($\mathbf{u}$):

$$\frac{E}{2(1+\nu)}\nabla^2\mathbf{u} + \frac{E}{2(1+\nu)(1-2\nu)}\nabla(\nabla\cdot\mathbf{u}) = \mathbf{B} \tag{V.6}$$

In order to solve the system equations in Equation V.6 over the liver mesh domain, the Galerkin weighted residual method is applied using linear basis functions. Using this technique, the system of equations reflecting the displacement vectors ($\mathbf{u}$) at each node in the tetrahedral mesh can compiled in matrix form using the following relation:

$$K\mathbf{u} = \mathbf{B} \tag{V.7}$$

The driving force behind generating deformations with a FEM model is provided by the prescription of the appropriate conditions along the boundary of the tetrahedral mesh. Similar to the conditions described by Cash *et al.* [28], a set of three general boundary condition types will be used in the creation of the liver deformation atlas. The first type of condition we use is a Dirichlet zero displacement condition that is used to signify fixed regions of the liver that do not experience any displacement. This condition is generally prescribed to regions on the posterior surface of the right lobe and is described mathematically by the following relation:

$$\mathbf{u}(x, y, z) = 0 \tag{V.8}$$

The second type is condition used is a Dirichlet condition of specified non-zero displacement. We use these conditions to model the liver packing performed prior to resection and is typically prescribed to regions beneath the left lobe. The mathematical representation of this Dirichlet condition is similar to that shown in Equation V.8. However, the right hand side contains a function of the specified non-zero displacement. The final type of condition used in the liver model is a Neumann stress free condition used to signify regions that are unrestricted by force. This stress free condition is prescribed to a majority of the liver surface and is represented mathematically as follows:

$$\left.\frac{\partial \mathbf{u}}{\partial \mathbf{n}}\right|_{x,y,z} = 0 \tag{V.9}$$

In the application of displacement boundary conditions for anatomical soft tissue (i.e. the aforementioned Dirichlet conditions), it is often desirable to express the movement of the boundary in a coordinate system that is relative the the shape of organ of interest. A number of studies have shown that the specification of displacement boundary conditions normal to the surface of interest can be quite helpful in providing tissue-mimicking deformations [28, 94, 97]. One such strategy to implement a normal displacement condition is to convert the normal displacement to its Cartesian representation:

$$\begin{Bmatrix} dn \\ dt_1 \\ dt_2 \end{Bmatrix} = \begin{bmatrix} \vec{x}\cdot\vec{n} & \vec{y}\cdot\vec{n} & \vec{z}\cdot\vec{n} \\ \vec{x}\cdot\vec{t_1} & \vec{y}\cdot\vec{t_1} & \vec{z}\cdot\vec{t_1} \\ \vec{x}\cdot\vec{t_2} & \vec{y}\cdot\vec{t_2} & \vec{z}\cdot\vec{t_2} \end{bmatrix} \begin{Bmatrix} dx \\ dy \\ dz \end{Bmatrix} \tag{V.10}$$

where $\vec{n}$, $\vec{t_1}$, and $\vec{t_2}$ represent an orthogonal coordinate system with the normal (to

the organ surface) and two orthogonal tangential axes, respectively. By utilizing the inverse of the relationship shown in Equation V.10 a displacement specified normal to the organ boundary can be imposed via it's Cartesian components. However, using the above relation, it is not possible to implement so called "mixed" boundary conditions. In certain scenarios it may be useful to allow an organ surface to slide along a supporting plane tangent to the surface and not deform in the normal direction. Additionally, it may also be useful to apply deformation in a direction normal to the surface and also allow the tissue to slide tangent to the displacing surface (e.g. the depression of a tissue surface with a retractor). These types of conditions require stress-free conditions to be imposed tangent to (i.e. $\vec{t_1}$ and $\vec{t_2}$) the specified normal displacement direction ($\vec{n}$):

$$\sigma_{t1} = \sigma_{t2} = 0, u_n = u_s \tag{V.11}$$

where $\sigma_{t1,t2}$ are the stresses applied tangent to the organ surface and u_s signifies the specified displacement normal the surface.

Being that the framework described by Equation V.10 does not posses the ability to achieve the necessary degrees of freedom for "mixed" boundary condition employment, the normal-tangential procedure described by Engelman *et al*. [54] is used. The normal-tangential framework is performed by rotating the equations for the nodes of interest via application of rotation matrices at the local element assembly level:

$$[R]_i[K]_i[R^T]_j\{\mathbf{u}\}_j = [R]_i\{\mathbf{b}\}_i \tag{V.12}$$

where pre-multiplication of by $[R]_i$ (the rotation matrix shown in Equation V.10 associated with the normal and tangential coordinate reference of the ith node) on the left and right-hand side rotates the equilibrium equation and body force vector, and the $[R^T]_j$ matrix rotates the displacement vector from the Cartesian coordinate

frame into the normal-tangential frame. In Equation V.12, the i and j indices are reference to the ith weighted residual equation and the jth displacement coefficient.

Deformation Atlas Creation

A primary factor in determining the success of atlas-based methods of registration is the process of atlas creation to ensure that the range of possible deformations, based on the pre-operative plan for a particular patient and *a priori* knowledge of surgical loading conditions, are contained within the atlas. The process of atlas construction begins with the generation of a volumetric mesh of the liver which is derived from the surface description provided by a segmentation of the pre-operatively obtained tomographic image volumes. As in previous work, a semi-automatic method developed by Dawant *et al.* [47, 115], based on the level set method proposed by Sethian [134], was used to segment the liver from the surrounding anatomical structures in the pre-operative tomograms. The liver isosurfaces were generated from the liver segmentations via the Marching Cubes Algorithm [84] and smoothed via radial basis functions (FastRBF toolkit, FarField Technology, Christchurch, New Zealand). Given the interpolated liver surface, we employ the algorithm described by Sullivan *et al.* [148] to generate the tetrahedral volumetric liver mesh. Once the mesh has been created, a set of boundary conditions, range of patient orientations (i.e. gravity directions), and range of material properties are selected based on *a priori* information about the surgical procedure. Once the set of conditions have been determined, the model is run for each permutation of the sets of conditions and the deformed volumetric and surface meshes for each model solution are then saved for incorporation into the surface matching algorithm (see Figure V.3).

Iterative Closest Atlas Algorithm

Once the set of model solutions have been computed and the deformed liver volume meshes and surfaces have been compiled, the collected intra-operative data (i.e. LRS scan of the liver surface) is then fit to the atlas via the Iterative Closest Atlas (ICAt) Algorithm. Similar to the work performed by Dumpuri *et al.* [52, 53], a simple linear model is used within algorithm to fit the intra-operative sparse data to the pre-operatively computed atlas of model solutions. Due to the problem of point correspondence mentioned previously, the linear model is formulated in terms of the actual surface data, rather than in terms of computed displacements in the work of Dumpuri *et al.*, as follows:

$$\mathbf{W}_f \mathbf{S} \phi = d \tag{V.13}$$

where $\mathbf{W}_f$ is an $[(N \times 3) \times (N \times 3)]$ diagonal matrix of point weighting parameters, $\mathbf{S}$ is an $[(N \times 3) \times M]$ model atlas matrix, ϕ is an $[M \times 1]$ vector representing weighting coefficients for each model solution, d is an $[(N \times 3) \times 1]$ vector representing the intra-operative data, M represents the number of model solutions contained in the atlas, and N is the total number of nodes in the intra-operative sparse data acquisition d. It should be noted that the $\mathbf{W}_f$ is populated on the diagonal with the weight factor $(w_P BR)$ based on the indices of the salient feature points in d and with a value of one for the non-feature indices. Similar to the work in Chapter III, the relaxation schedule shown in Equation III.3 is utilized to reduce the salient feature weighting within $\mathbf{W}_f$ as the algorithm proceeds. We choose a least squares formulation to obtain the solution of Equation V.13, which is equivalent to the following formulation:

$$\phi = (\mathbf{S}^T \mathbf{W}_f \mathbf{S})^{-1} \mathbf{S}^T \mathbf{W}_f \mathbf{d} \tag{V.14}$$

Due to the fact that the condition number of the matrix $\mathbf{S}^T \mathbf{W}_f \mathbf{S}$ is extremely

large, the inverse formulation is V.14 is ill-conditioned in the sense of Hadamard [152]. In order to stabilize the results of the solution of Equation V.14, we employ a Tikhonov regularization process where we seek to find a ϕ to minimize:

$$W_f \|\mathbf{S}\phi - d\|^2 + \beta^2 \|\phi\|^2 \tag{V.15}$$

where $\|\cdot\|$ is the Euclidean norm and β is called the Tikhonov factor. The least squares formulation in Equation V.14 now becomes:

$$\phi = (\mathbf{S}^T \mathbf{W}_f \mathbf{S} + \beta^2 I)^{-1} \mathbf{S}^T d \tag{V.16}$$

where I is the $M \times M$ identity matrix. We chose to use the following Tikhonov factor (β^2) used by Jaochimowicz *et al.* [78] for the solution of a similar inverse problem:

$$\beta^2 = \lambda \Big[1/N \sum_{j=1}^{N} \mathbf{S}^T \mathbf{W}_f \mathbf{S}(j,j) \Big] [d_{err}]^2 \tag{V.17}$$

where the parameter λ is a weighting parameter that represents the magnitude of β^2, which is empirically determined based on the convergence of the problem. The middle term represents the trace of the matrix $\mathbf{S}^T \mathbf{W}_f \mathbf{S}$, which improves the conditioning of the matrix by reducing the gap between its higher and lower eigenvalue. The final term ($[d_{err}]^2$) is a relative mean square error term used to decrease the weight of β^2 as the method converges and is defined as follows:

$$d_{err} = \sqrt{\frac{\sum_{i=1}^{N} |\Delta d_k(i)|^2}{\sum_{i=1}^{N} |d(i)|^2}} \tag{V.18}$$

where $\Delta d_i = S_{cp} - d$ at iteration i and j is the point index. In other words, d_{err} represents the relative error between the true point location (d) and the atlas

reconstructed point location (S) at each iteration. The difference in $\Delta d_i = S_{cp} - d$ between iterations is used as one of the stopping criteria.

Note that the expression in Equation V.13 inherently implies a known correspondence between mesh surface points and the intra-operative surface data points. Being that this correspondence is not known with any certainty within the context of IGLS, an iterative approach is used whereby point correspondence is updated at each iteration following computation of the current atlas solution based on the values of the weighting coefficients (ϕ) at the current iteration. Given an initial alignment of the intra-operative data set (d) with the pre-operative CT surface using the salient feature registration algorithm described in Chapter III, the algorithm proceeds as follows:

Algorithm Initialization:

Step 1. Let iteration number $i = 0$. Initialize $w_{PBR} = w_{PBR,max}$ and generate weighting matrix $\mathbf{W}_f$. Using the weighted point correspondence method ($C^*_{d \rightarrow S}$) described in Equation III.1, compute the set of closest points to d on the pre-operative CT surface mesh, denoted as S_{cp}.

Step 2. Generate a new atlas matrix using the closest point indices computed **Step 1**, $\mathbf{S_{cp}}$ and solve for the initial set of atlas weighting parameters (ϕ_0) by solving Equation V.16. Compute the current model solution using the relationship $S = \mathbf{S}\phi_0$.

Weighted Point Registration Phase:

Step 3. Increment iteration count ($i = i + 1$). Compute the weighted rigid body transformation (T_{d-S}) between the data point set (d) and S using the weighted point correspondence method ($C^*_{d \rightarrow S}$) as in the salient feature registration algorithm developed in Chapter III.

Step 4. Transform the data point set (d) using transformation computed in **Step 3** and re-compute the closest points on S to the transformed data points d, which we will call S_{cp}, again using the weighted point correspondence method. Build a new atlas matrix ($\mathbf{S}_{cp}$) containing only the indices of the points in S_{cp}.

Linear Model Solution Phase:

Step 5. Compute the new set of weighting parameters (ϕ_i) by solving the linear equation $\mathbf{W_f S}_{cp}\phi_i = d_{cp}$ using the least squares formulation of Equation V.16.

Step 6. Compute new model solution using the relationship $S = \mathbf{S}\phi_i$. Increment w_{PBR} using the relaxation schedule described in Equation III.3 and update the weighting matrix $\mathbf{W}_f$. Repeat **Step 3** through **Step 6** until i exceeds maximum number or residual error tolerance (Δd_i) is satisfied.

Validation: Simulation Experiment

The initial validation experiments for the ICAt algorithm involved the performance of a set of simulation trials. First, an atlas was created using one of the liver meshes obtained from the segmentation of a clinical data set (shown in Figure V.4). The following parameters were used in the generation of the atlas: initial gravity vector ($\vec{g}$) = (0.7071,0.7071,0.0), Young's modulus (E) = 15 kPa, Poisson's ratio (ν) = 0.47 and ρ = 1000.0 kg/m^3. The distribution of boundary conditions used to generated the atlas are shown in Figure V.4. The patient orientation was varied to create a atlas of 121 solutions by rotation of $\vec{g}$ about the y- and z-axes where the values of the rotation angles (θ^y and θ^z) were varied between -50° and 50° in increments of 10°. In order to generate a set of source data, simulating deformed LRS scans, five separate deformed meshes were created by using randomly generated rotation angles for θ^y and θ^z within the range of that used to create the atlas (i.e. $\theta^y, \theta^z \in [-50°, 50°]$). Once the deformed meshes were created, a subset of the surface

points, which were obtained by extracting the region corresponding with the coverage of the acquired LRS data (shown in Figure V.4), were used to realistically simulate the surface coverage of true intra-operative data. The falciform region was manually segmented on the CT liver surface (shown in Figure V.4) and was used for biasing the point correspondence determination and within the feature weighting described previously. It should be noted that the parameters used to create the deformation atlas were chosen such that considerable deformations would be imposed and not to reflect parameters that would be used in the generation of a deformation atlas to model actual intra-operative data.

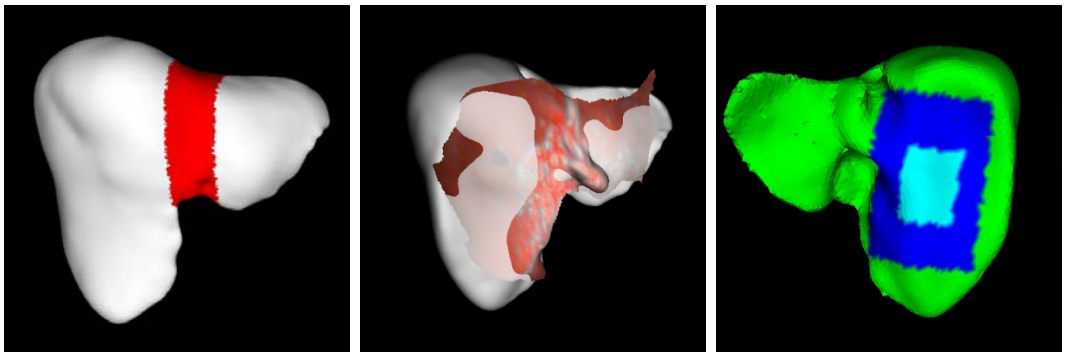

Figure V.4: The liver surface mesh (left), the ICP registration result (center), and the boundary condition distribution (right) used to create the deformation atlas for the ICAt simulation experiments. The ICP registration result is shown to give the reader an indication of the size of the simulated scans relative to the full liver surface. For the distribution of boundary conditions, the green area corresponds with the Neumann "stress free" condition, the light blue area corresponds with the Dirichlet "fixed" condition, and the dark blue region corresponds with the normal-tangential Dirichlet "fixed" condition where $u_n = 0$.

Once the deformation atlas and the sets of simulated LRS data had been generated, ICAt solutions were computed using both the initial formulation described in [39] (denoted as ICAt[1]) and the atlas matching algorithm utilizing feature weighting

[1]This version of the algorithm does not include any biasing in the point correspondence using the method described in Equation III.1 nor is any sort of point weighting utilized. The $\mathbf{W}_f$ term

described herein (denoted as ICAt*) using both the simulated LRS scan and full surface data. The errors are reported over all nodes in the mesh prior to rigid registration and after rigid surface registration using ICP and the PICP for the ICAt and ICAt* trials, respectively. Finally, errors are reported for the ICAt and ICAt* solutions using both the simulated LRS scan and full surface. For reference, the maximum number of iterations was set to 1000 and the convergence tolerance was set to 1e-6 mm. The weighting factor (λ) for the Tikhonov regularization parameter in Equation V.17 was set to 0.01. For the ICAt* trials, the following empirically determined parameters were used: $w_{PBR,max} = 2000$, $w_{PBR,base} = 1$, and $\alpha = 0.001$.

Validation: Phantom Experiment

A set of experiments were performed using an anthropomorphic liver model created using Smooth-On Ecoflex 00-10 (Smooth-On, Easton, PA). The liver phantom was rigidly attached to the plexiglass base used in Chapter III with a Teflon screw through the phantom in the region of the vena cava on the posterior surface, which serves as an anatomically realistic method to affix a region of the liver. The plexiglass base has a set of seven white Teflon spheres resting atop cylindrical holders of various heights which surround the liver phantom. These spheres can be localized in both CT and LRS images reliably and serve to provide landmarks for point-based registrations (PBR) between the various imaging data collected (see Figure III.5 for example images of the Tephlon spheres from CT and LRS modalities). A set ($N = 43$) of 1 mm steel beads (Boca Bearing Company, Delray Beach, FL) were distributed throughout the phantom to serve as sub-surface targets for error calculation. Also, a stripe of white paint was placed on the phantom in the falciform ligament region to

is removed from this formulation and the algorithm is initialized with ICP instead of the salient feature based surface registration.

facilitate the delineation of this anatomical feature in the LRS data. The positions of the distributed steel beads within the liver phantom are shown in Figure V.5.

As shown in Figure V.5, two separate deformations were then imposed on the phantom using a surgical towel: left lobe and inferior ridge of right lobe. A set of CT (Mx8000, Phillips Medical Systems, Bothell, WA) and LRS (RealScan 200C,3-D Digital Corporation, Bethel, CT) imaging data were acquired in the pre-deformed state and both deformed states of the anthropomorphic phantom. The phantom was segmented from the three image volumes and isosurfaces were generated. A tetrahedral volumetric mesh was generated from the pre-deformed phantom isosurface for use in deformation atlas generation. The sphere fiducials were localized in the LRS scan using a least squares sphere fitting method described by Ahn *et al.* [1] and the sphere centroids were computed in the CT image volume using a region growing algorithm implemented within the Analyze software package (Analyze AVW Version 6.0, Mayo Clinic, Rochester, MN). Centroids of the implanted steel targets were localized using the method developed by Wang *et al.* [156]

To perform the ICAt algorithm on the phantom data sets, an atlas of model solutions was created based on the *a priori* knowledge that left lobe and inferior ridge of the right lobe would experience deformation as well as the fact that the liver region near the vena cava would not experience any displacement. Using the volumetric mesh created from the un-deformed phantom, a set of 20 boundary conditions were created with varying regions undergoing normal displacement corresponding with the knowledge of the imposed deformation. A sample of the boundary condition set is visualized in Figure V.6. The imposed normal displacement (u_n) was varied from 5 mm to 4.5 cm in 5 mm increments which yielded an atlas of 180 model solutions. In solving the linear elastic FEM, the following parameters were utilized: Young's modulus (E) = 270 kPa, Poisson's ratio (ν) = 0.47 and ρ = 1040.0 kg/m^3.

Upon generation of the deformation atlas, ICAt and ICAt* solutions were for the

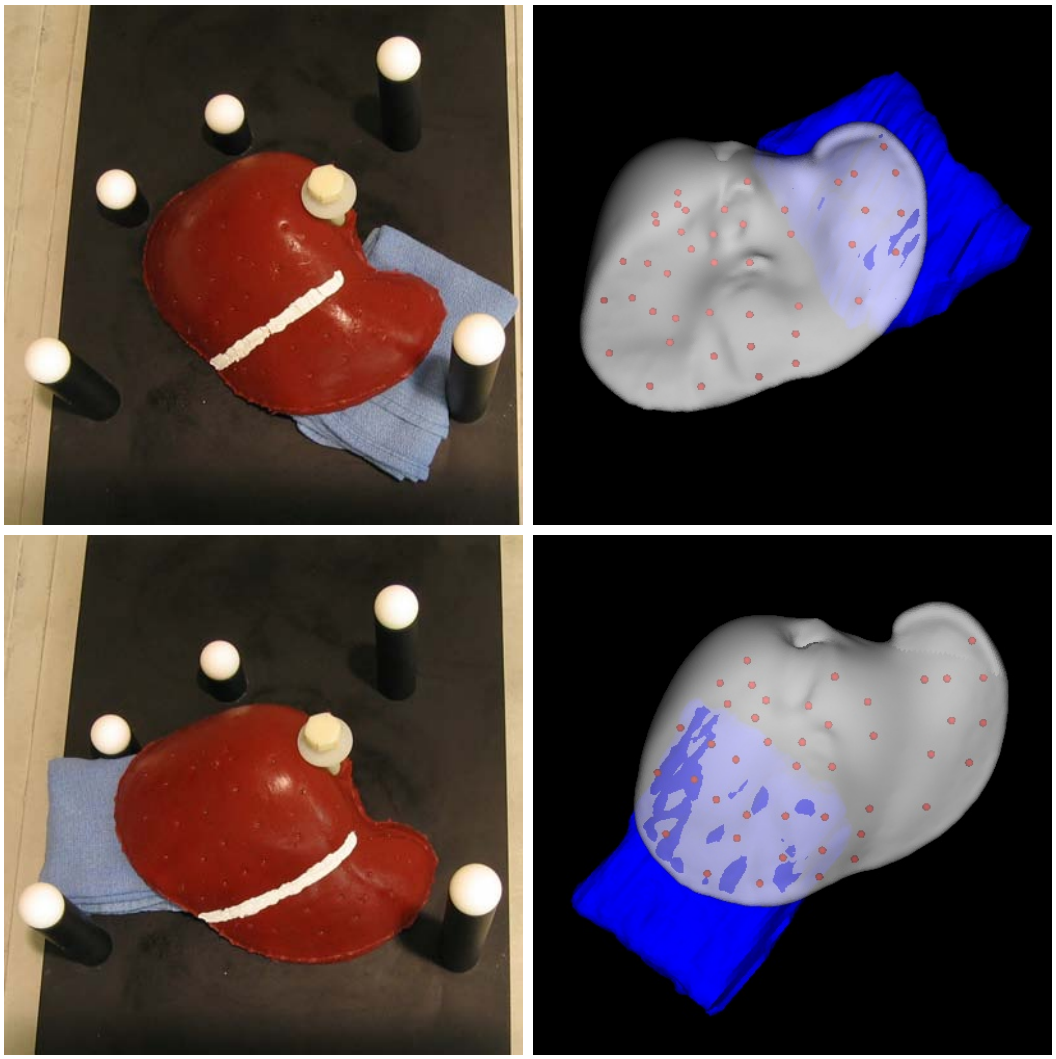

Figure V.5: Image of the anthropomorphic liver phantom with the left lobe (top row) and right lobe (bottom row) deformations. A surgical towel was placed underneath the left and right lobes of the liver phantom to simulate deformation imposed by liver packing performed during surgery. The left column shows the phantom along with the surrounding Tephlon spheres. The right column shows the distribution of sub-surface targets ($N = 43$) within the phantom.

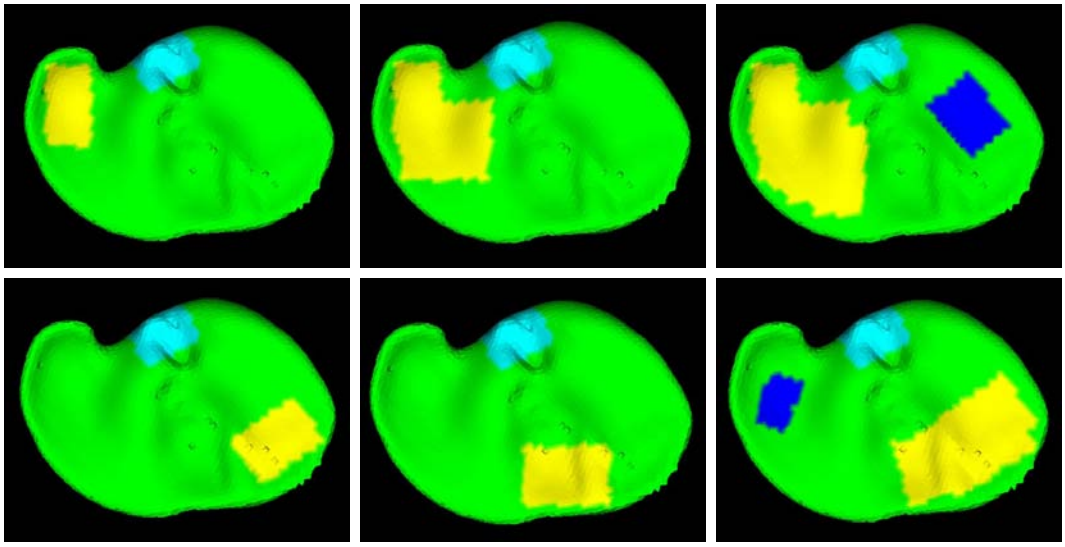

Figure V.6: Visualizations of a sample of the boundary conditions used to generated the atlas of model solutions for the phantom trials. The green area corresponds with the Neumann "stress free" condition, the light blue area corresponds with the Dirichlet "fixed" condition, the dark blue region corresponds with the normal-tangential Dirichlet "fixed" condition where $u_n = 0$, and the yellow area represents the regions over which a non-zero normal displacement (u_n) is specified.

two imposed deformations. As in the simulation trials, both the full surface and partial surface (i.e. LRS surface data) were utilized. The ICAt and ICAt* algorithms were initialized with their corresponding ICP and PICP rigid body surface registration results. For reference, the maximum number of iterations was set to 1000 and the convergence tolerance was set to 1e-6 mm. The weighting factor (λ) for the Tikhonov regularization parameter in Equation V.17 was set to 0.01. For the ICAt* trials, the following empirically determined parameters were used: $w_{PBR,max} = 2000$, $w_{PBR,base} = 1$, and $\alpha = 0.001$. The output displacements from the ICAt and ICAt* solutions were then interpolated via the mesh basis functions to deform the sub-surface bead locations for error analysis.

Finally, a small robustness trial was performed by perturbing the initial alignment provided by the rigid surface registration method over 25 trials to ascertain the impact of initial alignment on the determination of a unique solution. The perturbations were achieved via generation of a random six degree-of-freedom transformations using a uniformly distributed random number generator to supply the rotation parameters ($\theta^x, \theta^y, \theta^z$) and translation parameters (t^x, t^y, t^z). The rotation parameters were generated on the interval [-5°,5°] and the translation parameters were generated on the interval [-5 mm,5 mm]. The results of the perturbation trials were compared by direct observation of the absolute differences in the solution LSQ weighting factors (ϕ) as well as via comparison of the sub-surface target errors.

Results

Simulation Experiments

The simulation trial results are shown in Table V.1 and Table V.2. The error values reported describe the true error averaged over all of the nodes in the mesh using the known point correspondence. The errors shown in the first column of both Table V.1 and Table V.2 represent the mean error prior to any registration between the

Trial	Pre (mm)	Full Surface		Partial Surface	
		Post-ICP (mm)	Post-ICAt (mm)	Post-ICP (mm)	Post-ICAt (mm)
1	11.8(50.8)	7.6(24.2)	0.1(0.1)	9.9(22.8)	0.2(0.3)
2	14.1(59.2)	6.6(22.8)	0.3(0.3)	8.6(25.4)	5.0(10.3)
3	9.1(72.2)	8.3(23.6)	0.1(0.2)	10.3(22.3)	3.2(5.5)
4	13.3(57.9)	5.7(15.5)	0.1(0.2)	7.9(19.3)	5.0(8.5)
5	10.3(69.1)	8.0(23.7)	0.2(0.2)	10.2(23.0)	3.1(5.4)
mean	**11.7(64.4)**	**7.2(22.0)**	**0.2(0.2)**	**9.4(22.6)**	**3.3(6.0)**

Table V.1: Summary of simulation results depicting the node errors over entire 3D mesh for each deformation trial using both the full surface and partial surface (i.e. simulated scan) to drive the ICAt algorithm without point weighting (described in [39]). The values shown in parentheses are maximum errors. The relatively high error value for the partial surface solution of Trials 2 through 5 seem to indicate convergence to a local minimum.

five randomly deformed meshes and the pre-deformed mesh with the maximum error value shown in parentheses. The final four columns shown in Figure V.1 summarize the results of rigid ICP registration using both the full surface and the simulated LRS scan data along with the results of the ICAt algorithm using both full and partial surface data in terms of mesh node error. In general, the ICAt solution provides a significant decrease in the overall mesh error in comparison with a rigid registration. However, the ICAt solutions obtained using only the simulated LRS scan data provide significantly larger errors for four of the five trials. Similar to the results shown in [39], this result seems to indicate that the algorithm has a propensity for local minima convergence when sparse surface data is utilized.

The results shown in Table V.2 summarize the results of the rigid falciform region based PICP registration using both the full surface and simulate LRS scan data along with the result of the ICAt* algorithm using both full and partial surface data in terms of mesh node error. When compared with the results show in Figure V.1, it can be seen that algorithm provides significantly better results with respect to the partial surface (i.e. simulated LRS scan) trials, where four of five trials are shown

Trial	Pre (mm)	Full Surface		Partial Surface	
		Post-PICP (mm)	Post-ICAt* (mm)	Post-PICP (mm)	Post-ICAt* (mm)
1	11.8(50.8)	6.2(29.8)	0.1(0.2)	8.7(32.0)	0.1(0.3)
2	14.1(59.2)	5.8(28.3)	0.1(0.3)	11.8(30.7)	3.9(5.7)
3	9.1(72.2)	7.1(31.9)	0.04(0.1)	7.7(35.5)	0.2(0.4)
4	13.3(57.9)	6.2(17.6)	0.1(0.2)	8.4(22.3)	0.2(0.4)
5	10.3(69.1)	6.8(31.3)	0.1(0.2)	7.9(31.3)	0.1(0.3)
mean	**11.7(64.4)**	**6.4(27.8)**	**0.1(0.2)**	**8.9(30.4)**	**0.9(1.4)**

Table V.2: Summary of simulation results depicting the node errors over entire 3D mesh for each deformation trial using both the full surface and partial surface (i.e. simulated scan) to drive the ICAt algorithm. ICAt* denotes the version of the algorithm utilizing patch point weighting. The values shown in parentheses are maximum errors. The relatively high error value for the partial surface solution of Trial 2 seems to indicate convergence to a local minimum.

to converge to results with sub-millimetric mesh errors. The large disparity between the mesh errors reported between the ICAt* solution generated with full surface and partial surface data for Trial 2 seems to indicate that the algorithm converged to an inaccurate local minimum.

Phantom Experiments

Qualitative visualizations of the results of the phantom experiments are shown in Figure V.7 and Figure V.8 for the right and left lobe deformations, respectively. The visualizations display the closest point distance values between the deformed LRS data and non-deformed CT surface after point based registration (PBR) using the sphere fiducials. The closest point distances have been mapped on the non-deformed phantom liver surfaces to provide an indication of the magnitude of deformation imposed by the surgical towel packing and also to indicate the region over which LRS data was acquired for the two deformation cases. Further, the closest point distances computed between the deformed full CT surfaces and the non-deformed phantom surface based on the rigid ICP and PICP rigid registration whereby the full

surfaces were transformed with the transformation generated by registration of the deformed LRS data with the non-deformed CT phantom surface using the ICP and PICP registration methods. Finally, the closest point distances are visualized upon generation of solutions utilizing the ICAt and ICAt* methods via partial surface (i.e. LRS data) and full surface input data.

The qualitative visualizations indicate that significant improvement in the surface matching is achieved by utilizing the proposed atlas matching algorithm. In particular, the ICAt* algorithm converges to quite accurate results when the full deformed surface, which is generated from the CT volumes of the deformed phantom, is utilized. Also, the ICAt* algorithm achieves better results when compared with the original ICAt implementation in the case where only partial surface (i.e. LRS data) is used. While the results presented using the full deformed surface in determining the ICAt* does not have clinical relevance due to the inability to acquire the full liver surface in a surgical environment, the results show the impact of surface coverage on the performance of the algorithm. In general, the acquisition of more extensive intra-operative surface digitizations will yield more accurate results.

The sub-surface target errors for the phantom trials are summarized in Table V.3 and Table V.4 for the ICAt and ICAt* trials, respectively. The target error measurements displayed echo the qualitative visualization of the results. The solutions provided by the ICAt and ICAt* algorithms when the full surface data was utilized yields are quite accurate and provide a large improvement over the rigid registration errors. The sub-surface target errors are lower in all cases for the ICAt and ICAt* solutions using full surface data which indicates the importance of intra-operative surface coverage. Further, the solutions provided by the ICAt* for the partial LRS surface for both deformation cases are more accurate with respect to the sub-surface target measurements than the analogous solutions provided by the ICAt implementation without feature weighting. Visualizations of the distribution of target errors for

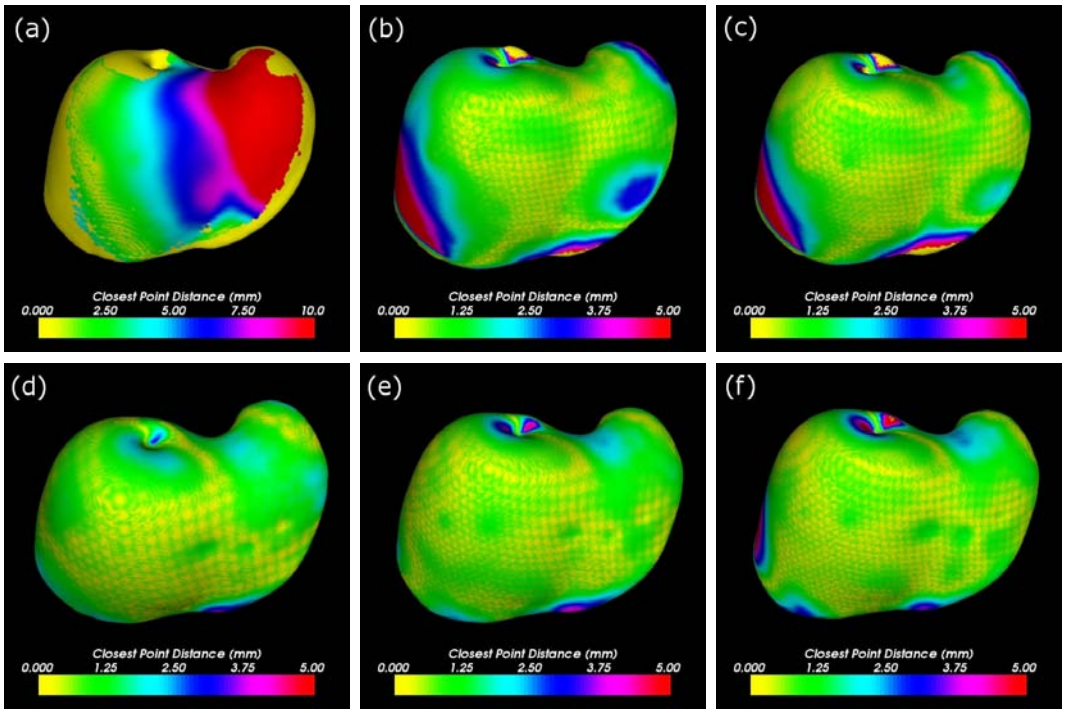

Figure V.7: Qualitative results for the left lobe phantom deformation via display of the closest point distance between deformed LRS data and non-deformed CT surface after point based registration (PBR) based on sphere fiducials (a). Closest point distance between the deformed full CT surface and non-deformed CT surface after PICP registration (b) and ICP registration (c) using the deformed LRS data are also shown. The closest point distances between deformed CT surface and the ICAt* solution surfaces computed with the full surface and LRS surface are shown in (d) and (e), respectively. The closet point distances between the deformed CT surface and the ICAt solution surface computed using the LRS data is shown in (f). For reference, the mean residuals for the PBR, PICP registration, ICP registration, ICAt* solution using full surface, ICAt* using LRS surface and ICAt solution using LRS data were found to be 7.3 mm, 2.1 mm, 1.8 mm, 1.0 mm, 1.3 mm and 1.7 mm, respectively.

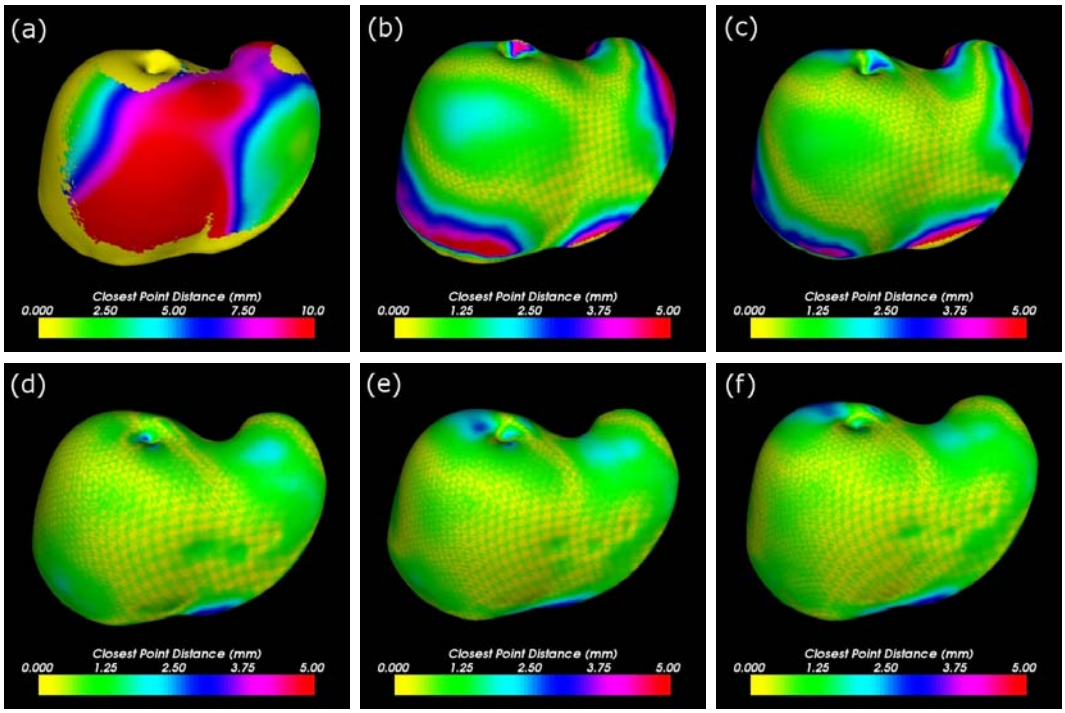

Figure V.8: Qualitative results for the right lobe phantom deformation via display of the closest point distance between deformed LRS data and non-deformed CT surface after point based registration based on sphere fiducials (a). Closest point distance between the deformed full CT surface and non-deformed CT surface after PICP registration (b) and ICP registration (c) using the deformed LRS data are also shown. The closest point distances between deformed CT surface and the ICAt* solution surfaces computed with the full surface and LRS surface are shown in (d) and (e), respectively. The closet point distances between the deformed CT surface and the ICAt solution surface computed using the LRS data is shown in (f). For reference, the mean residuals for the PBR, PICP registration, ICP registration, ICAt* solution using full surface, ICAt* using LRS surface and ICAt solution using LRS data were found to be 8.5 mm, 2.0 mm, 1.9 mm, 0.9 mm, 1.2 mm and 1.3 mm, respectively.

the left lobe and right lobe inferior ridge deformation trials are shown in Figures V.9 and V.10, respectively. Note that the target error distribution figures are displayed in an analogous fashion to the qualitative visualizations shown in Figure V.7 and Figure V.8.

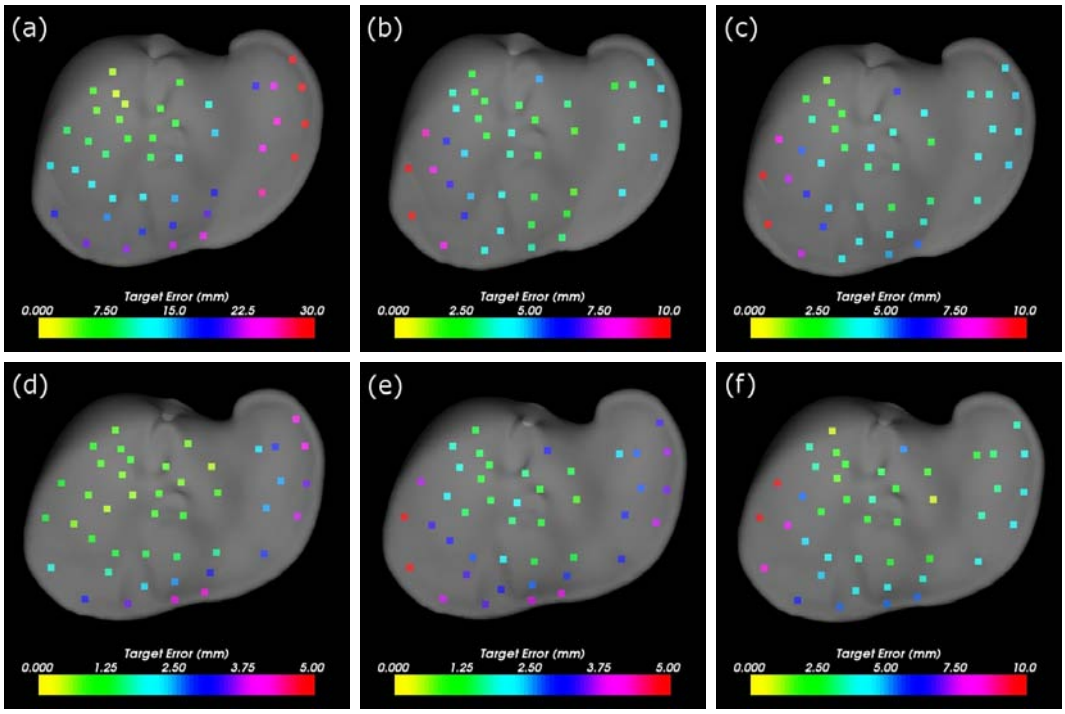

Figure V.9: Visualization of the distribution of target errors for the left lobe phantom deformation case. The distributions are shown for the PBR (a), PICP registration (b), ICP registration (c), ICAt* solution computed with the full surface (d), ICAt* solution computed with partial surface (ie. LRS data) (e), and ICAt solution computed with partial surface (i.e. LRS scan) (f). The error distributions shown are analogous to the qualitative results shown in Figure V.7.

As shown in Figures V.9 and V.10, the regions where the deformation was imposed (via placement of a surgical towel) correspond with those that experienced the largest sub-surface target displacement as indicated by the errors calculated via point-based registration. The results of the rigid surface registrations (ICP and PICP) performed using the LRS data for both deformation cases yielded the largest target errors in the

Deformation	Pre (mm)	Full Surface		Partial Surface	
		Post-ICP (mm)	Post-ICAt (mm)	Post-ICP (mm)	Post-ICAt (mm)
Left	14.8±8.5(31.0)	3.3±1.6(6.2)	1.9±1.2(4.4)	4.4±2.0(10.9)	4.0±2.6(14.3)
Right	22.8±8.8(42.3)	2.3±1.3(6.9)	1.1±0.6(2.4)	4.3±2.0(8.8)	3.3±1.5(7.4)

Table V.3: Summary of sub-surface targeting ($N = 43$) errors for the phantom validation trials where ICAt solution was determined using both full CT surface data and partial surface (i.e. LRS) data. Maximum target errors are shown in parentheses. Target errors were calculated after rigid point based registration (Pre), rigid surface registration without incorporation of salient features (Post-PICP), and after atlas-based model updating using the original formulation without feature weighting (Post-ICAt).

Deformation	Pre (mm)	Full Surface		Partial Surface	
		Post-PICP (mm)	Post-ICAt* (mm)	Post-PICP (mm)	Post-ICAt* (mm)
Left	14.8±8.5(31.0)	3.2±1.6(6.8)	1.8±1.2(4.2)	4.1±2.3(11.3)	2.5±1.1(5.4)
Right	22.8±8.8(42.3)	2.7±1.6(6.7)	1.1±0.5(2.3)	4.5±2.2(10.0)	2.5±1.1(5.3)

Table V.4: Summary of sub-surface targeting ($N = 43$) errors for the phantom validation trials where ICAt* solution was determined using both full CT surface data and partial surface (i.e. LRS) data. Maximum target errors are shown in parentheses. Target errors were calculated after rigid point based registration (Pre), rigid surface registration with feature weighting (Post-PICP), and after atlas-based model updating with feature weighting (Post-ICAt*).

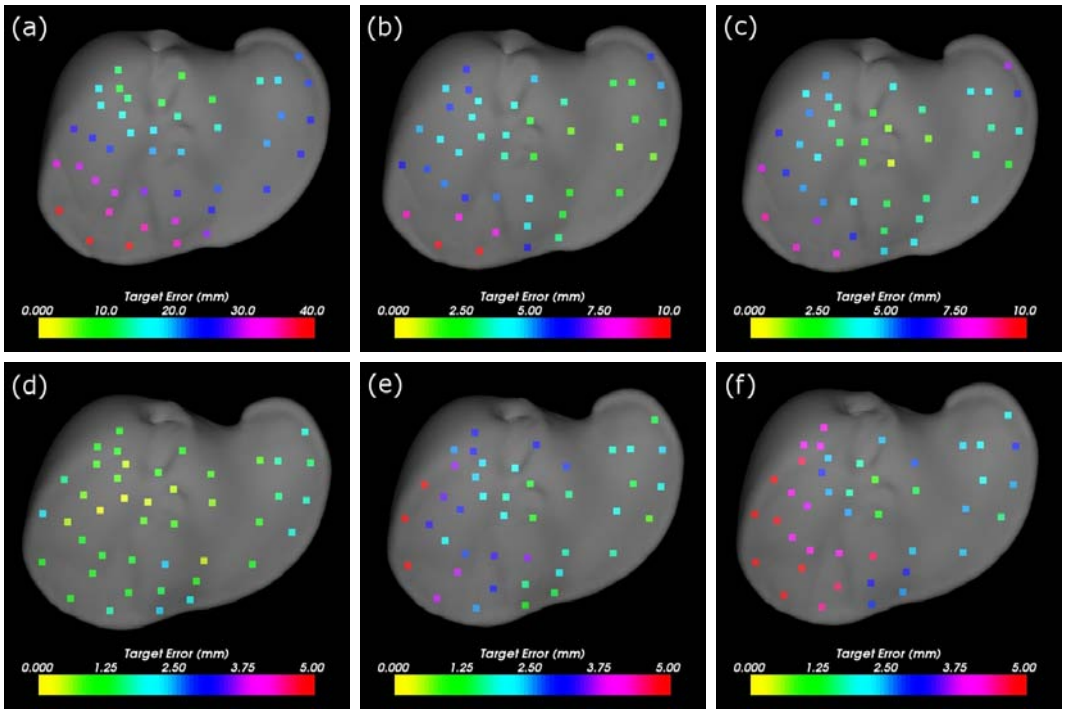

Figure V.10: Visualization of the distribution of target errors for the right lobe phantom deformation case. The distributions are shown for the PBR (a), PICP registration (b), ICP registration (c), ICAt* solution computed with the full surface (d), ICAt* solution computed with partial surface (ie. LRS data) (e), and ICAt solution computed with partial surface (i.e. LRS scan) (f). The error distributions shown are analogous to the qualitative results shown in Figure V.8.

right lobe of the phantom. Incidentally, the regions showing the largest sub-surface error corresponded with those regions where LRS data was not acquired (shown in Figures V.7 and V.8). Similar results are shown for the distribution of sub-surface errors for the ICAt and ICAt* solutions using partial surface data where regions further away from where LRS coverage was obtained yielded the largest sub-surface target error. The error distributions for the ICAt* solutions computed with the full surface data are more evenly distributed with the smaller errors closer to the vena cava region where displacement are minimized due to the placement of the Teflon screw.

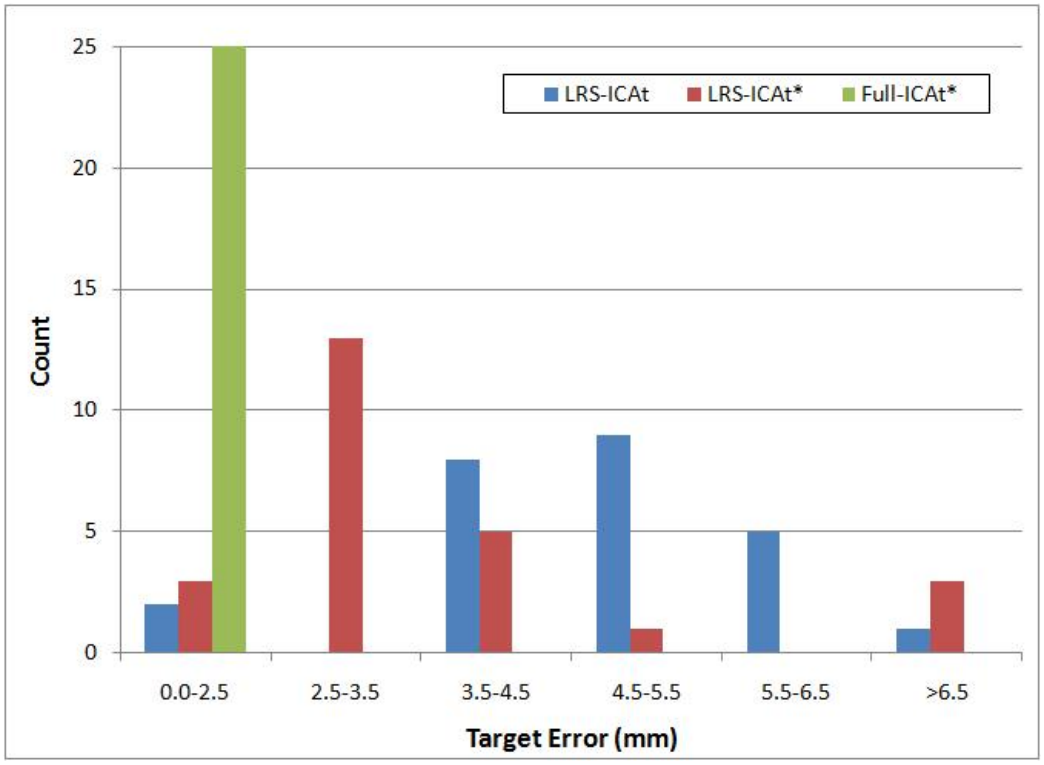

Figure V.11: Histogram summary of the sub-surface target errors from the perturbation trial ($N = 25$) preformed using the ICAt algorithm with partial surface (i.e. LRS) data and the ICAt* algorithm with both full and partial surface data. For reference, the mean target errors over the trials were found to be 4.8±1.1, 4.0±2.3, and 1.8±0.1 for the partial surface ICAt, partial surface ICAt*, and full surface ICAt* solutions, respectively.

The results of the perturbation trial are summarized in histogram format in Figure V.11 using the sub-surface error values calculated for each trial solution. As implied by the sub-surface target results and confirmed by manual observation of the ICAt and ICAt* solutions, the algorithm does not converge to a unique solution regardless of variations in initial pose. The results for the perturbation trials for the ICAt* algorithm using the full surface data indicate that when extensive surface information is available the algorithm becomes robust to variations in initial alignment with respect to the sub-surface target errors. When only partial surface data is used, the performance of the ICAt* algorithm seems to be more robust to variations in initial alignment than the initial ICAt formulation. The behavior illustrated by the results of the perturbation study indicate that the algorithm behaves in a similar fashion to ICP-based surface registration methods which are also sensitive to initial pose. This behavior seems to be due to the lack of known point correspondence within these applications and the reliance on the closest point operator or some similar variant to establish correspondence between the source and target data sets.

Discussion

The preliminary validation results from the simulation trials summarized in Table V.1 and Table V.2 indicate that the incorporation of point weighting into the previously proposed ICAt implementation (described in [39]) improves the robustness of the algorithm. In particular, for the trials in which the simulated LRS (i.e. partial surface) data was used within the generation of ICAt and ICAt* solutions the feature weighted implementation was able to converge to the true solutions for four of the five trials. This is a large improvement over the previous ICAt implementation which converged to the true solution for only a single one of the five trials. While the improved robustness of the algorithm via incorporation of feature weighting is exciting,

the reliance on full surface data for ensured convergence to an accurate solution suggest that further improvements in the robustness of the algorithm must be developed since an acquisition of the full liver surface intra-operatively is not feasible using the current IGLS system [27].

The results of the anthropomorphic liver phantom study provide some compelling preliminary results and also echoes the importance of surface coverage (i.e. the amount of data acquired intra-operatively when the liver is in a deformed state) on the ability of the proposed atlas-based deformation compensation technique to provide accurate results. In the case of the trials using partial surface (i.e. LRS) data, for both the qualitative surface distance and quantitative sub-surface target measurements the largest error values were found in the far field regions in relation to the location of the acquired LRS scans. While the results provided by the ICAt* method, which includes salient feature weighting and point correspondence biasing, are more robust and accurate, it is clear that further improvements must be made to ensure that robust and accurate solutions can be obtained in the situation where only minimal intra-operative surface data is acquired. Further, the error values shown for the ICAt and ICAt* solutions generated with the full surface data also indicate the importance of the creation of model solution atlases that fully encompass the true deformation imposed on the organ of interest. A potential, and very likely, source of error over all of the phantom results is the fact that the generated model solution atlas may not fully contain the imposed left and right lobe deformations.

While different phantoms were utilized in the two studies, the sub-surface target error data shown in Table V.3 and Table V.4 indicate that the proposed atlas-based approach provided comparable results to those achieved by the incremental FEM approach developed by Cash *et al* [28]. There are several key advantages of the proposed atlas-based technique over the incremental FEM method. First, the incremental FEM method uses the DIRR algorithm to initially orient the acquired surface data to the

pre-operative mesh. It is not clear that the DIRR will be robust when clinical data is utilized nor that the assumption that part of the acquired intra-operative data experiences no deformation. In contrast, the salient feature registration (developed in Chapter III) that is utilized within in the ICAt* implementation has been extensively utilized in registrations of clinical data. Futher, the proposed atlas-based method has the potential for faster intra-operative solution times and requires minimal user interaction in the surgical environment when compared with the traditional incremental FEM approach.

While the the presented method uses a very simple linear objective function without any constraining terms. Other work, such as that presented by Dumpuri *et al.* [53], have demonstrated the effectiveness of incorporating shape constraints within the linear model to improve accuracy. When making the transition from phantom and simulation to clinical data, it will likely be necessary to incorporate such constraints into the algorithm. Ultimately, the viability of utilizing an atlas-based approach to model updating is reliant on the ability to pre-operatively compute complete atlases that contain the full array of the deformations imposed by the various surgical loads. Incomplete atlases will limit the utility of the proposed ICAt algorithm in terms of yielding pertinent information to guide surgical procedures. Based on the analysis performed in Chapter IV, there are notable similarities in the imposed deformation across similar surgical procedures. However, it is unclear whether these similarities hold true across different surgeons due to the subtle differences in employing various surgical techniques. It may be needed to be both procedural and surgeon specific model solution atlases to achieve the most robust and accurate results.

Conclusion

The preliminary data provided in validation of the proposed atlas-based approach to model updating in IGLS indicate that the method should provide a more realistic and viable method to compensate for soft tissue deformation during surgical procedures. The ability to use *a priori* information to pre-compute an alas of model solutions allows for faster solution times and circumvents the need to prescribe boundary conditions within the OR is very exciting. However, the the amount of surface coverage acquired when the liver is in the deformed state (i.e. intra-operative sparse data) plays a large role in the performance of the proposed atlas-based deformation compensation method and additional work will be needed to ensure robust and accurate solutions for clinical data sets. By increasing our knowledge of the soft tissue deformation imposed by the surgical procedure in open hepatic resections we hope to be able to create more complete deformation atlases and ultimately provide model-updated images for guiding these procedures. Future work will entail improving the linear LSQ objective function by incorporating shape constraints to further improve robustness and validation of the proposed method using clinical data sets.

Acknowledgements

This work was supported by the NIH R21 Grant No. EB 007694-01 from the National Institute of Biomedical Imaging and Bioengineering of the National Institutes of Health. The authors would like to thank Dr. Sean Glasgow, Mary Ann Laflin, and Krista Cstonos of Washing University School of Medicine in St. Louis, MO for their help in collecting the clinical range scan data used in this work. In addition, many of the algorithms and visualization tools used in this work were developed using the Visualization Toolkit (http://www.vtk.org). The FastRBF Toolkit (FarField Technology, Christchurch, NZ) was used to generate a number of the surfaces shown. The ANN Nearest Neighbor Search Library (http://www.cs.umd.edu/ mount/ANN/)

was used to speed up closest point searches. Some segmentations of clinical data were performed using the Analyze AVE Version 6.0, which was provided in collaboration with the Mayo Foundation, Rochester, Minnesota. For disclosure, Drs. Chapman, Dawant, Galloway and Miga are founders and hold equity in Pathfinder Therapeutics, Inc., Nashville, TN.

CHAPTER VI

SUMMARY

The research described within the previous chapters presents a significant advancement to the field of image-guided liver surgery (IGLS) via the incorporation of anatomical features that can be reliably identified both in the pre-operative and intra-operative image data. In Chapter III, the utilization of these features has been shown to vastly improve the robustness of the rigid surface based registrations used to compute the mathematical mapping between the pre-operative images and the intra-operative presentation of the patient anatomy. Improving the robustness of the image-to-physical space registration method has proven to be invaluable in the performance of IGLS over multiple clinical sites and has shown a significant improvement in qualitative accuracy of the guidance information provided by the current state of the art IGLS system (Pathfinder Therapeutics, Nashville, TN).

In Chapter IV, the surface registration method enhanced with salient feature information was used to facilitate the quantitative evaluation of surface shift and organ shape change imposed during open hepatic resection procedures. The impact of soft tissue deformation is known to compromise the guidance information provided IGLS systems and no formal study of this deformation has heretofore been completed. Further, the evaluation of the nature of measured tissue shift and shape change over a variety of surgical procedures yields valuable insight into new deformation compensation methods that could further improve intra-operative guidance information and, ultimately, patient outcomes.

Finally in Chapter V, based on the improved surface registration method and surface deformation analysis, a new model-updating paradigm has been developed and studied for its feasibility for use within the context of IGLS. While preliminary, the

simulation and phantom results show that an atlas-based method for model-updating in IGLS is feasible and provides similar results to those previously reported by Cash *et al.* [28] Similar to the robust surface registration method developed, the incorporation of salient anatomical features within the atlas-based deformation compensation provides a marked improvement in accuracy and robustness when compared with the initial formulation without the incorporation of feature information.

Future Work

While the algorithms and methods developed in this work have facilitated a substantial advancement in the state of the art IGLS technology, there are a vast array of improvements and further studies that must be performed to transform IGLS into a standard of patient care for open hepatic resections. While a large body of work has been performed in the development of algorithms to use for registration and model-updating in IGLS, there is a dearth of analogous studies focused on clinical validation of the developed algorithms. Additionally, the extension of the IGLS methods developed for open procedures into the realm of laparoscopic and minimally invasive procedures is one of the next major challenges.

Targeting Accuracy Assessment of Image-Guided Liver Surgery

While qualitatively accurate registrations have been acquired intra-operatively via the algorithm developed within this work, a formal determination of the targeting accuracy provided by current IGLS systems has not been performed. An ongoing clinical study being performed by Pathfinder Therapeutics in collaboration with researchers at Vanderbilt University and clinicians at Memorial Sloan Kettering Cancer Center (MSKCC), University of Pittsburgh Medical Center (UPMC) and Shands Hospital at the University of Florida is seeking to acquire a large data set for the quantification of IGLS accuracy as well as provide the ability to validate potential model-updating

techniques. In addition to the acquisition of intra-operative digitizations for validation experiments, post-operative CT images of the remnant liver are also acquired for use in validating and gaining insight into model-updating techniques (shown in Figure VI.2). Preliminary data acquired for two patients from two of the participating clinical trial sites are shown in Figure VI.1 and Figure VI.2.

In addition to intra-operative digitizations of the resection contours, post-operative CT scans are also acquired of the remnant liver for retrospective analysis of the resection and registration (shown in Figure VI.2). While a vast majority of the post-operative CT data has not yet been useful for validation due, presumably, to parenchymal hypertrophy, the data shown in Figure VI.2 indicate that the post-operative CT imaging may have utility in studying deformation and for retrospective validation of the registrations and deformation compensation techniques. Ultimately, intra-operative acquisition of sub-surface information via co-registered C-arm CT or intra-operative ultrasound (iUS) is required to validate the targeting accuracy provided by IGLS registrations.

Movement Towards Minimally Invasive Image-Guided Liver Surgery

The results of recent research suggests that blood loss and hospital lengths of stay can be decreased by the performance of laparoscopic liver resections [106]. However, the loss of tactile information and the proximity of lesions near vascular structures can be contraindications for the use of minimally invasive techniques. The development of the appropriate registration techniques to make the current IGLS systems amenable to laparoscopic procedures would facilitate a more widespread implementation of minimally invasive methods for liver resection and treatment. While a large body of work has been dedicated to the development of algorithms for use in minimally invasive IGLS [144, 9, 104], no current system seems to exist whereby these methods

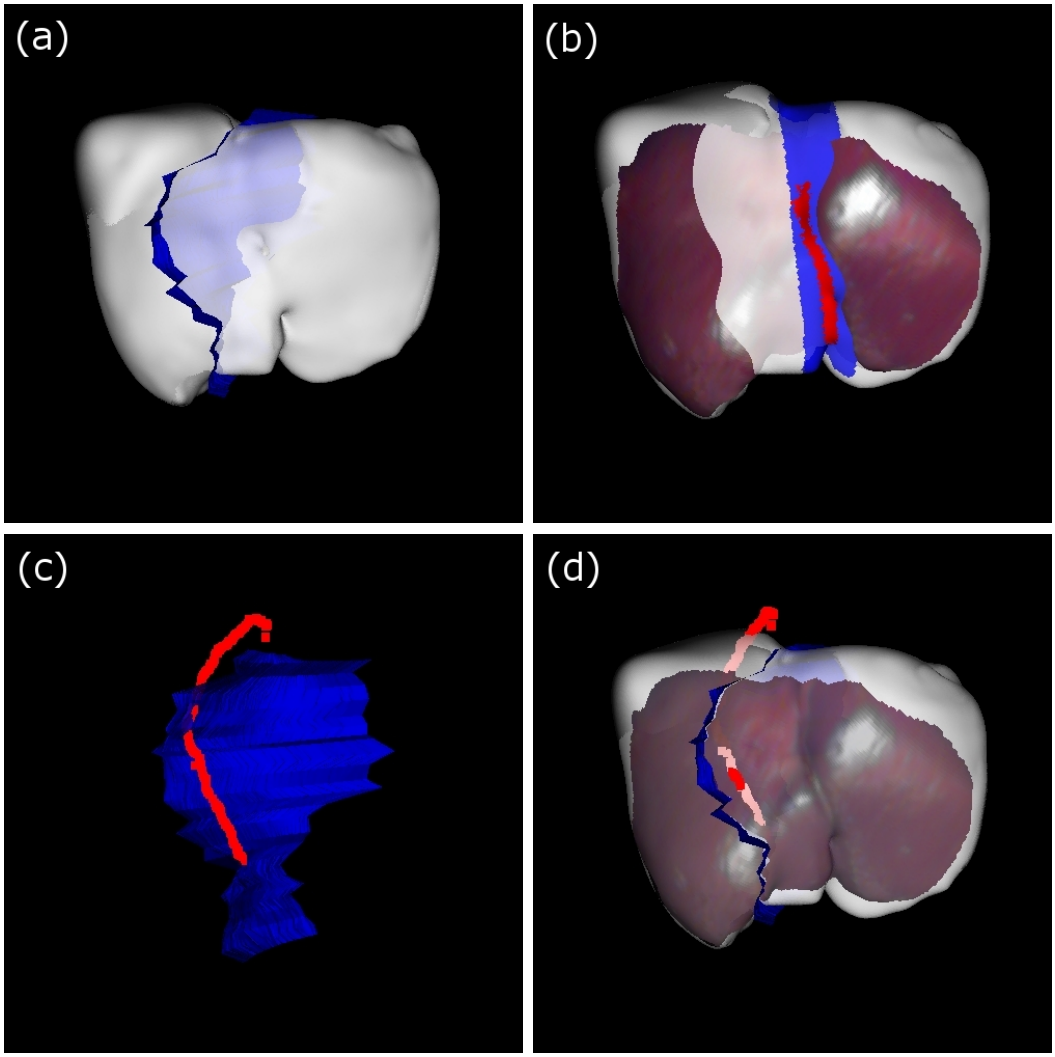

Figure VI.1: Preliminary validation results of IGLS via comparison of pre-operative resection plan with intra-operative digitization of resection contour acquired for a case performed at UPMC . The pre-operative CT surface showing the planned resection plane (a) is shown along with a depiction of the surface registration result provided by the weighted patch ICP algorithm developed in Chapter III (b). The falciform ligament feature used in the registration is visualized. The intra-operative digitization (red) is displayed on the pre-operative CT data using the transformation generated by the salient feature registration (c),(d).

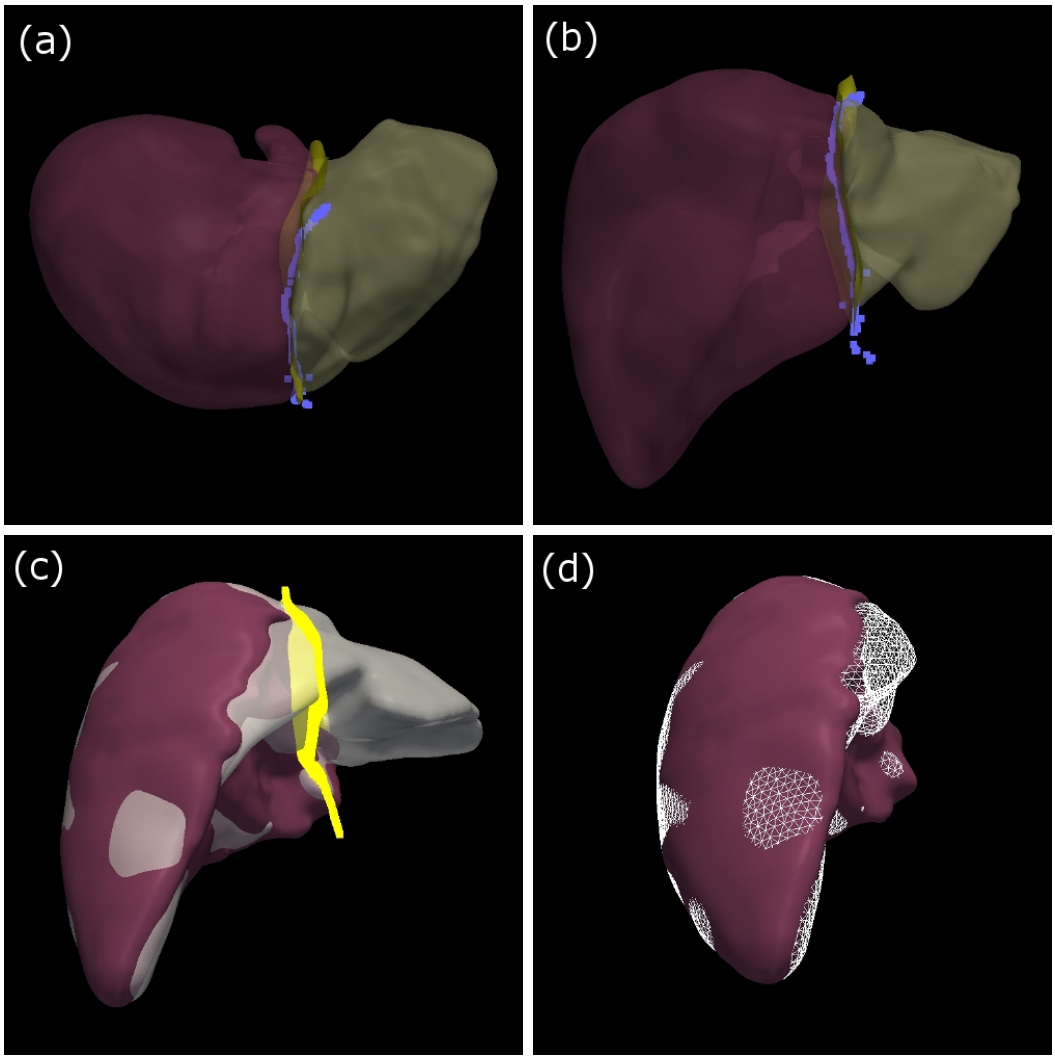

Figure VI.2: Comparison of the the pre-operative transection plane (yellow) with the intra-operative transection contour digitization (blue) for a case performed at MSKCC (a),(b). The intra-operative data is transformed via a registration computed by the salient feature surface registration developed in Chapter III. Comparison of post-operative CT liver surface with the pre-operative CT plan are also shown in (c). A direct comparison of the post-operative CT liver surface (purple) with the planned remnant liver (white) mesh is show in (d).

are implemented in a real-time fashion and results have only been shown for off-line and/or retrospective analysis.

The primary problem with the implementation of minimally invasive IGLS is the performance of image-to-physical registration. The surface registration methods utilized in open IGLS will likely not be useful or require significant modification due to the inability to acquire spatially accurate surface digitizations intra-operatively. Further, it is unclear whether the iUS registration methods proposed can be performed robustly and in a time frame that is reasonable for use in a surgical environment. Specifically, the ability to extract features and vasculature from liver iUS image data for use within image-registration techniques in an accurate, robust, and real-time manner has yet to be achieved. While the implementation of IGLS techniques in laparoscopic and hand-assisted laparoscopic procedures has not yet been realized, it is within the context of minimally invasive procedures that image-guidance will provide the greatest clinical utility.

Research Considerations

Before the beginning of this research on human subjects, there were two major considerations: the protection of the health and confidentiality of patients enrolled in this study and what contributions this research would have on society. The role of these factors is discussed below:

1. *Protection of Research Subjects:* Because human subjects were used in this research, all techniques were documented and approved by the Institutional Review Board (IRB) of Barnes-Jewish Hospital in St. Louis, MO. Informed consent was obtained from all patients before the procedure, and their confidentiality has been protected. Any information that could identify the patient

was removed from the medical imaging data and any photography acquired during surgery. Storage of all the patient documents and data pertaining to this research has been completed in accordance with IRB protocol.

2. *Societal implications:* By combining principles from the fields of computer vision, computer graphics, image processing, image registration, and finite element modeling, this work has made an effective contribution to the field of biomedical engineering and image-guided surgery. The ability to provide better therapeutic outcomes for patients in liver cancer will be a significant contribution to society. Liver metastases will continue to be a significant problem in the U.S. due to the tendency for other cancers to spread to the liver. In addition, primary tumors will be a growing concern, as the number of hepatitis C cases, one of the main risk factors for hepatocellular carcinoma, increases around the world. This work will not only be applicable to open abdominal resections and ablation procedures, but it will also aid in the targeting of minimally invasive procedures as well.

REFERENCES

[1] Ahn, S. J., Rauh, W., and Warnecke, H. J. Least-squares orthogonal distances fitting of circle, sphere, ellipse, hyperbola, and parabola. *Pattern Recogn. 34*, 12 (2001), 2283–2303.

[2] American Cancer Society. *Cancer Facts and Figures 2006*, 2006. http://www.cancer.org/downloads/STT/CAFF2006PWSecured.pdf.

[3] Arun, K. S., Huang, T. S., and Blostein, S. D. Least-squares fitting of 2 3-D point sets. *IEEE Trans. Pattern Anal. Mach. Intell. 9*, 5 (Sept. 1987), 699–700.

[4] Audette, M. A., Ferrie, F. P., and Peters, T. M. An algorithmic overview of surface registration techniques for medical imaging. *Medical Image Analysis 4*, 3 (2000), 201–217.

[5] Audette, M. A., Siddiqi, K., Ferrie, F. P., and Peters, T. M. An integrated range-sensing, segmentation and registration framework for the characterization of intra-surgical brain deformations in image-guided surgery. *Comput. Vis. Image Und. 89*, 2-3 (2003), 226–251.

[6] Audette, M. A., Siddiqi, K., and Peters, T. M. Level-set surface segmentation and fast cortical range image tracking for computing intrasurgical deformations. *Medical Image Computing and Computer-Assisted Intervention, Miccai'99, Proceedings 1679* (1999), 788–797.

[7] Aylward, S., Jomier, J., Guyon, J.-P., and Weeks, S. Intra-operative 3D ultrasound augmentation. In *Proceedings. 2002 IEEE International Symposium on Biomedical Imaging* (2002), pp. 421– 424.

[8] Banovac, F., Glossop, N., Lindisch, D., Tanaka, D., Levy, E., and Cleary, K. Liver tumor biopsy in a respiring phantom with the assistance of a novel electromagnetic navigation device. In *Medical Image Computing and Computer-Assisted Intervention - Miccai 2002* (2002), vol. 2488 of *Lecture Notes in Computer Science*, pp. 200–207.

[9] Bao, P., Warmath, J., Galloway, R. L., and Herline, A. Ultrasound to CT registration for image-guided laparoscopic liver surgery. *Surgical Endoscopy* (2004). In Press.

[10] Bentley, J. L. Multidimensional Binary Search Trees Used for Associative Searching. *Communications of the ACM 18*, 9 (Sept. 1975), 509–517.

[11] Berne, R., and M.N., L. *Special Circulations*, vol. 4th. Mosby, St. Louis, 1998, pp. 478–501.

[12] Besl, P. J., and McKay, N. D. A method for registration of 3-D shapes. *IEEE Trans. Pattern Anal. Mach. Intell. 14*, 2 (1992), 239–256.

[13] Biot, M. General theory of three-dimensional consolidation. *J.Appl.Phys. 12* (Feb 1941), 155–164.

[14] Birkfellner, W., Watzinger, F., Wanschitz, F., Enislidis, G., Kollmann, C., Rafolt, D., Nowotny, R., Ewers, R., and Bergmann, H. Systematic distortions in magnetic position digitizers. *Med.Phys. 25*, 11 (Nov 1998), 2242–2248.

[15] Birkfellner, W., Watzinger, F., Wanschitz, F., Enislidis, G., Truppe, M., Ewers, R., and Bergmann, H. Concepts and results in the development of a hybrid tracking system for cas. *Medical Image Computing and Computer-Assisted Intervention - Miccai'98 1496* (1998), 343–351.

[16] Birkfellner, W., Watzinger, F., Wanschitz, F., Ewers, R., and Bergmann, H. Calibration of tracking systems in a surgical environment. *Ieee Transactions on Medical Imaging 17*, 5 (1998), 737–742.

[17] Bittar, R. G., Olivier, A., Sadikot, A. F., Andermann, F., Comeau, R. M., Cyr, M., Peters, T. M., and Reutens, D. C. Localization of somatosensory function by using positron emission tomography scanning: a comparison with intraoperative cortical stimulation. *Journal of Neurosurgery 90*, 3 (1999), 478–483.

[18] Blackall, J. M., Penney, G. P., King, A. P., Adam, A. N., and Hawkes, D. J. Tracking alignment of sparse ultrasound with preoperative images of the liver and an interventional plan using models of respiratory motion and deformation. In *SPIE Medical Imaging 2004: Visualization, Image-Guided Procedures, and Display* (2004), vol. 5367, pp. 218–227.

[19] Blackall, J. M., Penney, G. P., King, A. P., and Hawkes, D. J. Alignment of sparse freehand 3-d ultrasound with preoperative images of the liver using models of respiratory motion and deformation. *IEEE Trans. Med. Imaging 24*, 11 (Nov. 2005), 1405–1416.

[20] Bookstein, F. L. Principal warps - thin-plate splines and the decomposition of deformations. *IEEE Transactions on Pattern Analysis and Machine Intelligence 11*, 6 (1989), 567–585.

[21] Brock, K. M., Balter, J. M., Dawson, L. A., Kessler, M. L., and Meyer, C. R. Automated generation of a four-dimensional model of the liver using warping and mutual information. *Medical Physics 30*, 6 (Jun 2003), 1128–1133.

[22] Cao, Z. J., Pan, S. Y., Li, R., Balachandran, R., Fitzpatrick, J. M., Chapman, W. C., and Dawant, B. M. Registration of medical images using an interpolated closest point transform: method and validation. *Med. Image. Anal. 8*, 4 (Dec. 2004), 421–427.

[23] Carr, J., Beatson, R.K. adn McCallum, B., Fright, W., McLennan, T., and Mitchell, T. Smooth surface reconstruction from noisy range data. In *ACM GRAPHITE 2003* (Melbourne, Austraila, 2003), pp. 119–126.

[24] Carrillo, A., Duerk, J., Lewin, J., and Wilson, D. Semiautomatic 3-D image registration as applied to interventional mri liver cancer treatment. *IEEE Transactions on Medical Imaging 19*, 3 (2000), 175–185.

[25] Cash, D., Sinha, T., Galloway, R., Chapman, W., Terawaki, H., and Miga, M. Incorporation of a laser range scanner into an image-guided surgical system. In *Medical Imaging 2003: Visualization, Display, and Image-guided Procedures* (2003).

[26] Cash, D. M. *Surface Registration and Deformation Compensation in Image-Guided Liver Surger*. PhD thesis, Vanderbilt University, 2004.

[27] Cash, D. M., Glasgow, S. C., Clements, L. W., Miga, M. I., Dawant, B., Cao, Z., Galloway, R. L., and Chapman, W. C. Concepts and preliminary data towards the realization of an image-guided liver surgery system. *J Gastrointest Surg 11*, 7 (July 2007), 844–59.

[28] Cash, D. M., Miga, M. I., Sinha, T. K., Galloway, R. L., and Chapman, W. C. Compensating for intraoperative soft-tissue deformations using incomplete surface data and finite elements. *IEEE Trans. Med. Imaging 24*, 11 (Nov. 2005), 1479–1491.

[29] Cash, D. M., Sinha, T. K., Chapman, W. C., Galloway, R. L., and Miga, M. I. Fast, Accurate Surface Acquisition Using a Laser Range Scanner for Image-guided Liver Surgery. In *SPIE Medical Imaging 2002, San Diego* (2002), vol. 4681.

[30] Cash, D. M., Sinha, T. K., Chapman, W. C., Terawaki, H., Dawant, B. M., Galloway, R. L., and Miga, M. I. Incorporation of a laser range scanner into image-guided liver surgery: Surface acquisition, registration, and tracking. *Med. Phys. 30*, 7 (Jun 2003), 1671–1682.

[31] Cha, C., Lee, F., Rikkers, L., Niederbuber, J., Nguyen, B., and Mahvi, D. Rationale for the combination of cryoablation with surgical resection of hepatic tumors. *Journal of Gastrointestinal Surgery 5*, 2 (2001), 206–213.

[32] Chapman, W., Debelak, J., Blackwell, T., Gainer, K., Christman, J., Pinson, C., Brigham, K., and Parker, R. Hepatic cryoablation-induced acute lung injury - pulmonary hemodynamic and permeability effects in a sheep model. *Arch.Surg. 135*, 6 (2000), 667–672.

[33] Chapman, W., Debelak, J., Pinson, C., Washington, M., Atkinson, J., Venkatakrishnan, A., Blackwell, T., and Christman, J. Hepatic cryoablation, but not radiofrequency ablation, results in lung inflammation. *Annals of Surgery 231*, 5 (2000), 752–760.

[34] Chui, H., Rambo, J., Duncan, J., Schultz, R., and Rangarajan, A. Registration of cortical anatomical structures via robust 3D point matching. In *Information Processing in Medical Imaging (IPMI '99)* (1999), A. Kuba, M. Sámal, and A. Todd-Pokropek, Eds., vol. 1613 of *Lecture Notes in Computer Science*, pp. 168–181.

[35] Chui, H., and Rangarajan, A. A new point matching algorithm for non-rigid registration. *Computer Vision and Image Understanding 89* (2003), 114–141.

[36] Chui, H., Win, L., Schultz, R., Duncan, J. S., and Rangarajan, A. A unified non-rigid feature registration method for brain-mapping. *Medical Image Analysis 7* (2003), 113–130.

[37] Clements, L., Cash, D., Chapman, W., Galloway Jr., R., and Miga, M. Robust surface registration using salient anatomical features in image-guided liver surgery. In *SPIE 2006 Medical Imaging: Visualization, Image-Guided Procedures, and Display* (2006), vol. 6141, pp. 105–115.

[38] Clements, L. W., Chapman, W. C., Dawant, B. M., Galloway, R. L., and Miga, M. I. Robust surface registration using salient anatomical features for image-guided liver surgery: algorithm and validation. *Med Phys 35*, 6 (Jun 2008), 2528–2540.

[39] Clements, L. W., Dumpuri, P., Chapman, W. C., R. L. Galloway, J., and Miga, M. I. Atlas-based method for model updating in image-guided liver surgery. In *Medical Imaging 2007: Visualization and Image-Guided Procedures* (2007), vol. 6509.

[40] Collignon, A., Vandermeulen, D., Suetens, P., and Marchal, G. Registration of 3d multi-modality medical images using surface and point landmarks. *Pattern Recogn. Lett. 15*, 5 (May 1994), 461–467.

[41] Comeau, R., Sadikot, A., Fenster, A., and Peters, T. Intraoperative ultrasound for guidance and tissue shift correction in image-guided neurosurgery. *Med.Phys. 27*, 4 (Apr 2000), 787–800.

[42] Comeau, R. M., Fenster, A., and Peters, T. M. Intraoperative us in interactive image-guided neurosurgery. *Radiographics 18*, 4 (1998), 1019–1027.

[43] Cootes, T. F., and Taylor, C. J. Combining point distribution models with shape models based on finite-element analysis. *Image and Vision Computing 13*, 5 (June 1995), 403–409.

[44] Cootes, T. F., Taylor, C. J., Cooper, D. H., and Graham, J. Active shape models - their traning and application. *Computer Vision and Image Understanding 61*, 1 (Jan 1995), 38–59.

[45] Couinaud, C. *Le Foie: Etudes Anatomiques et Chirurgicales*. Masson, Paris, 1957. Original definition of Couinaud segments for liver.

[46] Davatzikos, C., Shen, D., Mohamed, A., and Kyriacou, S. A framework for predictive modeling of anatomical deformations. *IEEE Trans. Med. Imaging 20*, 8 (Aug. 2001), 836–843.

[47] Dawant, B., Pan, S., and Li, R. Robust segmentation of medical images using geometric deformable models and a dynamic speed function. *Medical Image Computing and Computer-Assisted Intervention - MICCAI 2001 2208* (2001), 1040–1047. Lecture Notes in Computer Science.

[48] de Jode, M., Lamb, G., Thomas, H., Taylor-Robinson, S., and Gedroyc, W. Mri guidance of infra-red laser liver tumour ablations, utilising an open mri configuration system: technique and early progress. *J.Hepatol. 31*, 2 (Aug 1999), 347–353.

[49] D'Haese, P.-F., Cetinkaya, E., Konrad, P. E., Kao, C., and Dawant, B. M. Computer-aided placement of deep brain stimulators: from planning to intraoperative guidance. *IEEE Trans Med Imaging 24*, 11 (Nov 2005), 1469–1478.

[50] D'Haese, P.-F., Pallavaram, S., Niermann, K., Spooner, J., Kao, C., Konrad, P. E., and Dawant, B. M. Automatic selection of dbs target points using multiple electrophysiological atlases. *Med Image Comput Comput Assist Interv Int Conf Med Image Comput Comput Assist Interv 8*, Pt 2 (2005), 427–434.

[51] Dick, E., Taylor-Robinson, S., Thomas, H., and Gedroyc, W. Ablative therapy for liver tumours. *Gut 50*, 5 (May 2002), 733–739.

[52] Dumpuri, P., and Miga, M. I. Model-updated image guidance: A statistical approach to gravity-induced brain shift. In *Lecture Notes in Computer Science* (2003), vol. 2878, Medical Image Computing and Computer-Assisted Intervention, Springer-Verlag, pp. 375–382.

[53] Dumpuri, P., Thompson, R. C., Dawant, B. M., Cao, A., and Miga, M. I. An atlas-based method to compensate for brain shift: Preliminary results. *Medical Image Analysis Accepted* (2006).

[54] Engelman, M. S., and Sani, R. The implementation of normal and/or tangential boundary conditions in finite element codes for incompressible fluid flow. *International Journal for Numerical Methods in Fluids 2* (1982), 225–238.

[55] Feldmar, J., and Ayache, N. Rigid, affine and locally affine registration of free-form surfaces. *Int. J. Comput. Vision 18*, 2 (1996), 99–119.

[56] Feldmar, J., Declerck, J., Malandain, G., and Ayache, N. Extension of the icp algorithm to nonrigid intensity-based registration of 3D volumes. *Computer Vision and Image Understanding 66*, 2 (1997), 193–206. JMAY.

[57] Ferrant, M., Nabavi, A., Macq, B., Jolesz, F., Kikinis, R., and Warfield, S. Registration of 3-D intraoperative mr images of the brain using a finite-element biomechanical model. *IEEE Transactions on Medical Imaging 20*, 12 (2001), 1384–1397.

[58] Ferrant, M., Warfield, S. K., Nabavi, A., Jolesz, F. A., and Kikinis, R. Registration of 3D intraoperative mr images of the brain using a finite element biomechanical model. In *LNCS: Medical image computing and computer-assisted intervention: MICCAI '00* (2000), vol. 1935, Springer Verlag, pp. 19–28.

[59] Fitzpatrick, J., West, J., and Maurer, C. Predicting error in rigid-body point-based registration. *IEEE Transactions on Medical Imaging 17*, 5 (1998), 694–702.

[60] Frezza, E. E. Therapeutic management algorithm in cirrhotic and noncirrhotic patients in primary or secondary liver masses. *Digestive Diseases and Sciences 49*, 5 (2004), 866–871.

[61] Friedman, J., J.L., B., and R.A., F. An algorithm for finding best matches in logarithmic expected time. *ACM Trans.Math Software 3* (1977), 209–226.

[62] Galloway, R. L. The process and development of image-guided procedures. *Annual Review of Biomedical Engineering 3* (2001), 83–108.

[63] Galloway, R. L., Maciunas, R. J., and Edwards, C. A. Interactive, image-guided neurosurgery. *IEEE Transactions on Biomedical Engineering 39*, 12 (Dec. 1992), 1226–1231.

[64] Galloway, R. L., Macuinas, R. J., Bass, W. A., and Carpini, W. Optical localization for interactive, Image-Guided Neurosurgery. *Medical Imaging 2164* (1994), 137–145.

[65] Galloway Jr., R. The process and development of image-guided procedures. *Annu.Rev.Biomed.Eng 3* (2001), 83–108. UI - 21569434LA - engPT - Journal ArticleDA - 20011119IS - 1523-9829SB - IMCY - United States.

[66] Gazelle, G., and Haaga, J. Hepatic neoplasms: surgically relevant segmental anatomy and imaging techniques. *AJR Am.J.Roentgenol. 158*, 5 (May 1992), 1015–1018.

[67] Gazelle, G., Lee, M., and Mueller, P. Cholangiographic segmental anatomy of the liver. *Radiographics 14*, 5 (Sep 1994), 1005–1013. UI - 95083884LA - engPT - Journal ArticleDA - 19950110IS - 0271-5333SB - IMCY - UNITED STATESJC - RDG.

[68] Ge, Y., Maurer, C., and Fitzpatrick, J. M. Surface based 3-D image registration using the iterative closest point algorithm with a closest point transform. In *Proceedings of SPIE: Medical Imaging 1996* (1996), vol. 2710, pp. 358–367.

[69] Gignoux, B., Ducerf, C., Mabrut, J., Rivoire, M., Rode, A., and Baulieux, J. Cryosurgery for primary and metastatic liver cancers. *Annales de Chirurgie 126*, 10 (2001), 950–959.

[70] Herline, A., Stefansic, J., Debelak, J., Galloway, R., and Chapman, W. Technical advances toward interactive image-guided laparoscopic surgery. *Surg.Endosc. 14*, 7 (Jul 2000), 675–679.

[71] Herline, A. J., Herring, J. L., Stefansic, J. D., Chapman, W. C., Galloway, R. L., and Dawant, B. M. Surface registration for use in interactive image-guided liver surgery. In *LNCS: Medical Imaging Computation and Computer-Assisted Intervention: MICCAI '99* (1999), vol. 1679, Springer-Verlag, pp. 892–899.

[72] Herline, A. J., Herring, J. L., Stefansic, J. D., Chapman, W. C., Galloway Jr., R. L., and Dawant, B. M. Surface registration for use in interactive, image-guided liver surgery. *Comput. Aided Surg. 5*, 1 (2000), 11–17.

[73] Herline, A. J., Stefansic, J. D., Debelak, J. P., Hartmann, S. L., Pinson, C. W., Galloway, R. L., and Chapman, W. C. Image-guided surgery: preliminary feasibility studies of frameless stereotactic liver surgery. *Arch. Surg. 134*, 6 (Jun 1999), 644–649.

[74] Hermoye, L., Laamari-Azjal, I., Cao, Z. J., Annet, L., Lerut, J., Dawant, B. M., and Van Beers, B. E. Liver segmentation in living liver transplant donors: Comparison of semiautomatic and manual methods. *RADIOLOGY 234*, 1 (Jan. 2005), 171–178.

[75] Hill, D., Maurer, C., Maciunas, R., Barwise, J., Fitzpatrick, J., and Wang, M. Measurement of intraoperative brain surface deformation under a craniotomy. *Neurosurgery 43*, 3 (1998), 514–526.

[76] Horn, B. Closed-form solution of absolute orientation using unit quaternions. *J.Opt.Soc.Amer. 4* (1987), 629–642.

[77] Iannitti, D., Dupuy, D., Mayo-Smith, W., and Murphy, B. Hepatic radiofrequency ablation. *Arch.Surg. 137*, 4 (Apr 2002), 422–426.

[78] Joachimowicz, N., Pichot, C., and Hugonin, J. Inverse scattering: an iterative numerical method for electromagnetic imaging. *IEEE Transactions on Antennas and Propagation 39*, 12 (Dec. 1991), 1742–1753.

[79] Johnson, A. E., and Kang, S. B. Registration and integration of textured 3D data. *Image Vision Comput. 17*, 2 (Feb. 1999), 135–147.

[80] Kapoutsis, C. A., Vavoulidis, C. P., and Pitas, I. Morphological iterative closest point algorithm. *IEEE Trans. Image. Process. 8*, 11 (Nov. 1999), 1644–1646.

[81] Kelly, P., Kall, B., Goerss, S., and Earnest, F. Computer-assisted stereotaxic laser resection of intra-axial brain neoplasms. *J. Neurosurg. 64*, 3 (Mar 1986), 427–439.

[82] Lange, T., Eulenstein, S., Hunerbein, M., Lamecker, H., and Schlag, P. M. Augmenting intraoperative 3d ultrasound with preoperative models for navigation in liver surgery. In *Lecture Notes in Computer Science* (2004), Springer-Verlag, Ed., vol. 3217, Medical Image Computing and Computer-Assisted Intervention, pp. 534–541.

[83] Li, X., Yankeelov, T. E., Peterson, T. E., Gore, J. C., and Dawant, B. M. Automatic nonrigid registration of whole body ct mice images. *Med Phys 35*, 4 (Apr 2008), 1507–1520.

[84] Lorensen, W., and Cline, H. Marching cubes: A high resolution 3D surface construction algorithm. *ACM Computer Graphics 21*, 4 (Jul 1987), 163–169.

[85] Lunn, K., Paulsen, K., Roberts, D., Kennedy, F., Hartov, A., and West, J. Displacement estimation with co-registered ultrasound for image guided neurosurgery: a quantitative in vivo porcine study. *Medical Imaging, IEEE Transactions on 22*, 11 (Nov. 2003), 1358–1368.

[86] Lunn, K. E., Paulsen, K. D., Lynch, D. R., Roberts, D. W., Kennedy, F. E., and Hartov, A. Assimilating intraoperative data with brain shift modeling using the adjoint equations. *MEDICAL IMAGE ANALYSIS 9*, 3 (June 2005), 281–293.

[87] Machi, J., Uchida, S., Sumida, K., Limm, W., Hundahl, S., Oishi, A., Furumoto, N., and Oishi, R. Ultrasound-guided radiofrequency thermal ablation of liver tumors: percutaneous, laparoscopic, and open surgical approaches. *J.Gastrointest.Surg. 5*, 5 (Sep 2001), 477–489.

[88] Maes, F., Collignon, A., Vandermeulen, D., Marchal, G., and Seutens, P. Multimodality image registration by maximization of mutual information. *IEEE Trans. Med. Imaging 16*, 2 (Apr. 1997), 187–198.

[89] Marescaux, J., Clement, J., Tassetti, V., Koehl, C., Cotin, S., Russier, Y., Mutter, D., Delingette, H., and Ayache, N. Virtual reality applied to hepatic surgery simulation: the next revolution. *Ann.Surg. 228*, 5 (Nov 1998), 627–634.

[90] Maurer, C. R., Aboutanos, G. B., Dawant, B. M., Maciunas, R. J., and Fitzpatrick, J. M. Registration of 3-D images using weighted geometrical features. *IEEE Trans. Med. Imaging 15*, 6 (1996), 836–849.

[91] Maurer, C. R., Fitzpatrick, J. M., Wang, M. Y., Galloway, R. L., Maciunas, R. J., and Allen, G. S. Registration of head volume images using implantable fiducial markers. *IEEE Transactions on Medical Imaging 16*, 4 (1997), 447–462.

[92] Maurer, C. R., Hill, D. L. G., Maciunas, R. J., Barwise, J. A., Fitzpatrick, J. M., and Wang, M. Y. Measurement of intraoperative brain surface deformation under a craniotomy. In *Medical Image Computing and Computer-Assisted Intervention - Miccai'98*, vol. 1496 of *LECTURE NOTES IN COMPUTER SCIENCE*. 1998, pp. 51–62.

[93] Maurer, C. R., Hill, D. L. G., Martin, A. J., Liu, H. Y., McCue, M., Rueckert, D., Lloret, D., Hall, W. A., Maxwell, R. E., Hawkes, D. J., and Truwit, C. L. Investigation of intraoperative brain deformation using a 1.5-T interventional mr system: Preliminary results. *IEEE Trans. Med. Imaging 17*, 5 (1998), 817–825.

[94] Miga, M., Cash, D., Cao, Z., R.L., G., Dawant, B., and Chapman, W. Intraoperative registration of the liver for image-guided surgery using laser range scanning and deformable models. *SPIE Medical Imaging 2003 5029* (2003).

[95] Miga, M., Paulsen, K., Hoopes, P., Kennedy, F., Hartov, A., and Roberts, D. In vivo modeling of interstitial pressure in the brain under surgical load using finite elements. *J.Biomech.Eng 122*, 4 (Aug 2000), 354–363.

[96] Miga, M., Paulsen, K., Hoopes, P., Kennedy Jr., F., Hartov, A., and Roberts, D. In vivo quantification of a homogeneous brain deformation model for updating preoperative images during surgery. *IEEE Trans.Biomed.Eng 47*, 2 (Feb 2000), 266–273.

[97] Miga, M., Paulsen, K., Lemery, J., Eisner, S., Hartov, A., Kennedy, F., and Roberts, D. Model-updated image guidance: initial clinical experiences with gravity- induced brain deformation. *IEEE Trans. Med. Imaging 18*, 10 (Oct 1999), 866–874.

[98] Miga, M., Roberts, D., Kennedy, F., Platenik, L., Hartov, A., Lunn, K., and Paulsen, K. Modeling of retraction and resection for intraoperative updating of images. *Neurosurgery 49*, 1 (Jul 2001), 75–84.

[99] Miga, M. I., Sinha, T. K., Cash, D. M., Galloway, R. L., and Weil, R. J. Cortical surface registration for image-guided neurosurgery using laser range scanning. *IEEE Trans. Med. Imaging 22*, 8 (Aug 2003), 973–985.

[100] Mitros, F. A. *Tumors of Liver*. No. 11. Department of Pathology, The University of Iowa Hospitals and Clinics and The University of Iowa College of Medicine, 1996.

[101] Monga, O., and Benayoun, S. Using partial derivatives of 3D images to extract typical surface features. *Computer Vision and Image Understanding 61*, 2 (Mar 1995), 171–189.

[102] Murphy, M. A., O'Brien, T. J., Morris, K., and Cook, M. J. Multimodality image-guided surgery for the treatment of medically refractory epilepsy. *Journal of Neurosurgery 100*, 3 (2004), 452–462.

[103] Nabavi, A., Black, P., Gering, D., Westin, C., Mehta, V., Pergolizzi, R., Ferrant, M., Warfield, S., Hata, N., Schwartz, R., Wells, W., Kikinis, R., and Jolesz, F. Serial intraoperative magnetic resonance imaging of brain shift. *Neurosurgery 48*, 4 (2001), 787–797.

[104] Nakamoto, M., Hirayama, H., Sato, Y., Konishi, K., Kakeji, Y., Hashizume, M., and Tamura, S. Recovery of respiratory motion and deformation of the liver using laparoscopic freehand 3d ultrasound system. *Med Image Anal 11*, 5 (Oct 2007), 429–442.

[105] Nauta, H. Error assessment during 'image guided' and 'imaging interactive' stereotactic surgery. *Comput. Med. Imaging Graph. 18*, 4 (Jul 1994), 279–287.

[106] Nguyen, K. T., Gamblin, T. C., and Geller, D. A. Laparoscopic liver resection for cancer. *Future Oncol 4*, 5 (Oct 2008), 661–670.

[107] Nimsky, C., Ganslandt, O., Cerny, S., Hastreiter, P., Greiner, G., and Fahlbusch, R. Quantification of, visualization of, and compensation for brain shift using intraoperative magnetic resonance imaging. *Neurosurgery 47*, 5 (Nov 2000), 1070–1079.

[108] Nimsky, C., Ganslandt, O., Hastreiter, P., and Fahlbusch, R. Intraoperative compensation for brain shift. *Surg.Neurol. 56*, 6 (Dec 2001), 357–364.

[109] Nimsky, C., Ganslandt, O., Kober, H., Buchfelder, M., and Fahlbusch, R. Intraoperative magnetic resonance imaging combined with neuronavigation: a new concept. *Neurosurgery 48*, 5 (May 2001), 1082–1089.

[110] Northern Digital, Inc. *Polaris - Technical Specifications*. Waterloo, Ontario. http://www.ndigital.com/polaris-techspecs.php.

[111] Northern Digital, Inc. *Aurora - Technical Specifications*. Waterloo, Ontario, 2006. http://www.ndigital.com/aurora-techspecs.php.

[112] Northern Digital Inc. *Optotrak Certus - Technical Specifications*. Waterloo, Ontario, 2006. http://www.ndigital.com/certus-techspecs.php.

[113] O'Suilleabhain, P., and Dewey, R. Validation for tremor quantification of an electromagnetic tracking device. *Movement Disorders 16*, 2 (2001), 265–271.

[114] Ozsunar, Y., Skjoldbye, B., Court-Payen, M., Karstrup, S., and Burcharth, F. Impact of intraoperative ultrasonography on surgical treatment of liver tumours. *Acta Radiol 41*, 1 (Jan 2000), 97–101.

[115] Pan, S., and Dawant, B. M. Automatic 3D segmentation of the liver from abdominal CT images: a level-set approach. In *Medical Imaging 2001: Image Processing* (2001), M. Sonka and K. Hanson, Eds., vol. 4322, Proceedings of SPIE, pp. 128–138.

[116] Parker, G. A., Lawrence, W., Horsley, J. S., Neifeld, J. P., Cook, D., Walsh, J., Brewer, W., and Koretz, M. J. Intraoperative ultrasound of the liver affects operative decision making. *Ann Surg 209*, 5 (May 1989), 569–76; discussion 576–7.

[117] Paulsen, K., Miga, M., Kennedy, F., Hoopes, P., Hartov, A., and Roberts, D. A computational model for tracking subsurface tissue deformation during stereotactic neurosurgery. *IEEE Trans. Biomed. Eng 46*, 2 (Feb 1999), 213–225.

[118] Penney, G. P., Blackall, J. M., Hamady, M. S., Sabharwal, T., Adam, A., and Hawkes, D. Registration of freehand 3D ultrasound and magnetic resonance liver images. *Medical Image Analysis 8* (2004), 81–91.

[119] Peters, T. M. Image-guided surgery: from x-rays to virtual reality. *Comput Methods Biomech Biomed Engin 4*, 1 (2000), 27–57.

[120] Peters, T. M. Image-guidance for surgical procedures. *Phys Med Biol 51*, 14 (Jul 2006), R505–R540.

[121] Reittner, P., Tillich, M., Luxenberger, W., Weinke, R., Preidler, K., Kole, W., Stammberger, H., and Szolar, D. Multislice ct-image-guided endoscopic sinus surgery using an electromagnetic tracking system. *European Radiology 12*, 3 (2002), 592–596.

[122] Rifkin, M. D., Rosato, F. E., Branch, H. M., Foster, J., Yang, S. L., Barbot, D. J., and Marks, G. J. Intraoperative ultrasound of the liver. an important adjunctive tool for decision making in the operating room. *Ann Surg 205*, 5 (May 1987), 466–472.

[123] Ringe, B. Transplantation for liver tumors: current status. *Liver 22*, 1 (Feb 2002), 1–7.

[124] Roberts, D., Hartov, A., Kennedy, F., Miga, M., and Paulsen, K. Intraoperative brain shift and deformation: a quantitative analysis of cortical displacement in 28 cases. *Neurosurgery 43*, 4 (Oct 1998), 749–758.

[125] Rodhe, G., Aldroubi, A., and Dawant, B. The Adaptive Bases Algorithm for Intensity Based Non Rigid Image Registration. *IEEE Transactions on Medical Imaging 22*, 11 (Nov. 2003), 1470–1479.

[126] Rohlfing, T., Maurer, C. R., O'Dell, W. G., and Zhong, J. H. Modeling liver motion and deformation during the respiratory cycle using intensity-based nonrigid registration of gated MR images. *Medical Physics 31*, 3 (March 2004), 427–432.

[127] Rueckert, D., Sonoda, L. I., Hayes, C., Hill, D. L. G., Leach, M. O., and Hawkes, D. J. Nonrigid registration using free-form deformations: Application to breast mr images. *IEEE Transactions on Medical Imaging 18*, 8 (1999), 712–721.

[128] Sardi, A., Akbarov, A., and Conaway, G. Management of primary and metastatic tumors to the liver. *Oncology (Huntingt) 10*, 6 (Jun 1996), 911–925.

[129] Sasson, A., and Sigurdson, E. Surgical treatment of liver metastases. *Semin.Oncol. 29*, 2 (Apr 2002), 107–118.

[130] Schroeder, W., Zarge, J., and Lorensen, W. Decimation of triangle meshes. *ACM SIGGRAPH Computer Graphics 26*, 2 (1992), 65–70.

[131] Schwartz, S. I. Hepatic resection. *Ann Surg 211*, 1 (Jan 1990), 1–8.

[132] Selle, D., Preim, B., Schenk, A., and Peitgen, H.-O. Analysis of vasculature for liver surgical planning. *IEEE Trans. Med. Imaging 21*, 11 (Nov 2002), 1344–1357.

[133] SETHIAN, J. A. Numerical algorithms for propagating interfaceshamilton-jacobi equations and conservation-laws. *JOURNAL OF DIFFERENTIAL GEOMETRY 31*, 1 (Jan. 1990), 131–161.

[134] Sethian, J. A. *Level Set Methods and Fast Marching Methods: Evolving Interfaces in Computational Geometry, Fluid Mechanics, Computer Vision, and Materials Science*. Cambridge University Press, 1999.

[135] Sharp, G. C., Lee, S. W., and Wehe, D. K. ICP registration using invariant features. *IEEE Trans. Pattern Anal. Mach. Intell. 24*, 1 (2002), 90–102.

[136] Sherwood, L. *Human Physiology: From Cells to Systems*. Wadsworth Publishing Company, 1997.

[137] Shimizu, S., Shirato, H., Xo, B., Kagei, K., Nishioka, T., Hashimoto, S., Tsuchiya, K., Aoyama, H., and Miyasaka, K. Three-dimensional movement of a liver tumor detected by high-speed magnetic resonance imaging. *Radiother Oncol 50*, 3 (Mar 1999), 367–370.

[138] Sinha, T., Cash, D., Weil, R., Galloway, R., and Miga, M. Cortical surface registration using texture mapped point clouds and mutual information. *Medical Image Computing and Computer-Assisted Intervention - Miccai'02 2489* (2002), 533–540.

[139] Sinha, T. K., Dawant, B. M., Duay, V., Cash, D. M., Weil, R. J., Thompson, R. C., Weaver, K. D., and Miga, M. I. A method to track cortical surface deformations using a laser range scanner. *IEEE Trans. Med. Imaging 24*, 6 (June 2005), 767–781.

[140] Skrinjar, O., Nabavi, A., and Duncan, J. A Stereo-Guided Biomechanical Model for Volumetric Deformation Analysis. IEEE Workshop on Mathematical Methods in Biomedical Image Analysis (MMBIA 2001), Kauai, Hawaii.

[141] Skrinjar, O., Studholme, C., Nabavi, A., and Duncan, J. Steps Toward a Stereo-Camera-Guided Biomechanical Model for Brain Shift Compensation. Information Processing in Medical Imaging (IPMI 2001), Davis, CA, USA, pp. 183–189.

[142] Sohn, R. L., Carlin, A. M., Steffes, C., Tyburski, J. G., Wilson, R. F., Littrup, P. J., and Weaver, D. W. The extent of cryosurgery increases the complication rate after hepatic cryoablation. *American Surgeon 69*, 4 (Apr 2003), 317–322.

[143] Solbiati, L., Ierace, T., Goldberg, S. N., Sironi, S., Livraghi, T., Fiocca, R., Servadio, G., Rizzatto, G., Mueller, P. R., DelMaschio, A., and Gazelle, G. S. Percutaneous us-guided radio-frequency tissue ablation of liver metastases: Treatment and follow-up in 16 patients. *RADIOLOGY 202*, 1 (Jan. 1997), 195–203.

[144] Stefansic, J., Herline, A., Shyr, Y., Chapman, W., Fitzpatrick, J., Dawant, B., and Galloway Jr., R. Registration of physical space to laparoscopic image space for use in minimally invasive hepatic surgery. *IEEE Trans.Med.Imaging 19*, 10 (Oct 2000), 1012–1023.

[145] Stefansic, J. D., Bass, W. A., Hartmann, S. L., Beasley, R. A., Sinha, T. K., Cash, D. M., Herline, A. J., and Galloway, R. L. Design and implementation of a PC-based image-guided surgical system. *Computer Methods and Programs in Biomedicine 69* (2002), 211–224.

[146] Stokely, E., and Ww, S. Surface parameterization and curvature measurement of arbitrary 3-D objects - 5 practical methods. *IEEE Transactions on Pattern Analysis and Machine Intelligence 14*, 8 (1992), 833–840.

[147] Studholme, C., Hill, D. L. G., and Hawkes, D. J. An overlap invariant entropy measure of 3D medical image alignment. *Pattern Recogn. 32*, 1 (1999), 71–86.

[148] Sullivan, J., Charron, G., and Paulsen, K. A three-dimensional mesh generator for arbitrary multiple material domains. *Finite Elements in Analysis and Design 25*, 3-4 (1997), 219–241.

[149] Sun, H., Farid, H., and Paulsen, K. D. Cortical vessels for patient registration during image-guided neurosurgery, H. Sun, H. Farid, K. D. Paulsen. In *Proceedings of SPIE: Medical Imaging 2003* (Feb. 2003).

[150] Sun, H., Lunn, K., Farid, H., Wu, Z., Roberts, D., Hartov, A., and Paulsen, K. Stereopsis-guided brain shift compensation. *Medical Imaging, IEEE Transactions on 24*, 8 (Aug. 2005), 1039–1052.

[151] Talos, I. F., O'Donnell, L., Westin, C. F., Warfield, S. K., Wells, W., Yoo, S. S., Panych, L. P., Golby, A., Mamata, H., Maier, S. S., Ratiu, P., Guttmann, C., Black, P., Jolesz, F. A., and Kikinis, R. Diffusion tensor and functional mri fusion with anatomical mri for image-guided neurosurgery. In *Lecture Notes In Computer Science* (2003), vol. 2878 of *MICCAI 2003 - Medical Image Computing and Computer Assisted Intervention*, Springer-Verlag, pp. 407–415.

[152] Tikhonov, A. N., and Arsenin, V. Y. *Solutions of Ill-Posed Problems*. V.H. Winston & Sons, 1977.

[153] Trobaugh, J. W., Richard, W. D., Smith, K. R., and Bucholz, R. D. Frameless stereotaxic ultrasonography - method and applications. *Computerized Medical Imaging and Graphics 18*, 4 (1994), 235–246. JUL-AUG COMPUT MED IMAGING GRAPH.

[154] University of Iowa, Division of Physiologic Imaging, Department of Radiology. *Liver Anatomy Tutorial Overview*, 1999. http://everest.radiology.uiowa.edu/nlm/app/livertoc/liver/overview.html.

[155] Viola, P., and Wells, W. Alignment by maximization of mutual information. *Int. J. Comput. Vision 24*, 2 (1997), 137–154.

[156] Wang, M. Y., Maurer, C. R., Fitzpatrick, J. M., and Maciunas, R. J. An automatic technique for finding and localizing externally attached markers in ct and mr volume images of the head. *IEEE Transactions on Biomedical Engineering 43*, 6 (1996), 627–637.

[157] Wilkinson, I. D., Romanowski, C. A., Jellinek, D. A., Morris, J., and Griffiths, P. D. Motor functional mri for pre-operative and intraoperative neurosurgical guidance. *British Journal of Radiology 76* (2003), 98–103.

[158] Wilson, D., Carrillo, A., Zheng, L., Genc, A., Duerk, J., and Lewin, J. Evaluation of 3D image registration as applied to mr-guided thermal treatment of liver cancer. *Jmri-Journal of Magnetic Resonance Imaging 8*, 1 (1998), 77–84.

[159] Wong, L. Current status of liver transplantation for hepatocellular cancer. *Am.J.Surg. 183*, 3 (Mar 2002), 309–316.

[160] Wong, S., Edwards, M., Chao, C., Simpson, D., and McMasters, K. Radiofrequency ablation for unresectable hepatic tumors. *Am.J.Surg. 182*, 6 (Dec 2001), 552–557.

[161] Wu, Z. M. Multivariate compactly supported positive definite radial functions. *Adv. Comput. Math*, 4 (1995).

[162] Zhang, Z. Y. Iterative point matching for registration of free-form curves and surfaces. *Int. J. Comput. Vision 13*, 2 (1994), 119–152.